Politecnico di Torino

PhD School in Physics

PhD Thesis

Synthesis and characterization of piezoelectric thin films as functional materials for sensing

Marco Laurenti

Academic Supervisor

Prof. Candido Fabrizio Pirri

Coordinator of the PhD program in Physics

Prof. Arianna Montorsi

Tutor
Dott. Alessandro Chiolerio

XXVII Cycle 2012-2014

Academic Year 2014-2015

Scientific Disciplinary Sector: FIS/03

Contents

Chapter 1

Introduction

The aim of this work is the synthesis and characterization of piezoelectric thin films as functional materials for sensing. The activities were developed at the Center for Space Human Robotics (CSHR), which is part of the Istituto Italiano di Tecnologia (IIT) foundation.

The mission of the center is to study, design and realize demonstrators for the future generation of materials, processes and components for space human robotics, where locomotion and manipulation, sensing and perception, intelligence and communication with humans are the basic requirements. The development of these basic functions needs technologies applied to structural and functional components combined to compact and flexible energy supply systems. These novel technologies can also be fruitfully used in terrestrial robotic systems and in several industrial applications.

One of the main activities pursued by CSHR is the development of smart materials and technologies for micro/nano-sensors and actuators, based on MEMS and NEMS technology. Different items are investigated, such as the development of lead free piezoelectric materials based on polymer-ceramic composites and thin films, piezoresistive materials, piezoelectric nanostructures, hybrid and nanocomposite materials, nanostructured multifunctional polymers (for sensing and energy applications, including mechanical harvesting), new nanostructured materials for energy applications (polymeric electrolytes and new materials for electrodes, with a particular focus on metal oxides and carbon based structures), and the implementation of innovative processing techniques for device fabrication. The investigated materials are obtained through several low cost techniques: thin film deposition (chemical vapor deposition and sputtering), ink-jet deposition, chemical synthesis (hydrothermal, microwave assisted and wet processes), electrochemical synthesis (anodic oxidation), and surface functionalization (with specific molecules, thus easily expanding the materials functions in sensing or energetic direction).

This PhD thesis work is part of the activities related to the study and development of lead-free piezoelectric materials in the form of thin films, being applicable to both MEMS and NEMS technology.

Recently great interest has been shown towards the synthesis and characterization of piezoelectric materials with the aim of fabricating sensors and actuators, capable of converting mechanical energy into electrical energy and viceversa. The fields requiring such technologies are numerous. Especially for applications related to humanoid robotics, the development of piezoelectric sensors is quite important, in order to help in all those actions related to the interaction of the robot with the real world, especially related to objects identification and manipulation [1]. In the last few years many works proposed the integration of piezoelectric thin films in different devices configurations such as surface acoustic wave devices [2, 3] and piezoelectric-oxide semiconductor field-effect transistors (POSFETs) [4]. Such sensors were integrated in the sensing skin of the i-cub experimental platform, entirely developed within IIT.

Among all the piezoelectric materials, lead zirconate titanate (PZT) is by far the most performing one, thanks to its high piezoelectric constant and large electromechanical coupling factor. Actuators and surface acoustic wave sensors based on PZT thin films, and working at frequencies as high as a few GHz, have already been reported [2, 5]. Despite its amazing properties, the presence of lead makes PZT a toxic material. Parliament and the European Council, on June 8^{th}, 2011, approved a document (directive 2011/65/EU, [6]) regarding

the restriction in using certain hazardous substances in electrical and electronic equipment. This has strongly motivated the world of the scientific research to consider and deeply study lead-free piezoelectric materials alternative to PZT. Among them, zinc oxide (ZnO) is one of the most investigated, because of its versatility, cost-effectiveness and easiness of fabrication. Piezoelectricity of ZnO has been widely exploited for the fabrication of surface acoustic wave devices [3], nanogenerators [7], and hybrid energy harvesting nanoarchitectures [8]. Moreover, the possibility of combining its semiconductive and piezoelectric unique properties in the same device has been recently demonstrated, and the new class of so-called piezotronic devices started to be investigated [9].

The present work focuses on the synthesis and characterization of functional materials in the form of thin films, suitable for the fabrication of piezoelectric sensors. Zinc oxide has been selected as the functional material to be studied. ZnO-based piezoceramic thin films were deposited by a physical vapor deposition method, using the radio-frequency magnetron sputtering technique. One of the main characteristics of ZnO is the possibility of being growth in a lot of nanostructures with different morphologies and shapes. This aspect was considered in this work, and the attention was focused on two different thin film morphologies: the first one consisted in a dense and compact structure, while the second one is characterized by the presence of a nanoporous network, giving to the ZnO film a sponge-like morphology. For each of the stated morphologies, the optimization of the sputter deposition process was carried out, with the final aim of improving and emphasizing their piezoelectric behaviour. The presence of a sponge-like morphology was further exploited for the synthesis of doped ZnO thin films by the impregnation of the porous network with two different liquid solutions, providing the desired doping elements, i.e., manganese (Mn) and antimony (Sb).

Both dense and sponge-like ZnO films were deposited on a large variety of substrates. Silicon wafers were considered during the initial step of optimization of the deposition conditions. Also silicon covered with metal layers were considered, in order to provide a conductive substrate necessary for the functional characterizations of both the electrical and piezoelectric ZnO properties. Also glass substrates covered with transparent conducting oxides were used, with the aim of using transparent conductive supports. In addition, flexible polymer substrates, such as polyimide, were taken into account, in order to exploit the functional properties of the as-grown ZnO thin films for the preparation of flexible piezoelectric devices.

The characteristics of both dense and sponge-like ZnO thin films were properly analyzed. In particular, the chemical composition, crystal structure, and morphology were investigated by means of X-Ray Photoelectron Spectroscopy and Energy Dispersive X-ray spectroscopy, X-Ray Diffraction and Field-Emission Scanning Electron Microscopy measurements, respectively. The piezoelectric properties of both dense and sponge-like ZnO thin films were also analyzed. Different characterization techniques were used to evaluate both direct and converse piezoelectric effect, measuring the electrical charge generated when an external mechanical force was applied on the material (direct piezoelectric effect) or applying a signal voltage and measuring the mechanical displacement of the piezoceramic layer (converse piezoelectric effect). A quantitative evaluation of the piezoelectric coefficient in dense ZnO thin films was also performed by means of Piezoresponse Force Microscopy. Current-Voltage and Polarization-Voltage measurements were also carried out, in order to evaluate the electrical properties and to investigate the presence of ferroelectric behaviors in the piezoelectric thin films.

The basic scheme of this PhD thesis can be summarized as follows. A brief introduction about piezoelectric thin films and the theoretical aspects of piezoelectricity are briefly discussed in Chapter 2. This is followed by Chapter 3, reporting an exhaustive description of the physical principles governing the mechanism of thin film growth and describing the class of physical vapor deposition methods, with a particular reference to the case of the sputtering technique.

A description of the sputtering systems used for the deposition of the materials analyzed in this work is also reported. Chapter 4 is focused on the description of the physical properties of ZnO and the related applications, considering both the undoped and doped case. Chapter 5 summarizes all the results obtained from the deposition and characterization of ZnO thin films with a dense and compact nanostructure. A further insight into the exploitation of dense ZnO thin films is given in Chapter 6, which shows how these can be successfully used as a supporting material for growing high-quality ZnO nanowires. Sponge-like ZnO thin films were also considered as potential candidates for the preparation of piezoelectric active layers. All the results concerning the analysis of such a particular ZnO nanostructure are reported in Chapter 7. Finally, Chapter 8 reports about the synthesis and characterization of Mn-doped and Sb-doped, sponge-like ZnO thin films.

Bibliography

[1] V. Maheshwari, and R. Saraf, *Angew. Chem. Int. Ed.* **47** (2008) 7808-7826.

[2] A. K. Sarin Kumar, P. Paruch, J.-M. Triscone, W. Daniau, S. Ballandras, L. Pellegrino, D. Marré, and T. Tybell, *Appl. Phys. Lett.* **85** (2004) 1757.

[3] Y. Q. Fua, J. K. Luo, X. Y. Du, A. J. Flewitt, Y. Li, G. H. Markx, A. J. Walton, W. I. Milne, *Sens. Actuat. B-Chem.* **143** (2010) 606-619.

[4] R. S. Dahiya, G. Metta, M. Valle, A. Adami, and L. Lorenzelli, *Appl. Phys. Lett.* **95** (2009) 034105.

[5] Ph. Luginbuhl, G. -A. Racine, Ph. Lerch, B. Romanowicz, K. G. Brooks, N. F. de Rooij, Ph. Renaud, and N. Setter, *Sens. Actuat. A-Phys.* **54** (1996) 530-535.

[6] *Official Journal of the European Community*, Directive 2011/65/EU.

[7] Z. L. Wang, and J. Song, *Science* **312** (2006) 242-246.

[8] D. Choi, K. Y. Lee, K. H. Lee, E. S. Kim, T. S. Kim, S. Y. Lee, S. -W. Kim, J. -Y. Choi, and J. M. Kim, *Nanotechnology* **21** (2010) 405503.

[9] X. Wen, W. Wu, Y. Ding, and Z. L. Wang, *Adv. Mater.* **25** (2013) 3371-3379.

Chapter 2

Piezoelectric thin films as functional materials for sensing

2.1. Overview

With the advent of the micro and nanotechnologies the development of MEMS based on piezoelectric materials has gained growing and growing importance in the world of scientific research and a lot of attention is currently devoted to the study of such materials. The possibility of combining piezoelectric sensors and actuators with silicon-based CMOS technology, and to integrate them into smart structures, allows the implementation of a new class of devices which integrate sensors and operate autonomously, converting mechanical energy into dielectric displacement [1, 2]. Piezoceramic layers also found applications in the fabrication of impact sensors [3] required for structural health monitoring and integrity, quality control, and failure analysis in multitude of areas such as aerospace, automotive, and process control industries. Especially for spatial applications, these sensors are quite important. As satellites and spacecrafts travels through upper atmosphere, the corrosive chemicals like atomic oxygen strikes them at a velocity of about 5 miles per seconds [3]. This impact force affects the commonly used spacecraft materials, and hence reduces their overall lifetime. The damages caused by impact forces on the composite structures, such as delaminations, are almost impossible to detect by visual assessment, and thus results in significant failure of structural integrity [3].

Among all the functional ceramics, lead zirconate titanate ($Pb(Zr_{1-x}Ti_x)O_3$, PZT) attracted considerable attention thanks to the presence of excellent ferroelectric and piezoelectric properties, becoming one of the most studied materials of the last decade. It consists of a solid solution of lead titanate and lead zirconate, which can be present in different relative quantities. Generally, sputtering and sol-gel are the most diffused techniques for the deposition of PZT thin films, and their applications in MEMS devices have been fully demonstrated [4, 5]. Ferroelectric PZT thin films are also widely used in the study and fabrication of nonvolatile ferroelectric random access memories (FeRAM) while the strong piezoelectric response of PZT, in accordance with the presence of high electromechanical coupling coefficients, is exploited in the realization of sensors and actuators, especially for acoustic applications, where large piezoelectric coefficients and electromechanical coupling factors are preferred. Especially in the field of ultrasonic imaging, where transducers operating at frequencies comprised between 20 and 50 MHz are required, PZT films have been recently used and transducers operating at 20 MHz have been demonstrated [6, 7]. Furthermore, good electrical properties, i.e., a high dielectric constant and a strong dependence of the dielectric constant on the DC bias field, in accordance with ferroelectricity, makes PZT a good candidate for the realization of microwave devices applications, like voltage-controlled oscillators, varactors, delay lines, phase shifters, and as electric clock for nanomagnet logic circuits [8, 9].

Even though PZT is the most performing piezoceramic, thanks to its high piezoelectric constant, recently lots of efforts have been devoted to the study and development of innovative, non toxic, lead-free piezoelectric materials. Among them aluminum nitride (AlN), barium titanate (BT), and zinc oxide (ZnO) are by far the most studied.

Aluminum nitride is a valid alternative, thanks to its high electrical resistance, high breakdown voltage and low dielectric loss [10, 11, 12]. Despite its

smaller piezoelectric constant [13], a lower dielectric permittivity respect to the one of PZT makes AlN competitive in the realization of MEMS devices.

Similar to PZT, barium titanate belongs to the class of perovskite-based materials. The presence of a non centro-symmetrical tetragonal crystal structure at room temperature allows it to feature piezoelectricity. BT is a high dielectric material with a piezoelectric coefficient higher than those of ZnO and AlN [14]. As in the previous cases, also BT can be synthesized in different ways, both from physical and chemical vapor deposition methods, as well as by hydrothermal synthesis. The main problem of BT is the low T_C, which is around 120°C but can be increased by doping the material. Despite this aspect, a flexible nanogenerator based on BT thin film was reported by Park et al. [15]. In this case, perovskite BT thin films were deposited by radio frequency magnetron sputtering and transferred to a flexible substrate after an annealing process at a high temperature (700°C). Since such high temperature processes have not permitted direct application to flexible and plastic substrates, the transfer process of thin films represents a crucial point of the fabrication process. On the other hand, low-temperature-treated thin film does not require the cumbersome transfer of a thin film from inorganic substrates such as silicon or sapphire wafers to plastics. Thus, there is a need for a low temperature process for thin film based nanogenerators.

Zinc oxide is a lead-free, pyroelectric, piezoelectric, wide band gap semiconductor (3.37 eV) with a large exciton binding energy (60 meV) at room temperature and a wurtzite hexagonal structure. It can be synthesized both in the form of sponge-like and dense thin films [16, 17], and different kinds of nanostructures (nanowires [18], nanobelts [19], nanorods [20], nanocombs [21]) by physical vapor deposition techniques like sputtering, pulsed laser deposition, atomic layer deposition, chemical vapor deposition, but also by hydrothermal growth and sol-gel techniques. The selection of ZnO thin film for experimental studies is generally due to its ease of deposition on a wide variety of substrates, and the simplicity of its chemical composition with respect to perovskite piezoelectric materials. It does not necessarily require high temperature processes and any electric-thermal poling, which are necessary for PZT and BT, moreover its stoichiometry, texture and other properties can be easily controlled. However, ZnO also shows some disadvantages, like a quite low electrical resistance, and suffers from high electrical losses. Some of these problems, together with its poor piezoelectric properties, can be solved by properly doping ZnO.

It has been demonstrated that ZnO can be successfully used for the realization of photodetectors [22], light-emitting diodes [23], and chemical [24] sensors while the presence of piezoelectricity [13] makes ZnO suitable for the realization of surface acoustic wave resonators [25], nanogenerators [26], touch-sensitive piezoelectric sensors [27] and impact sensors. Moreover, a ZnO film-based piezoelectric microcantilever was fabricated by micromachining techniques [28], and used in smart slider in hard disk drives to do nanoactuation for detecting the slider-disk contact and then adjusting the spacing, in order to decrease the damage to the head disk interface. The possibility of exploiting ZnO piezoelectricity for the fabrication of tactile sensors has also been reported [27, 29]. Forces applied normal to the surface of an oriented ZnO thin-film capacitor can alter the surface charge on the ZnO owing to the piezoelectric effect. The charge can be detected by an on-chip NMOS amplifier. The sensor array reported by Polla et al. [29] consists of 1.0 μm-thick sputtered ZnO piezoelectric capacitors in an 8 x 8 array with each sensing element measuring 70 x 70 μm^2. Also chemical-reaction sensors, based on the pyroelectric effect in ZnO thin films, have been demonstrated [30]. In the last few years, the study of energy has been gaining more and more attraction, and there are many researches focused on the implementation of small size, light weight, high density in power, economically efficient, and environmentally friendly energy harvesting systems. Possible sources of ambient energy include light energy, vibration, wind power, and thermal energy. Solar power is the most frequently used. However, the application of solar power is restricted by day-and-night limitation [31]. Therefore,

the development of green energy should be able to address the disadvantages of solar power. In many applications energy harvesting systems were applied on microactuators and microsensors in MEMS technology, which need an independent and embedded power source without connection to the outside. One of the possible solutions is to design the power supply at the same scale as actuators, sensors, and electronics [32]. The conventional solution of using batteries can be undesirable, mainly because of being quite bulky and with a limited time-life, containing a finite amount of energy and also chemicals that could cause a hazard [33]. Mechanical vibration is ubiquitous in real environments and its conversion to electrical energy is considered one of the likely methods of powering wireless sensor, without hazardous byproducts related to power generation. Moreover, the power source does not need to be replaced [34]. The piezoelectric materials have electrical-mechanical coupling effects, and are the leading candidates for converting mechanical energy into electricity [35]. White et al. [36] developed an inertial piezoelectric generator that used 7 μm thick film of lead zirconate titanate (PZT) with 100 μm thick steel substrate. The device produced an output of 2.1 W from vibrations in the environment. Roundy et al. [37] improved the geometry of the scavenger's piezoelectric bimorph. With the same volume of PZT and a trapezoidal geometry it can supply more than twice the energy than the rectangular geometry. Fang et al.[38] used a generator structure of nickel-metal composite cantilever. At the resonant frequency of about 608 Hz, 608 mV AC voltage value with 2.16 W power level was obtained. Minazara et al. [39] used a mechanically excited unimorph piezoelectric membrane transducer. A power of 0.65 mW was generated at the resonance frequency of 1.71 kHz. Despite all these promising results, the fabrication of PZT-based energy harvesting systems may cause serious environmental pollution. Lead-free, ZnO-based energy harvesters have been successfully demonstrated [40]. Gazia et al. [41] showed that sponge-like ZnO films can be successfully used as a promising smart material for sensing and energy harvesting applications. In that case, they provided a mechanical stimulus exerted by the impact of a water drop delivered on the ZnO surface, and observed the generation of intense piezoelectric output voltage peaks, thus proving material sensing capability. Moreover, a maximum average output power density of 2.4 nW cm^{-2} was calculated. Wang et al. also realized energy harvesting systems based on 1D ZnO nanostructures [42], reaching output voltage of up to 2.03 V, and a peak output power density of 11 mW cm^{-3}[43].

Despite all the recent developments in the synthesis of lead-free, non toxic functional materials, a lot of work has to be done in order to improve AlN, BT, and ZnO electromechanical properties to become comparable with the PZT ones.

2.2. Hints of piezoelectric theory

Piezoelectricity is represented by a linear interaction between mechanical and electrical systems. The direct piezoelectric effect may be defined as the change in the electrical polarization proportional to the strain. When the application of an external mechanical stress induces a dielectric displacement, the material is said to be piezoelectric. This displacement manifests itself as internal electric polarization. Closely related to the direct piezoelectric effect is the converse one, in which a piezoelectric crystal becomes strained if an external electric field is applied. It should be noted that the piezoelectric effects strongly depend on the symmetry of the crystal, being a typical effect shown from all that classes of materials not having a center of symmetry in the crystal structure [44]. Both the direct and converse effects are thus the manifestation of the same fundamental property of non-centro symmetrical crystals.

The phenomenological theory of piezoelectricity is based on the principles of thermodynamics formulated by Lord Kelvin. In 1890 Waldemar Voigt published the first complete and rigorous formulation of piezoelectricity [45]. The

formulation used in the physics of crystals today owes much to Voigt's monumental work "Lehrbuch der Kristallphysik" [46]. Voigt formulated the theory of thermodynamic potentials for piezoelectricity. One could argue that this phase of development in solid state physics was concluded by the publication of Voigt's famous textbook in 1910. For all technical applications, thermodynamics is of special importance. The foundations of the thermodynamic theory of elastic dielectrics and of piezoelectricity were further developed in the second half of the twentieth century. In the late forties V.L. Ginzburg and A.F. Devonshire produced a phenomenological description of piezoelectric and other properties of ferroelectrics.

Piezoelectric effect is of fundamental importance for the piezoelectric measurements technology, and can be properly described by a general thermodynamic theory. Taking constants the temperature and entropy, the piezoelectric effect can be described just with the relationship between mechanical quantities T_μ or S_μ (stress or strain) and electrical quantities E_k or D_k (electric field or electric displacement). In this simplified representation, the piezoelectric effect can be described by the following set of linear equations [47]:

$$D_i = \varepsilon_{ik} E_k + d_{i\mu} T_\mu \tag{2.1}$$

$$S_\lambda = d_{k\lambda} E_k + s_{\lambda\mu} T_\mu \tag{2.2}$$

$$E_k = \beta_{ik} D_i - g_{k\mu} T_\mu \tag{2.3}$$

$$S_\lambda = g_{i\lambda} D_i + s_{\lambda\mu} T_\mu \tag{2.4}$$

$$D_i = \varepsilon_{ik} E_k + e_{i\lambda} S_\lambda \tag{2.5}$$

$$T_\mu = -e_{k\mu} E_k + c_{\lambda\mu} S_\lambda \tag{2.6}$$

$$E_k = \beta_{ik} D_i - h_{k\lambda} S_\lambda \tag{2.7}$$

$$T_\mu = -h_{i\mu} D_i + c_{\lambda\mu} S_\lambda \tag{2.8}$$

Equations of state 2.1, 2.3, 2.5, and 2.7 belong to the description of direct piezoelectric effect while equations 2.2, 2.4, 2.6, and 2.8 describe the converse effect. The piezoelectric effect could thus be described by four different material coefficients, according to the choice of independent variables. This choice is submitted to the particular experimental conditions, e.g. by electrical variables E_k or D_k given by shortened or open circuit conditions. If T_μ and E_k are considered as the independent variables, they correspond to free mechanical and electrical conditions and the piezoelectric effect is characterized by the coefficient $d_{i\mu}$. Such situation is especially important for piezoelectric measurements technology. Generally it is more or less fulfilled or at least assumed as fulfilled. Direct piezoelectric effect is described in such particular case by equation 2.9 [48]:

$$D_i = d_{i\mu} T_\mu \tag{2.9}$$

under the assumption of constant electric field. Experimentally, the electrically free conditions (E_k = const.) could be realized by shorting the electrodes where the generated charges are collected. Under the assumption of constant stress (even if in complicated multiaxial stress system), the piezoelectric element could be treated as mechanically free with respect to the electromechanical energy conversion. Under these conditions, the piezoelectric coefficient could be measured by using the converse piezoelectric effect. In this case, the piezoelectric coefficient just represent a proportionality factor between S_μ and E_k.

Equations 2.3 and 2.4 describe the situation in which D_i and T_μ are considered as the independent variables [49]. Such situation is valid for mechanically free, but electrically clamped, piezoelectric specimens. The piezoelectric effect is thus described by the piezoelectric coefficient $g_{i\mu}$. The piezoelectric coefficient could be measured as a proportionality factor between the electric field E_k and the mechanical stress T_μ under the condition of constant electric displacement in the sample. Piezoelectrically generated charges contribute by the depoling electric field and the electric displacement D_k in piezoelectric element remains zero. The piezoelectric element under such conditions is called "open". Corresponding piezoelectric coefficient $g_{i\mu}$ could be measured using the converse piezoelectric effect from the dependence of the elastic strain S_μ on the electric displacement D_i, caused by the free charges on the electrodes.

On the contrary, equations 2.5 and 2.6 are valid for the description of mechanically clamped, but electrically free piezoelectric element [49]. The independent variables in this case are E_k and S_μ, and the corresponding piezoelectric coefficients are represented by the piezoelectric coefficient $e_{i\mu}$, which might be obtained by using the converse piezoelectric effect. The mechanical stress T_μ is measured as a function of the electric field E_k under a constant mechanical strain. In this case, there is also a second possibility for the measurement of the $e_{i\mu}$ moduli, by the direct piezoelectric effect. In such a situation, the electric displacement D_i is measured as a function of the mechanical strain under the electrically free condition (i.e. electrodes on the sample are shortened). The applied mechanical strain could be practically measured, e.g., by the time-of-flight technique for ultrasound wave propagated through the element. The proportionality coefficient between piezoelectric signal and mechanical strain can be directly related to the piezoelectric moduli $e_{i\mu}$, because of shortened electrodes (constant electric field) [50, 51].

Equations 2.7 and 2.8 (independent variables D_i and S_μ) correspond to the combination of mechanically as well as electrically clamped piezoelectric element [49]. In this case, the piezoelectric effect is represented by the piezoelectric coefficient $h_{i\mu}$.

Every piezoelectric coefficient $d_{i\mu}$ in Eq. 2.9 corresponds to specific relationships between a particular mechanical stress component T_μ and to the specific component of the electric displacement D_i. On the basis of the direction of the electric displacement and of the mechanical stress component, different cases of piezoelectric effect could be distinguished, which are summarized in Table 2.1, with the corresponding piezoelectric coefficients representative of each situation.

	T_1	T_2	T_3	T_4	T_5	T_6
D_1	d_{11}	d_{12}	d_{13}	d_{14}	d_{15}	d_{16}
	L	T	T	S_L	S_T	S_T
D_2	d_{21}	d_{22}	d_{23}	d_{24}	d_{25}	d_{26}
	T	L	T	S_T	S_L	S_T
D_3	d_{31}	d_{32}	d_{33}	d_{34}	d_{35}	d_{36}
	T	T	L	S_T	S_T	S_L

Table 2.1. Piezoelectric coefficients corresponding to all the different piezoelectric effects - longitudinal (L), transversal (T), longitudinal shear (S_L), and transversal shear (S_T) [52].

Since piezoelectricity is strongly related to the crystal structure and symmetry of the corresponding piezoelectric material, only a subset of the total piezoelectric effects previously described can be observed [53]. ZnO belongs to the hexagonal wurtzite (6mm) crystal class. The piezoelectric coefficients and the corresponding average values describing ZnO piezoelectricity are summarized in Table 2.2.

$$\begin{bmatrix} 0 & 0 & 0 & 0 & d_{15} & 0 \\ 0 & 0 & 0 & d_{15} & 0 & 0 \\ d_{31} & d_{31} & d_{33} & 0 & 0 & 0 \end{bmatrix}$$

$$\begin{bmatrix} 0 & 0 & 0 & 0 & -11.34 & 0 \\ 0 & 0 & 0 & -11.34 & 0 & 0 \\ -5.43 & -5.43 & 11.67 & 0 & 0 & 0 \end{bmatrix}$$

Table 2.2. ZnO piezoelectric strain coefficients (10^{-12} C N^{-1}) [54].

Since d_{33} is the highest value predicted for ZnO, generally ZnO nanomaterials are synthesized in order to enhance the d_{33} piezoelectric coefficient and the longitudinal piezoelectric effect should be exploited for technological applications.

Bibliography

[1] N. Chidambaram, A. Mazzalai, and P. Muralt, *IEEE Trans. Ultrason. Ferr.* **59** (2012) 1624-1631 .

[2] K. Ortner, D. Koeßler, T. Jung, H. Jacobsen, and H. Quenzer, *Plasma Process. Polym.* **4** (2004) S134-S138.

[3] S. Joshy, G. M. Hegde, M. M. Nayak, and K. Rajanna, *Sens. Actuat. A-Phys.* **199** (2013) 272-282.

[4] C. S. Park, J. W. Lee, G. T. Park, and H. E. Kim, *J. Mater. Res.* **22** (2007) 1367-1372.

[5] F. Xu, S. Trolier-McKinstry, W. Ren, B. Xu, Z. L. Xie, and K. Hemker, *J. Appl. Phys.* **89** (2001) 1336-1348.

[6] A. Abellard, D. Kuscer, J. Holc, F. Levassort, O. Noshchenko, M. Lethiecq, and M. Kosec, *Proceeding of the 47th International Conference on Microelectronics, Devices and Materials* (2011).

[7] H. S. Hsu, V. Benjauthrit, Q. Wei, Y. Huang, Q. Zhou, and K. Shung, *Appl. Phys. A* **111** (2013) 459-463.

[8] J. Wu, D. Xiao, Y. Wang, J. Zhu, J. Zhu, and R. Xie, *J. Am. Ceram. Soc.* **91** (2008) 3786-3788.

[9] M. Vacca, M. Graziano, A. Chiolerio, A. Lamberti, M. Laurenti, D. Balma, E. Enrico, F. Celegato, P. Tiberto, L. Boarino, and M. Zamboni, *Electric Clock for NanoMagnet Logic Circuits. In: Field-Coupled Nanocomputing. Paradigms, Progress, and Perspectives* / Neal G. Anderson, Sanjukta Bhanja. Springer Berlin Heidelberg (2014) pp. 73-110.

[10] A. Cleland, M. Pophristic, and I. Ferguson, *Appl. Phys. Lett.* **79** (2001) 2070-2072.

[11] M. Dubois, and P. Muralt, *Appl. Phys. Lett.* **74** (1999) 3032-3034.

[12] G. Piazza, P. Stephanou, and A. Pisano, *J. Microelectromech. Syst.* **15** (2001) 1406-1418.

[13] Y. Fu, J. Luo, X. Du, A. Flewitt, Y. Li, G. Markx, A. Walton, and W. Milne, *Sens. Actuat. B-Chem.* **143** (2010) 606-619.

[14] P. Panda, *J. Mater. Sci.* **44** (2009) 5049-5062.

[15] K. -I Park, S. Xu, Y. Liu, G. -T. Hwang, S. -J. L. Kang, Z. L. Wang, and K. J. Lee, *Nano Lett.* **10** (2010) 4939-4943.

[16] M. Laurenti, V. Cauda, R. Gazia, M. Fontana, V. F. Rivéra, S. Bianco, and G. Canavese, *Eur. J. Inorg. Chem.* **2013** (2013) 2520-2527.

[17] A. Lamberti, A. Sacco, M. Laurenti, M. Fontana, C. F. Pirri, and S. Bianco, *J. Alloys Compd.* **615** (2014) S487-S490.

[18] M. Laurenti, A. Verna, M. Fontana, M. Quaglio, and S. Porro, *Appl. Phys. A* **117** (2014) 901-907.

[19] X. Wang, J. Song, and Z. L. Wang, *J. Mater. Chem.* **17** (2007) 711-720.

[20] A. Manekkathodi, M. -Y. Lu, C. W. Wang, and L. -J. Chen, *Adv. Mater.* **22** (2010) 4059-4063.

[21] T. L. Phan, Y. Sun, and R. Vincent, *J. Korean Phys. Soc.* **59** (2011) 60-64.

[22] J. B. K. Law, and J. T. L. Thong, *Appl. Phys. Lett.* **88** (2006) 133114.

[23] M. Willander et al., *Nanotechnology* **20** (2009) 332001.

[24] P. Motto, V. Cauda, S. Stassi, G. Canavese, and D. Demarchi, *SENSORS IEEE* (2013) 1-4.

[25] X.Y. Du et al., *J. Phys.: Conf. Ser.* **76** (2007) 012035

[26] X. Wen, W. Wu, Y. Ding, and Z. L. Wang, *Adv. Mater.* **25** (2013) 3371-3379.

[27] D. Choi, K. Y. Lee, K. H. Lee, E. S. Kim, T. S. Kim, S. Y. Lee, S. -W. Kim, J. -Y. Choi, and J. M. Kim, *Nanotechnology* **21** (2010) 405503.

[28] P. Wang, H. Du, S. Shen, M. Zhang, and B. Liu, *Nanoscale Res. Lett.* **7** (2012) 176.

[29] D.L. Polla, W.T. Chang, R.S. Muller, R.M. White, *International Electron Devices Meeting* (1985), 133-136.

[30] Y. Yang, W. Guo, K. C. Pradel, G. Zhu, Y. Zhou, Y. Zhang, Y. Hu, L. Lin, and Z. L. Wang, *Nano Lett.* **12** (2012) 2833-2838.
[31] R.C. Lin, B.R. Wu, Y.C. Chen, C.C. Cheng, and K.S. Kao, *The 4th International Conference on Advances of Thin Films and Coatings (Thin Films 2008)*, Singapore, June, 2008.
[32] G.J. Wang, W.C. Yu, Y.H. Lin, and H. Yang, *J. Chin. Inst. Eng.* **29** (2006) 697-706.
[33] C.B. Williams, and R.B. Yates, *Sens. Actuat. A-Phys.* **50** (1996) 8-11.
[34] G.H. Feng, and J.C. Hung, *Microsyst. Technol.* **14** (2008) 419-425.
[35] S. Watanabe, and T. Fujiu, *Procedure of 10^{th} IEEE International Symposium on Applications of Ferroelectrics* **1**, 18-21 August (1996) 199–204.
[36] P.G. Jones, S.P. Beeby, and N.M. White, *IEEE Proceedings: Science, Measurement and Technology* **148** (2001) 69-72.
[37] S. Roundy, E.S. Leland, J. Baker, E. Carleton, E. Reilly, E. Lai, B. Otis, J.M. Rabaey, and P.K. Wright, *Energy Harvesting & Conservation* **4** (2005) 28-36.
[38] H.B. Fang, J.Q. Liu, Z.Y. Xu, L. Donga, L. Wang, D. Chen, B.C. Cai, and Y. Liu, *Microelectron. J.* **37** (2006) 1280-1284.
[39] E. Minazara, D. Vasic, F. Costa, G. Poulin, *Ultrasonics* **44** (2006) e699-e703.
[40] C.T. Pan, Z.H. Liu, Y.C. Chen, and C.F. Liu, *Sens. Actuat. A-Phys.* **159** (2010) 96-104.
[41] R. Gazia, P. Motto, S. Stassi, A. Sacco, A. Virga, A. Lamberti, and G. Canavese, *Nano Energy* **2** (2013) 1294-1302.
[42] Z. L. Wang, and J. Song, *Science* **312** (2006) 242-246.
[43] G. Zhu, R. Yang, S. Wang, and Z. L. Wang, *Nano Lett.* **10** (2010) 3151-3155.
[44] J. Tichý, J. Erhart, E. Kittinger, and J. Přivratská, *Fundamentals of Piezoelectric Sensorics: Mechanical, Dielectric, and Thermodynamical Properties of Piezoelectric Materials* Springer-Verlag Berlin Heidelberg (2010) 1.
[45] W. Voigt, *Abh. Gött.* **36** (1890) 1-99.
[46] W. Voigt, *Lehrbuch der Kristallphysik* (1910) Teubner, Leipzig, Berlin.
[47] J. Tichý, J. Erhart, E. Kittinger, and J. Přivratská, *Fundamentals of Piezoelectric Sensorics: Mechanical, Dielectric, and Thermodynamical Properties of Piezoelectric Materials* Springer-Verlag Berlin Heidelberg (2010) 69.
[48] J. Tichý, J. Erhart, E. Kittinger, and J. Přivratská, *Fundamentals of Piezoelectric Sensorics: Mechanical, Dielectric, and Thermodynamical Properties of Piezoelectric Materials* Springer-Verlag Berlin Heidelberg (2010) 69-70.
[49] J. Tichý, J. Erhart, E. Kittinger, and J. Přivratská, *Fundamentals of Piezoelectric Sensorics: Mechanical, Dielectric, and Thermodynamical Properties of Piezoelectric Materials* Springer-Verlag Berlin Heidelberg (2010) 71.
[50] R. A. Graham, *Phys. Rev. B* **6** (1972) 4779-4792.
[51] R. A. Graham, *J. Phys. Chem. Solids* **35** (1974) 355-372.
[52] J. Tichý, J. Erhart, E. Kittinger, and J. Přivratská, *Fundamentals of Piezoelectric Sensorics: Mechanical, Dielectric, and Thermodynamical Properties of Piezoelectric Materials* Springer-Verlag Berlin Heidelberg (2010) 72.
[53] Y. Lu, N. W. Emanetoglu, and Y. Chen, ZnO Bulk, Thin Films and Nanostructures: Processing, Properties and Applications, Elsevier Ltd. (2006) 444.
[54] Y. Lu, N. W. Emanetoglu, and Y. Chen, ZnO Bulk, Thin Films and Nanostructures: Processing, Properties and Applications, Elsevier Ltd. (2006) 445.

Chapter 3

Thin film growth by the sputtering technique

The aim of this chapter is to introduce and accurately describe the sputtering technique, which is the deposition method used for the synthesis of all the functional materials analyzed in this work. Sputtering belongs to the class of Physical Vapor Deposition (PVD) methods. In the first section, the basic principles governing PVD techniques and thin film deposition will be discussed. A detailed description of the sputtering technique will be then provided, focusing particular attention on the physical principle governing this technology. In conclusion the systems used for the deposition of all the materials presented in this work will be described.

3.1. Physical Vapor Deposition techniques and thin film growth

Thin film growth consists in the deposition of different amounts of material layers on a massive substrate, starting from single atoms and/or molecules but eventually also involving atom clusters. This aspect allows to obtain an accurate control over the chemical composition and stoichiometry of the as-deposited materials, whose average thickness ranges from few nanometers up to tens of microns [1]. Generally thin film deposition techniques belong to Physical Vapor Deposition (PVD) or Chemical Vapor Deposition (CVD) methods. In the following, the attention will be focused on the class of PVD techniques.

PVD techniques are based on the deposition of materials starting from single atoms and/or molecules which come from a solid source. Atoms and/or molecules can be extracted by two main physical processes. In the first case, atoms and/or molecules come from the bombardment of the solid source with massive high-energy particles. This is the case of the sputtering techniques. In the second case, thermal excitation of the material source provides the energy needed for the extraction of atoms and/or molecules. This is the physical principle at the basis of evaporation methods.

Despite the existence of a large variety of PVD techniques, these are all linked to the following characteristics:

— formation of the vapor phase, by the extraction of atoms and/or molecules from a source material;
— transport of vapors on the substrate surface;
— thin film formation through condensation, nucleation and coalescence processes.

Some examples of PVD techniques are thermal and electron-beam evaporation, direct current (DC) or radio-frequency (RF) sputtering, ion-beam sputtering (IBS), pulsed laser deposition (PLD), and molecular beam epitaxy (MBE).

The process which leads to the formation of thin films is schematically represented in Fig. 3.1(a), and can be divided into six main steps:

1. **Generation of the vapor phase [2]**. The deposition process starts with the vapor phase formation through physical or chemical mechanisms, as stated before. In the particular case of PVD techniques, during this step, atoms and/or molecules needed for growing thin films are provided by evaporating or sputtering a solid source.
2. **Transport and condensation of the vapors on the substrate [2]**. Once the vapors are formed, these are carried on the substrate surface and

condense on it. Transport of the vapor phase can be performed in vacuum or in an inert atmosphere, using a proper carrier gas like argon or nitrogen. Once a particle has condensed, re-evaporation or diffusion of the condensed particle on the substrate can take place. The diffusion process leads to adsorption of atoms at nucleation centers after a Brownian movement, and might be favoured, particularly when special sites like edges or other defects are present on the substrate surface. In both condensation and diffusion phenomena, different activation energy values are involved and have to be overcome. The desorption rate, for example, is proportional to $exp(E_{des}/K_BT)$, where E_{des} is the activation energy for desorption. The activation energy for adsorption or diffusion is dependent on the atomic details of the process. This quantity influences the mean residence time of adatoms τ_s, which is proportional to $exp\,(E_{ad}/K_BT)$, where E_{ad} is the adsorption energy of adatoms on the substrates. If E_{ad} is in the order of K_BT, the adatoms will re-evaporate from the substrates.

3. **Adsorption [3]**.Once condensation is started, adsorption of atoms and/or molecules on the surface takes place. Adsorbed atoms and/or molecules are called adatoms. This process can occur in two different ways:
   a) Physical adsorption, or physisorption;
   b) Chemical adsorption, or chemisorption.
   These two adsorption processes are clearly different and strongly influence the final characteristics of the thin film. Physisorption is a process in which electrostatic interactions, like van-der Waals bonding, hardly perturb the electronic structures of the adatoms and the surface substrate upon adsorption. The interaction between adatoms and the surface is represented by attractive forces due to correlated charge fluctuations between mutually induced dipole moments. In the case of physisorption, adatoms are characterized by a high degree of mobility on the surface. This aspect can be well understood if physisorption potential characteristics are taken into account. A low binding energy on the order of 10 to 100 meV, and a relatively large equilibrium separation of 3-10 Å, are the main reasons why physisorbed particles are located at relatively large distances from the surface and usually have high surface mobility [4, 5].
   This last aspect has an important consequence on the inverse process, which takes place during thin film deposition; desorption of adatoms. Thin films deposition consists in a continuous alternation of condensation and evaporation of adatoms. At thermodynamic equilibrium between vapor phase and solid, the number of adatoms condensing on the surface and evaporating is the same. Indeed, all processes proceed in two opposite directions at equal rates, as required by the principle of detailed balance [6]. Therefore, in equilibrium, there is no net growth of a film. In order to allow thin film formation, it is necessary to operate far from thermodynamic equilibrium conditions, so that adsorption (condensation) process is favoured against desorption (evaporation). Generally, each adatom is characterized by a mean residence time after which it leaves the surface. In the case of physisorption this time is quite short, because of the high surface mobility of the adatoms, and the probability of adatoms desorption increases. Physisorption can only be observed when stronger chemisorption interactions are not present.
   Chemisorption, on the other hand, is an adsorption process similar to the formation of ionic or covalent bonding, and the electronic structure of the adatoms and the surface are strongly perturbed. When chemisorption takes place, new hybrid orbitals are formed and there may be charge transfer from one partner to the other. Chemisorption potentials are characterized by a short separation distance of 1-3 Å and high values of the binding energy, generally on the order of a couple of eVs. Chemisorbed adatoms are then characterized by a low surface mobility (the binding energy is higher than for physisorbed species), while the mean residence time increases, decreasing the probability that a chemisorbed adatom will leave the surface.
   During thin films deposition, physisorption and chemisorption take place

simultaneously and are related to the distance of the adatom from the surface. As stated before, when the distance of the adatom from the surface is comprised between 1-3 Å, chemisorption is promoted, while physisorption takes place for distances comprised between 3 Å and 10 Å.

4. **Nucleation [7]**. During this phase, adatoms are free of diffusing on the surface of the substrate, and aggregate themselves, giving rise to the formation of so-called nuclei. Nucleation can be described as the formation of atomic clusters. Newly formed nuclei are thermodynamically unstable when formed, and become thermodynamically stable when a critic dimension is reached (nucleation threshold).
5. **Island formation [7]**. Once the nucleation threshold is reached, nuclei start to expand until the saturation density of nucleation is achieved. After that, nuclei can growth both parallel to the substrate, thanks to the surface mobility, or perpendicularly, because of the continuous supply of material coming on the surface. In this way, different nuclei can aggregate to each other and so-called islands are formed.
6. **Coalescence [7, 8]**. The characteristic of this step is represented by the combination of different islands to each other, with the aim of decreasing the surface free area and creating a film with a discontinuous structure. If the substrate temperature is increased, coalescence phase is promoted, because surface mobility of islands is enhanced. The film structure becomes complete and more continuous thanks to the adsorption of adatoms coming from the vapor phase. The coalescence phase is very critical because strongly influences the final thin film structure and morphology [8]. During this step, islands can aggregate to each other in three different ways (reported in Fig. 3.1(b)):

— Island growth, also called **Volmer-Weber growth** mode. This is the case where the interaction between neighbouring film atoms exceeds the overlayer substrate interaction.
— Layer by layer growth, also called **Frank-van der Merwe growth** mode. In this case, the stronger interaction is between substrate and layer atoms.
— Mixed growth, also called **Stranski-Krastanov growth** mode. In this case, both adatom/adatom and adatom/surface interactions are equally favoured. After forming of one, or sometimes several complete monolayers, island formation occurs, and 3D islands grow on top of the first full layer.

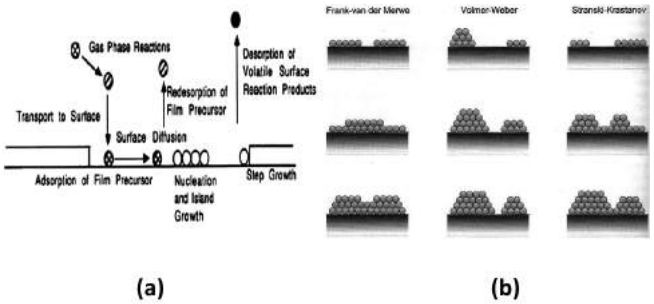

Figure 3.1. Schemes representative of (a) the different steps involved in the growth of thin films and (b) the Volmer-Weber, Frank-van der Merwe, and Stranski-Krastanov growth modes.

Two of the most important parameters in determining the particular growth mode of thin films are surface free energy γ and the degree of supersaturation. The growth mode of thin films is governed by γ_f, γ_s and γ_{fs}, which are respectively defined as the surface free energies of thin films, substrate and the interfacial energy [9, 10]. The island growth will be predominant at $(\gamma_S - \gamma_{FS}) <$

γ_F while the layer growth mode at $(\gamma_S - \gamma_{FS}) > \gamma_F$. The other parameter which influences the growth mode is called degree of supersaturation. This parameter allows to consider the equilibrium condition for the whole system including the gas phase above the deposited film. Supersaturation is related to the change in the free enthalpy of the system once a particle is transferred from the vapor phase to the solid. If this transfer occurs exactly at the equilibrium vapor pressure $p_0(T)$, then no energy is needed because of the equilibrium condition. If however the particle changes over from vapor to solid at a pressure p, a free enthalpy change is involved, proportional to $ln(p/p_0)$. This quantity is called degree of supersaturation and is one of the driving forces for the formation of a thin film deposited from an ambient vapor phase. The degree of supersaturation can influence the growth mode and, with increasing supersaturation, layer-by-layer growth is favoured [10, 11].

Also other parameters may influence the final characteristics of thin films, such as the energy of the impinging species on the substrate, the adsorption coefficient, the deposition rate, and the impurity level present during the deposition. A detailed analysis of these aspects will be provided in Section 3.2.2.

3.2. Sputtering

The aim of this section is the description of sputter deposition, which is the PVD technique used for the synthesis of all the materials described in this work. The attention will be focused on the physical principle governing sputter deposition and the influence of different sputtering parameters on the characteristics of the final material. This section will conclude with a description of the sputter systems used for the synthesis of the materials discussed in the following chapters.

3.2.1. Basic principles

Sputtering belongs to the class of plasma-assisted physical vapor deposition processes, in which a plasma is used as the source of energy for the formation of a vapor phase. Literally, sputtering process is the extraction of atoms from a solid source (target), and is based on the exchange of kinetic energy between ions and the atoms of the target material [12]. A noble gas (usually argon, Ar) is injected into the deposition chamber and ionized by the application of a proper potential between the cathode (where the target is placed), and the anode (where the substrate holder is placed). The impinging of the ions on the surface of the target allows the extraction of atoms. Once the vapor is formed, condensation on the surface of the substrate can take place and, by nucleation and coalescence, a continuous layer can be formed. The initiation of plasma discharge is linked to the presence of suitable vacuum conditions, which are provided by a proper high-vacuum system. High-vacuum conditions also allow the presence of a suitable atmosphere for thin film growth, free from any contaminants or pollutants. The mechanism of sputtering can locally create non-neutral electrical charge regions on the surface of the target, highly reducing the sputtering efficiency. For this reason, depending on the nature of the target material, both direct current (DC) or radio-frequency (RF) signal voltage are used. When electrically conductive materials such as metals are involved, both types of signal can be used. However, when non-conductive materials like oxides, nitrides or carbides have to be deposited, the use of a RF signal is required, in order to neutralize at each cycle the local charge created during the sputtering process, enhancing the sputtering efficiency. Depending on the nature of the target material and the material to be deposited, sputter deposition can be performed in an inert atmosphere or in a mixture of inert and reactive gases (oxygen). When a reactive gas is used, the process is referred to as the reactive sputtering technique. This particular configuration is interesting because of the possibility to strictly control and vary the stoichiometry of the

final material. Indeed, even if targets made of stoichiometric compounds are commercially available, sometimes it is necessary to adjust the stoichiometry of films in order to change and gradually tune the properties of the as-grown materials. Reactive sputtering is characterized by a higher deposition rate, and can be performed starting from both metallic and ceramic targets. So both DC and RF reactive sputtering are allowed. One of the major drawbacks encountered when performing reactive sputtering is the so-called target poisoning. It consists of the contamination of the target surface with compounds formed by the reaction between gas molecules and target atoms. When the target surface is completely covered by this compound, the target is poisoned and a strong decrease in the sputtering yield can be observed.

Sputtering process can be simply divided into five steps, described below:

1. Generation of energetic species (ions) used for the bombardment of the solid source, through the ionization of inert gas atoms by creating a plasma discharge. Ar but also Xe or Ne are commonly used for this purpose.
2. Sputtering process can occur only if ions have a proper energy value. The energy of the ions depends on the electric field applied between the anode and the cathode. For a proper polarization value, ions have a sufficient energy able to extract atoms from the target, when impinging on the surface of the solid source. The applied electric field is then used for the acceleration of the ions onto the target surface. Typical energy values of sputtered atoms range from 1 to 10 eV.
3. Atoms and/or molecules are extracted from the target.
4. Sputtered atoms and/or molecules move from the target towards the substrate surface, adsorbing on it.
5. Thin film formation can start, through condensation, nucleation and coalescence of the adsorbed atoms and/or molecules on the surface of the substrate.

The physical model which is generally used for the explanation of the sputtering process is the momentum transfer theory [13]. In this picture, sputtering is described as an energy transfer between ions and the atoms of the target, in which the only atoms involved in the process are those which energy momentum is completely transferred from the ions arriving on the surface of the target itself.

3.2.2. Sputtering parameters

The final quality of thin films is strictly related to different parameters. A close control of the physical and/or chemical properties of the resulting thin films is indeed necessary for both scientific research and applications.

The main characteristics which influence the final thin films quality are [14]:

1. Chemical composition
2. Crystal structure
3. Crystal phase
4. Surface flatness
5. Film stress

All these properties are in turn governed by the following parameters [14, 15]:

1. Chemical composition:
   - Flux composition of sputtering source
   - Flux composition of sputtered adatoms, impurity, and/or residual gas atoms
   - Sticking coefficient of adatoms
   - Surface reaction of the adatoms
   - Interdiffusion between the adatoms and the substrates
   - Mixing of adatoms in the growing films
2. Crystal properties:
   - Film composition, stoichiometry
   - Impurity and/or foreign atoms
   - Surface mobility of adatoms
   - Surface chemical properties of substrates
   - Interface properties between thin films and substrates

— Phase separation

Some examples of the relation between thin film properties and the sputtering parameters are reported in Table 3.1.

Thin film properties	Key sputtering parameter
Composition	Target composition
Crystal phases	Target crystallinity, target crystal orientation, substrate temperature
Film microstructures	Post-deposition annealing temperatures
Surface microstructures	Sputtering atmosphere, total pressure, partial pressure
Interface microstructures	Substrate materials/ Electrode materials
Defects	Substrate position/Bias
	Cooling rate, cooling atmosphere

Table 3.1. Thin film properties and key sputtering parameters [15].

Control of film structure [16]. The microstructure and morphology of thin films depend on the kinetics of growth and hence on the substrate temperature, source and energy of impinging species, the chemical nature, the topography of the substrate and gas ambience.

One of the most important factors affecting the final quality of thin films is the surface mobility of the adsorbed species, which is in turn determined by different aspects such as kinetic energy of the impinging species, deposition rate, supersaturation and the level of impurities.

The lateral grain size, for example, is expected to increase when surface mobility of adsorbed species and supersaturation increase. As a result, thin films with well-defined large grains are expected at high substrate temperatures, because it results in high surface mobility. The effect of substrate temperature on grain size is more prominent for relatively thicker films, and can be obtained also performing post deposition thermal annealing treatments, at temperatures higher than the deposition temperature; the higher the annealing temperature, the larger is the grain size obtained. The grain growth is more pronounced by depositing the film at annealing temperatures. Indeed, high-activation energy processes as thermal diffusion are present in this case, instead of lower activation energy values related to the condensation process of mobile species, when directly heating the substrates during the deposition. It is worth noting that the grain size cannot be increased indefinitely, because of the limitation on the surface mobility of the adsorbed species.

Epitaxial growth [17, 18]. Both substrate temperature and deposition rate strongly influence the crystal structure of the final thin films. Amorphous materials can be obtained at low deposition temperatures with high deposition rate values. The conversion of the amorphous phase towards a polycrystalline structure can be reached increasing the substrate temperature during deposition. Another important factor affecting the crystal quality is the substrate material. Epitaxial growth of single-crystal thin films is possible if crystallographic compatibility between substrate and the deposited material is present, together with high surface mobility, high substrate temperatures, low supersaturation, clean and smooth substrate surfaces. Regarding the substrate material, amorphous thin films are prepared on glass/ceramic substrates at temperatures lower than the crystallization temperature of the thin film. Polycrystalline films are prepared on a glass/ceramic substrate, above the crystallization temperature. Single-crystalline films can be prepared on a single-crystal substrate due to the epitaxial growth process and, in general, they are epitaxially grown on a single-crystal substrate at the substrate temperature above the epitaxial temperature. Polycrystalline films deposited on single crystalline substrates can be converted to single-crystalline films with a post-deposition annealing process.

Surface roughness [19]. Surface roughness characteristics are mainly related to nucleation barrier and supersaturation. When the former is low and the latter is large, the initial nucleation density is low and the size of the critical nucleus is small. This results in fine-grained smooth surfaces, which become continuous at small thicknesses. On the contrary, when the nucleation barrier is large and supersaturation is low, large but few nuclei are formed, which result in coarse-grained, rough films, and become continuous at relatively large thicknesses. Also the surface mobility affects the surface morphology, and smooth deposits can be obtained when the surface mobility is high. There is an exception to this situation, involving those materials which preferentially grow along specific crystallographic directions because of either anisotropy in the surface energy or the presence of faceted roughness on the substrate. Generally also the growth mode influences the surface roughness. Smooth surfaces are favoured in the case of Frank-van-der-Merwe growth mode while roughness is promoted for Volmer-Weber growth mode.

Adhesion [20, 21]. The adhesion of a deposit to the substrate is strongly related to the chemical nature, cleanliness and topography of the substrate surface. Generally, high values of kinetic energy of the incident species, adsorption energy of the deposit and initial nucleation density provide a better adhesion of the deposit. Higher or lower adsorption energy values can be provided by the presence of contaminants on the substrate surface, while a fine-grained substrate is characterized by a high nucleation density, which promotes the adhesion of the deposited material. On the other hand, loose and porous deposits are formed under conditions of high supersaturation and poor vacuum, and the resulting films are less adherent than compact ones.

All deposits store a certain amount of elastic energy, due to the presence of internal stresses included during film growth. These can be introduced by different thermal expansion coefficients between the deposit material and the substrate material and/or by lattice misfits in presence of crystalline substrates. If the stored elastic energy is greater than the adhesive energy, the deposited films will peel off. Peeling of the deposited material also happens when the critical value of film thickness is overcome.

3.2.3. Sputtering systems

In this section a brief overview of the most common sputtering techniques is presented.

DC diode sputtering [22, 23]. This is the simplest sputter configuration, where a constant DC electric field is applied between a pair of planar electrodes, the first working as anode, the second as cathode. Ion formation takes place when a proper electrical voltage (200 - 1000 V) is applied between the electrodes and a suitable gas pressure is present in the vacuum chamber. These conditions allow the triggering of a plasma discharge and the ionization of gas molecules. Substrates are placed on the anode while the target is mounted on the cathode. The electric field accelerates the ions from the anode to the cathode, where the target is placed. Collisions of the ions on the surface of the target allow the extraction of target atoms (sputtering process) and the deposition of sputtered atoms on the substrate surface, giving rise to thin film growth.

RF diode sputtering [24, 25]. When ceramic targets are used, static electric fields cannot be applied for starting the deposition, because of charge accumulation on the surface of the target and the consequent plasma shutdown, as discussed in Section 3.2.1. In order to overcome this limitation, a radio-frequency (RF) signal voltage must be used (typical working frequency 13.56 MHz). Depending on the nature of the target material, typical values for the RF signal range between 50 and 300 W.

Magnetron sputtering [26, 27]. In order to increase the sputtering yield, a fixed magnetic field can be applied on the target surface (balanced magnetron sputtering). In this case, the electrons present in the plasma can be confined

in the region next to the target surface and their orbits cover spirals close to the target. This increases a lot the ionization process yield and the sputter deposition rate. In other cases, the magnetic field can be unbalanced towards the anode, with the aim of achieving the ionic bombardment of substrates. In some cases this can be selfdefeating but in others is necessary to obtain films with better final characteristics. Indeed, substrate bombardment allows to remove those atoms which are not completely bonded. In this way the resulting films will be characterized by a higher hardness and an improved adhesion.

Ion-beam sputtering [28, 29]. In the previous techniques, plasma is used as the source of high-energy ions for performing the sputtering process. However this can also be obtained through an ion-beam sputter system. In this case, ions are generated by a ion beam. A proper control system allows to focus and accelerate the ions on the surface of the target. The main advantage of this system is the possibility of obtaining films with a higher purity degree, despite the lower growth rate.

3.3. System Set-Up

This section concerns the description of the two sputter systems which were employed for the deposition of the materials reported in this work. Two different systems were used: a RF magnetron sputtering monotarget and a confocal co-sputter system.

3.3.1. RF magnetron sputtering monotarget

One of the systems used for thin films deposition is shown in Fig. 3.2.

Figure 3.2. RF magnetron sputtering monotarget system.

The deposition process takes place in a cylindrical stainless steel chamber (400 mm diameter, 550 mm height), equipped with a single 4" circular cathode

on which the target is clamped, facing downwards. Substrates are placed in the lower part of the reactor, facing upwards toward the target, with an average target-to-substrate distance of 8 cm (see Fig. 3.3). These technical features guarantee the deposition of uniform and homogeneous coatings on a maximum area of about 80 cm^2.

Figure 3.3. RF magnetron sputtering monotarget system - View of the inner part of the deposition chamber.

A RF signal generator, operating at a working frequency of 13.56 MHz, and a matching network, needed to adjust the reflected power down to zero, are respectively used to supply and maximize the signal power provided to the cathode. Sputtering deposition of materials requires suitable vacuum conditions before starting the deposition, granting an environment clean from contaminations and from residues such as oxygen and moisture. These are obtained by a two-stage pumping system, made by a rotary and a turbomolecular pumps connected in series (nominal pumping speeds of 15 m^3/h and 350 l/s respectively), allowing to reach pressures as low as 10^{-7} Torr. The final characteristics of the thin films can be controlled by properly modifying the deposition parameters, i.e., gas flux, gas composition and partial pressures, the substrate temperature and the applied RF signal power. Gas flows are properly controlled by a set of mass flow controllers while the substrate temperature is monitored by a thermocouple.

3.3.2. Confocal co-sputtering system

The other sputtering system used for the deposition of thin films is shown in Fig. 3.4. Namely, it is a confocal co-sputter system (KS 300 CONFOCAL Dual, Kenosistec). This model is labeled as a "cluster" system, and is composed by two different deposition chambers (in the following named PM1 and PM2). PM1 and PM2 chambers are connected to each other, and consequential depositions of different kind of materials are allowed. Each deposition chamber is equipped with three cathodes which can work simultaneously. In this way, deposition of multilayer structures or co-deposition of different materials can be performed. Both the deposition chambers are connected through a central load-lock (LL) chamber, shown in Fig. 3.5. The presence of the LL chamber allows the automatic transfer of samples to both the deposition chambers PM1

and PM2, or from one to the other. The confocal co-sputter system is then composed of:

— Two deposition chambers (PM1 and PM2), each equipped with three water - cooled cathodes, designed for working with high power density values. The cathodes are mounted in a confocal geometry, as shown in Fig. 3.6.

— A rapid sample introduction chamber (LL chamber), which can be easily opened for loading the samples, and quickly pumped to pressure values up to 10^{-7} mbar. The presence of the LL chamber allows to improve substrate cleaning and the total time of the work cycle, without perturbing for a long time the vacuum conditions of the process chambers. The LL chamber is connected with PM1 and PM2 chambers by two valves for transferring the samples from the central LL to PM1 and PM2. Sample transfer is automatic, through a robotic arm.

— Both deposition chambers PM1 and PM2 are equipped with a rotating sample-holder anode, in order to improve as much as possible the uniformity of the deposition. The anode is also electrically isolated for allowing the application of a bias voltage on the substrates, during rotation. On the anode a set of heating lamps for heating substrates at temperatures up to 800°C is mounted. A thermocouple sensor monitors and controls the temperature set-point value.

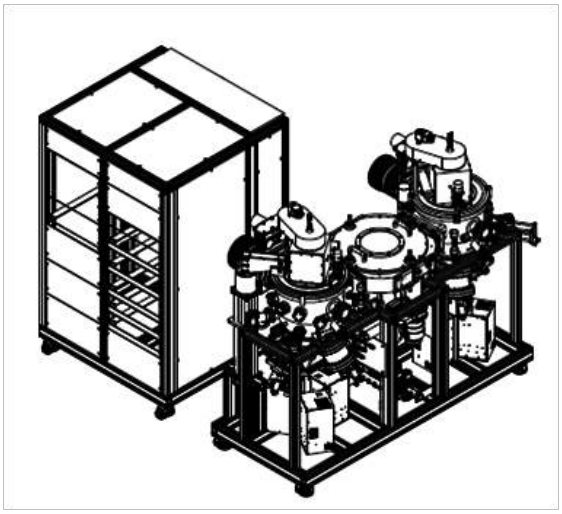

Figure 3.4. View of the KS 300 CONFOCAL Dual co-sputter system.

Depending on the process chamber, this system allows the deposition of different kind of materials. Chamber PM1 is used for the deposition of metals and nitrides, while chamber PM2 is designed to perform oxides deposition. In the following, a detailed description of each deposition chamber will be provided.

Load-lock chamber The load-lock (LL) deposition chamber is made of aluminum and is placed in the central part of the co-sputter system. It is designed to allow the insertion and extraction of samples before and after a deposition process, through an automatic process for moving the samples from one chamber to the others, without breaking the high vacuum conditions of the deposition chambers and also with the aim of preventing as much as possible the introduction of contaminants, pollutants and moisture. The LL chamber is equipped with a proper two-stage vacuum system, with the aim of quickly restore high-vacuum conditions before transferring the samples into one of the two process chambers, or when transferring a sample from one chamber to the other, if consequential depositions have to be carried out. It is composed of a rotary and a turbomolecular pumps, characterized by nominal pumping speeds

of 16 m^3/h and 150 l/s respectively. A pair of electro-pneumatic valves separates the LL chamber from PM1 and PM2 chambers.

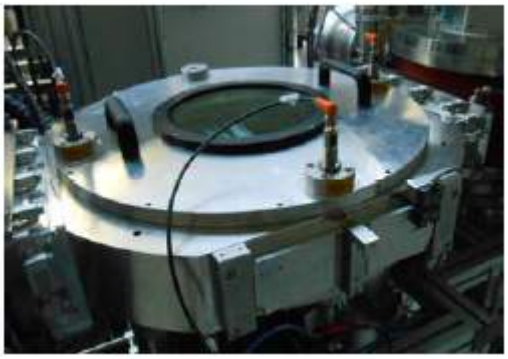

Figure 3.5. View of the load-lock chamber.

Figure 3.6. PM1 cathodes.

Deposition chamber for metals and nitrides PM1 is a cylindrical electropolished stainless steel (AISI 304) deposition chamber (400 mm diameter, 450 mm height), designed for the deposition of metals and nitrides. The chamber is equipped by three magnetron water-cooled cathodes, shown in Fig. 3.6. The two cathodes 2" diameter and the one 3" diameter are mounted on the lower part of the reactor, facing upwards to the anode ("sputter up" configuration). The cathodes are placed in a confocal geometry with the possibility of varying the tilt angle up to 15°. To prevent cross-contamination between targets when performing co-sputtering, each cathode is enclosed by special shields and a shutter. In PM1 a handling system is present on the 3" diameter cathode. The distance of the cathode from the anode can be adjusted through lamellar metallic bellows and precision manipulator, in order to vary the distance from the substrates of about 50 mm. Reactor walls are equipped with silicone rubber bands in order to perform the bakeout of the chamber and promote degassing of the walls, with the aim of improving vacuum conditions. Screen-printed resistors

incorporated in the bands allow to perfectly fit with the shape of the chamber, in order to get a uniform heating. The set-point temperature and control is obtained by a thermocouple sensor incorporated in the bands. The sample holder is designed for allowing depositions on 6" silicon wafers, and is able to rotate at a maximum rotational speed of 20 rpm. A heating system is placed in the upper part of the chamber, directly onto the sample holder, and can reach temperatures up to 800°C. The sample holder is connected to a DC power supply, in order to provide a DC polarization voltage to the substrates. An automatic shutter is also present on the sample holder, to avoid contamination of substrates during pre-sputtering processes. All the three cathodes are connected to a RF power supply, working at a frequency value of 13.56 MHz. One of the two 2" diameter cathodes can be also manually switched and connected to a DC power supply. Suitable vacuum conditions in PM1 can be reached by a two-stage pumping system, capable of reaching vacuum levels around $2 \cdot 10^{-7}$ mbar after 5 hours pumping. It is composed by a rotary and a turbomolecular pumps, with nominal pumping speeds of 25 m^3/h and 700 l/s respectively. Gas flows are properly controlled by a set of mass flow controllers.

Deposition chamber for oxides PM2 is the process chamber designed for oxides deposition. All the geometrical and functional features are the same of PM1, except for the cathodes dimensions; in the case of PM2, all the magnetron cathodes are 3" diameter.

Bibliography

[1] K. Wasa, M. Kitabatake, and H. Adachi, *Thin Film Materials and Devices*, in *Thin Film Materials Technology - Sputtering of Compound Materials*, William Andrew Publishing, Norwick (NY)/Springer-Verlag Heidelberg (Germany) (2004) p. 1.

[2] K. Wasa, M. Kitabatake, and H. Adachi, *Thin Film Materials and Devices*, in *Thin Film Materials Technology - Sputtering of Compound Materials*, William Andrew Publishing, Norwick (NY)/Springer-Verlag Heidelberg (Germany) (2004) p. 18.

[3] H. Luth, *Adsorption on Solid Surafces in Surfaces and Interfaces of Solid Materials*, 3rd Edition, Springer-Verlag Berlin Heidelberg New York (1995) p. 490.

[4] H. Luth, *Adsorption on Solid Surafces in Surfaces and Interfaces of Solid Materials*, 3rd Edition, Springer-Verlag Berlin Heidelberg New York (1995) p. 496.

[5] H. Luth, *Adsorption on Solid Surafces in Surfaces and Interfaces of Solid Materials*, 3rd Edition, Springer-Verlag Berlin Heidelberg New York (1995) p. 492.

[6] H. Luth, *Solid Surfaces, Interfaces and Thin Films*, Fifth Edition, Springer-Verlag Berlin Heidelberg New York (2010) p. 89.

[7] K. Wasa, M. Kitabatake, and H. Adachi, *Thin Film Materials and Devices*, in *Thin Film Materials Technology - Sputtering of Compound Materials*, William Andrew Publishing, Norwick (NY)/Springer-Verlag Heidelberg (Germany) (2004) p. 18.

[8] K. Wasa, M. Kitabatake, and H. Adachi, *Thin Film Materials and Devices*, in *Thin Film Materials Technology - Sputtering of Compound Materials*, William Andrew Publishing, Norwick (NY)/Springer-Verlag Heidelberg (Germany) (2004) p. 19.

[9] H. Luth, *Solid Surfaces, Interfaces and Thin Films*, Fifth Edition, Springer-Verlag Berlin Heidelberg New York (2010) p. 90.

[10] H. Luth, *Solid Surfaces, Interfaces and Thin Films*, Fifth Edition, Springer-Verlag Berlin Heidelberg New York (2010) p. 91.

[11] H. Luth, *Solid Surfaces, Interfaces and Thin Films*, Fifth Edition, Springer-Verlag Berlin Heidelberg New York (2010) p. 92.

[12] K. Wasa, M. Kitabatake, and H. Adachi, *Thin Film Materials and Devices*, in *Thin Film Materials Technology - Sputtering of Compound Materials*, William Andrew Publishing, Norwick (NY)/Springer-Verlag Heidelberg (Germany) (2004) p. 39.

[13] K. Wasa, M. Kitabatake, and H. Adachi, *Thin Film Materials and Devices*, in *Thin Film Materials Technology - Sputtering of Compound Materials,* William Andrew Publishing, Norwick (NY)/Springer-Verlag Heidelberg (Germany) (2004) p. 98.

[14] K. Wasa, I. Kanno, and H. Kotera, *Handbook of Sputter Deposition Technology, Fundamentals and Applications for Functional Thin Films, Nano-Materials and MEMS*, 2nd Edition William Andrew Publishing, Norwick (NY) (2012) p. 297.

[15] K. Wasa, I. Kanno, and H. Kotera, *Handbook of Sputter Deposition Technology, Fundamentals and Applications for Functional Thin Films, Nano-Materials and MEMS*, 2nd Edition William Andrew Publishing, Norwick (NY) (2012) p. 298.

[16] K. Wasa, I. Kanno, and H. Kotera, *Handbook of Sputter Deposition Technology, Fundamentals and Applications for Functional Thin Films, Nano-Materials and MEMS*, 2nd Edition William Andrew Publishing, Norwick (NY) (2012) p. 302.

[17] K. Wasa, I. Kanno, and H. Kotera, *Handbook of Sputter Deposition Technology, Fundamentals and Applications for Functional Thin Films, Nano-Materials and MEMS*, 2nd Edition William Andrew Publishing, Norwick (NY) (2012) p. 303.

[18] K. Wasa, I. Kanno, and H. Kotera, *Handbook of Sputter Deposition Technology, Fundamentals and Applications for Functional Thin Films, Nano-Materials and MEMS*, 2nd Edition William Andrew Publishing, Norwick (NY) (2012) p. 304.

[19] K. Wasa, I. Kanno, and H. Kotera, *Handbook of Sputter Deposition Technology,*

Fundamentals and Applications for Functional Thin Films, Nano-Materials and MEMS, 2nd Edition William Andrew Publishing, Norwick (NY) (2012) p. 306.

[20] K. Wasa, I. Kanno, and H. Kotera, *Handbook of Sputter Deposition Technology, Fundamentals and Applications for Functional Thin Films, Nano-Materials and MEMS*, 2nd Edition William Andrew Publishing, Norwick (NY) (2012) p. 312.

[21] K. Wasa, I. Kanno, and H. Kotera, *Handbook of Sputter Deposition Technology, Fundamentals and Applications for Functional Thin Films, Nano-Materials and MEMS*, 2nd Edition William Andrew Publishing, Norwick (NY) (2012) p. 313.

[22] K. Wasa, M. Kitabatake, and H. Adachi, *Thin Film Materials and Devices*, in *Thin Film Materials Technology - Sputtering of Compound Materials*, William Andrew Publishing, Norwick (NY)/Springer-Verlag Heidelberg (Germany) (2004) p. 39.

[23] K. Wasa, M. Kitabatake, and H. Adachi, *Thin Film Materials and Devices*, in *Thin Film Materials Technology - Sputtering of Compound Materials*, William Andrew Publishing, Norwick (NY)/Springer-Verlag Heidelberg (Germany) (2004) p. 136.

[24] K. Wasa, M. Kitabatake, and H. Adachi, *Thin Film Materials and Devices*, in *Thin Film Materials Technology - Sputtering of Compound Materials*, William Andrew Publishing, Norwick (NY)/Springer-Verlag Heidelberg (Germany) (2004) p. 40.

[25] K. Wasa, M. Kitabatake, and H. Adachi, *Thin Film Materials and Devices*, in *Thin Film Materials Technology - Sputtering of Compound Materials*, William Andrew Publishing, Norwick (NY)/Springer-Verlag Heidelberg (Germany) (2004) p. 137-139.

[26] K. Wasa, M. Kitabatake, and H. Adachi, *Thin Film Materials and Devices*, in *Thin Film Materials Technology - Sputtering of Compound Materials*, William Andrew Publishing, Norwick (NY)/Springer-Verlag Heidelberg (Germany) (2004) p. 40-41.

[27] K. Wasa, M. Kitabatake, and H. Adachi, *Thin Film Materials and Devices*, in *Thin Film Materials Technology - Sputtering of Compound Materials*, William Andrew Publishing, Norwick (NY)/Springer-Verlag Heidelberg (Germany) (2004) p. 148.

[28] K. Wasa, M. Kitabatake, and H. Adachi, *Thin Film Materials and Devices*, in *Thin Film Materials Technology - Sputtering of Compound Materials*, William Andrew Publishing, Norwick (NY)/Springer-Verlag Heidelberg (Germany) (2004) p. 42.

[29] K. Wasa, M. Kitabatake, and H. Adachi, *Thin Film Materials and Devices*, in *Thin Film Materials Technology - Sputtering of Compound Materials*, William Andrew Publishing, Norwick (NY)/Springer-Verlag Heidelberg (Germany) (2004) p. 151-152.

Chapter 4

Zinc Oxide

The material studied in this work is zinc oxide (ZnO). The aim of this chapter is to introduce and describe this material, considering its physical and chemical characteristics. The attention will be focused also on the analysis of the electrical and piezoelectric properties, both in undoped and doped ZnO. An overview on the properties and potential applications will be given, with a further insight about the doping of ZnO thin films.

4.1. Introduction

Among the large variety of semiconductor materials, zinc oxide (ZnO) is by far one of the most investigated, thanks to the possibility of combining its semiconducting behavior with its promising catalytic, electrical, optical and piezoelectric properties [1].

The interest in studying ZnO is not only related to its properties, but also to the possibility of combining its characteristics with different varieties of morphology. Indeed ZnO can be easily synthesized in a large amount of shapes and sizes, both at the micrometric and nanometric scale, including the forms of compact and porous thin films, micro and nano wires, nanobelts, nanorods, nanotubes, nanosprings, micro and nano particles, tetrapods, multipods and flower-like microstructures. All these different morphologies can be easily prepared by wet and dry synthesis techniques.

ZnO is a metal oxide semiconductor of II-IV group, whose nature resides at the borderline between ionic and covalent semiconductors [1]. It shows a wide band gap energy of 3.37 eV, a large exciton binding energy at room temperature (around 60 meV), absorption of light in the UV range, near UV and visible (500 - 600 nm) emission and a n-type semiconductor behavior, with a high electron mobility and high thermal conductivity [2, 3, 4]. Moreover it shows biocompatibility and low impact on the environment when being disposed at the end of its life cycle.

All these aspects make ZnO suitable for the fabrication of different kind of devices, such as solar cells, nanogenerators, FETs, gas and optical sensors, and other micro- and nano- devices [2, 5, 6]. In the last years the research field has focused particular attention on ZnO, with the aim of exploiting its piezoelectric behavior for the fabrication of nanoactuators, nanosensors and nanometric energy harvesting systems. Recently it has also been highlighted the possibility of combining both the semiconducting and piezoelectric properties in the so-called "piezotronic effect", where the charge carrier transport properties can be driven and tuned by the inner electric potential generated in ZnO thanks to the piezoelectric effect. Moreover, it has been also demonstrated the possibility of combining the optical properties with the piezoelectric ones, resulting in the so-called "piezo-phototronic effect" [7].

4.2. Crystal structure

The piezoelectric behavior of ZnO, as well as the other interesting physical properties, are due to the crystal structure of this semiconductor, which can take three different frameworks, shown in Fig. 4.1; rocksalt (B1), zinc blende (B3) and wurtzite (B4). Under ambient conditions, the thermodynamically stable

phase is the wurtzite structure. The zinc blende structure is on the contrary a metastable phase, which can be stabilized only in the case of growth on cubic symmetry substrates. The last phase, which is the rocksalt or Rochelle salt structure, can be obtained only working at relatively high pressures. ZnO is also known as zincite in the mineral form, and is very rare in nature. The characteristics deriving from the crystal structure make ZnO a material whose nature is considered to be at the border between the one of a covalent and ionic semiconductor.

When ZnO stabilizes in the wurtzite structure, the unit cell is hexagonal close-packed symmetry, and each Zn atom is surrounded by a tethraedron of four O atoms and viceversa. An alternated combination of different planes of Zn and O atoms is then formed and each Zn atom within ZnO is bound to the other four O atoms through sp^3 hybridization, in a tetrahedral configuration. This aspect is characteristic of covalent semiconductors. However the high band-gap energy is typical of solid materials with a high ionic component.

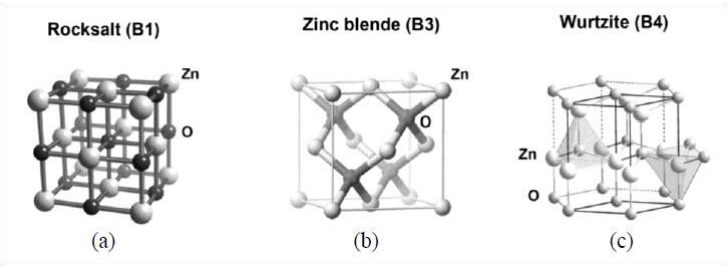

Figure 4.1. The crystal structures of ZnO: (a) rocksalt, (b) zinc blend, and (c) wurtzite unit cells. Grey spheres correspond to zinc atoms, black spheres to the oxygen ones [8].

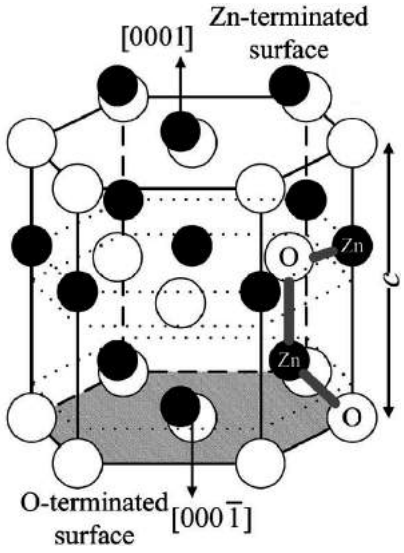

Figure 4.2. Wurtzite structure of ZnO with polar Zn- and O-terminated surfaces. The labeled four atoms indicate the primitive cell. Open and filled symbols represent oxygen and zinc ions, respectively [9].

All tetrahedra are oriented in one direction and their stacking produces the ZnO hexagonal symmetry. The alternation of Zn and O planes does not display

any center of inversion, and for this reason the wurtzite ZnO structure is intrinsically asymmetric along the c-axis, or [001] direction, so it is an anisotropic crystal.

The hexagonal prism of wurtzite structure always end with a (0001) oxygen plane at one side and a zinc plane on the other, because of the alternating presence of Zn and O planes. This situation is well-described in Fig. 4.2. Positive and negative polarities, i.e. the $\pm(0001)$ planes, are thus present at the two ends of the ZnO crystal. These $\pm(0001)$ surfaces show the highest surface energy and are metastable. The presence of this sequence of negative and positive polarities, together with the presence of asymmetry in the wurtzite crystal structure, is responsible for the intrinsic polarity of hexagonal wurtzite ZnO crystals and is at the base of the existence of piezoelectricity in ZnO.

The wurtzite crystal structure is characterized by two typical lattice parameters, which are labeled as c and a. The first represents the lattice distance between two first neighboring atoms. The second is representative of the basal plane length of the crystal, perpendicular to the crystal c-axis. X-Ray Diffraction performed with high-resolution measurements allows to estimate c and a values , and typical values of 3.2496 Å to 3.2501 Å for a and values ranging from 5.2042 Å to 5.241 Å for c were experimentally reported [10]. The presence of crystal defects such as dislocations, vacancies and interstitials causes a variation of c and a values from the one previously reported for the ideal case, and the c/a ratio can provide an estimation of the degree of deviation from the case of ideal structure. Among all the tetrahedrically coordinated semiconductors, ZnO is the one with the highest piezoelectric constants and electro-mechanical coupling coefficients. This aspect is related to the presence of a spontaneous polarization along the c-axis or [001] direction of the crystal (shown in Fig. 4.3), when a uniform mechanical stress is applied on the material. Therefore, in order to gain high piezoelectric constants in ZnO, the growth along the [001] direction must be pursued.

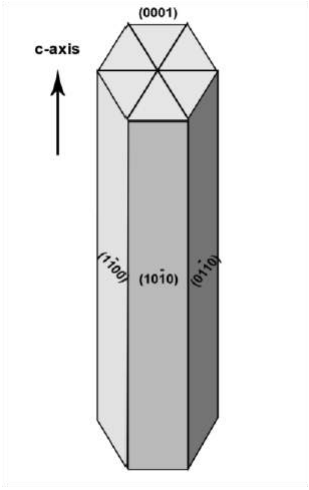

Figure 4.3. Wurtzite hexagonal crystal structure of ZnO [13].

4.3. Electrical and piezoelectric properties

ZnO is a well-known direct band gap semiconductor, where both the valence band maxima and the conduction band minima are positioned at the gamma point K=0 [11]. The band gap of ZnO is temperature dependent up to 300 K, and the value theoretically estimated is reported to be 3.77 eV. This is in good agreement with the 3.37 eV value experimentally obtained. This

large value also indicates that ZnO is a wide band gap semiconductor. The presence of a so high value, together with an unavoidable presence of electrically active native defects or impurities (typical donor ionization energies of 10-100 meV and concentrations of around 10^{15}-10^{16} cm^{-3}) [12], are the main reasons for the impurity-dominated n-type conductivity behavior of nominally undoped ZnO-based nanomaterials, which can thus be considered as transparent conducting oxide semiconductors. The electrically n-type behavior can also be enhanced by intentionally doping with elements like aluminum (Al), indium (In) and gallium (Ga), and carrier concentrations as high as 10^{21} cm^{-3} are reported from the literature [14]. At the moment, what is known about the electrical properties is based on n-type ZnO materials, as the preparation of "pure", intrinsic and accurately stoichiometric ZnO specimens is still a challenge for the materials scientists. In part this is because of the not sufficient amount of high-quality materials, as a consequence of the difficulty in achieving adequate oxygen incorporation into the specimens. Despite such a circumstance may seem a technological rather than a fundamental limitation, recently theoretical works suggest that the n-type behavior results from electrically active and stoichiometric native point defects [15, 16], such as vacancies, interstitials, and antisites. In addition, the unusually non amphoteric and donor-like character of unintentional but ever-present hydrogen can cause the n-type property of ZnO [17].

The presence of a non-centrosymmetric crystal structure is at the basis of ZnO piezoelectricity. Zn atoms, which are positively charged, are tetrahedrally bonded to the O atoms, which are negative charges, resulting in charge of the centers of gravity located in the crystal structure [2]. However, when a mechanical stimulus is applied to the material, a lattice deformation is generated and the positive and negative charge centers of gravity will no longer coincide. The crystal deformation consequent to the applied mechanical stimulus will thus induce a formation of a local electric dipole inside the cell. If all the cells have the same orientation and thus all the electric dipoles aligned, a macroscopic electric dipole inside the crystal is generated. Piezoelectric materials like ZnO are thus able to convert a mechanical deformation into an electric signal. This is known as direct piezoelectric effect. It is also possible the opposite situation, in which the application of a proper electric field to the piezoelectric material will generate a mechanical deformation of the crystal structure, caused by the motion of the ions inside the cell, which are sensitive to the applied electric field [2]. This is usually called converse piezoelectric effect. Combining the piezoelectric properties with the semiconducting ones, ZnO-based materials can be used in the fabrication of nanosensors, or as nanogenerators to harvest energy from surrounding environment, thus by converting mechanical deformation into electric potential [2, 18]. Fig. 4.4 shows all the possible configurations of both direct and converse piezoelectric effects, which are possible in the different piezoelectric materials.

The intrinsic n-type behavior of ZnO-based nanomaterials and the relatively high electrical conductivity has been widely exploited for the preparation of high transparent and conducting ZnO thin films, which have been successfully tested for different kind of applications where transparent electrodes are required. The n-type conductivity of ZnO can be properly increased by several order of magnitude by doping ZnO with III-group elements. The most common dopants used for this purpose are Al, In and Ga, as Zn-substitution, or Cl and I as O-substitution [20]. Indeed, all these elements behave as shallow donors in ZnO. Intentional n-type doping is thus a well-established technique, and carrier concentrations ranging between 10^{18} cm^{-3} and 10^{21} cm^{-3} have been obtained in the case of Ga or Al dopants (see Table 4.1). As stated before, the intrinsic n-type behavior of ZnO is generally ascribed to the presence of native defects such as Zn interstitials and O vacancies [21].

Despite this, these kind of defects are detrimental when p-type doping would

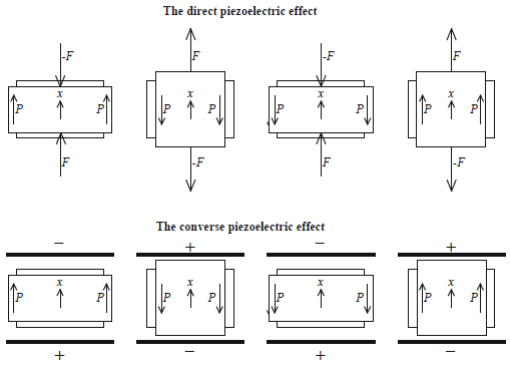

Figure 4.4. Direct and converse piezoelectric effects [19].

be pursued. Low-energy native defects like O vacancies or Zn interstitials can indeed compensate p-type dopants [21, 22]. This represents a drawback in obtaining stable and reliable p-type doped ZnO materials, and a real challenge in ZnO doping. Generally, I-group elements like Li, Na, K are the main dopants used as p-type acceptors, but also V-group elements, like N, P, As and Sb, are considered as a promising category of p-type dopants [22] (see Table 4.2). A general improvement in the electrical conductivity is thus obtained by doping ZnO with selected chemical elements.

Dopant	Carrier concentration [cm^{-3}]	Mobility [$cm^2V^{-1}s^{-1}$]
Al	$1.5 \cdot 10^{21}$	50
Ga	$1.33 \cdot 10^{18}$ - $1.13 \cdot 10^{20}$	51.1 - 120.5
Ga	$2 \cdot 10^{18}$ - $7 \cdot 10^{18}$	55 - 68

Table 4.1. Carrier concentration and mobility for n-type ZnO films grown by PVD techniques, using Al and Ga dopants [23].

Dopant	E_i[eV]	$\triangle$[eV]
Li	0.09	0.21
Na	0.17	1.04
K	0.32	1.38
N	0.40	0.13
P	0.93	-0.46
As	1.15	-0.18

Table 4.2. Defect energy levels (E_i) relative to the valence band maximum for negatively charged substitutional impurities, and the energy ($\triangle$E) required to form the positively charged center from the substitutional p-type doping [24].

The n-type intrinsic behavior of undoped ZnO nanomaterials, for selected applications, is however detrimental for the piezoelectric response, and doping of ZnO is also considered a powerful technique for improving the piezoelectric behavior of this material. Under specific doping conditions, the crystal cell of ZnO can be strained enough by the insertion of atoms with a proper ionic radius. The problems related to the choice of the right doping element, with a higher instead of a lower atomic dimension, is still under study, and contradictory results are reported in literature, showing that an improvement of the electromechanical response of doped ZnO thin films, and an increase of the d_{33} coefficient, can

be pursued in both cases [25, 26, 27, 28, 29]. Despite this consideration, the appearance of a ferroelectric behavior, together with the presence of a residual polarization in the doped materials, is observed in almost all the cases.

Among all the possible elements which can be used for doping ZnO, V, Mn, Cr, Fe and Cu are those which allowed to obtain a high increase in the piezoelectric response, together with ferroelectricity (see Table 4.3) [25, 26, 27, 28, 29]. The typical d_{33} value reported for undoped ZnO nanomaterials is in the range of tens of pmV^{-1}, and can slightly change depending on the particular kind of nanostructure. It is lower in ZnO thin films (12 pmV^{-1}) [30], but it is reported to increase up to 23 pmV^{-1} and 27 pmV^{-1} for ZnO nanobelts and for ZnO nanowires [31, 32], respectively. An increase by a hundred units in the piezoelectric coefficient d_{33} have been reported in the literature for doped ZnO thin films by using the aforementioned elements, suggesting that this method can be the right way for enhancing the piezoresponse of ZnO-based nanomaterials. This improvement seems to be related with the appearance of typical ferroelectric behavior [25, 26, 27, 28, 29]. Indeed, a typical butterfly loop in the displacement curves was observed for this kind of materials, together with the presence of a residual polarization and of hysteresis in the electrical polarization.

Dopant	d_{33}[pmV^{-1}]
-	12
V	110
Mn	86
Cr	120
Fe	200
Cu	13.5

Table 4.3. Enhanced d_{33} piezoelectric coefficient in doped ZnO thin films.

4.4. Sputter deposition of ZnO thin films

Among all the different morphologies, zinc oxide thin films have received much interest especially for their versatility and potential applications to microelectromechanical (MEMS) devices [33]. ZnO can be deposited by using different methods, such as chemical vapor deposition, molecular beam epitaxy, pulsed laser deposition, spray pyrolysis, direct current (DC) and radio frequency (RF) magnetron sputtering. Among all these technologies, the sputtering one is of great interest and widely diffused in thin film deposition, since it is based on a simple and relatively low-cost apparatus, where a large variety of materials can be deposited at low growth temperatures and with relatively high deposition rates [34]. The sputtering technique is widely used also for the deposition of ZnO thin films, mainly because of the easiness in achieving high-quality specimens, showing a preferential crystal orientation and uniform morphological properties, despite the low-temperature growth process. Moreover, the properties of sputtered ZnO thin films are known to be strictly influenced by the set of the deposition parameters used during the growth, such as the DC/RF power, gas pressure and flows, gas atmosphere and substrate temperature [35]. The physical properties of the resulting ZnO films can be thus controlled and properly tuned by simply changing one or more of the aforementioned parameters.

The possibility of controlling the crystal structure and morphology is of particular importance for growing high-quality piezoelectric ZnO films, especially in view of the fabrication of efficient, reliable and high performing devices. Another way of increasing the piezoelectric effect of ZnO is by increasing the electrical resistivity of the film [36]. Because of its wide band gap, ZnO should have an intrinsic resistivity exceeding 10^{20} Ω·cm. However, native defects (most

probably oxygen vacancies and/or zinc interstitials [37]) do not allow to reach such a high value. Defects concentrations and the structural quality of the film are thus important factors in this regard. Nevertheless, pure ZnO thin films, with resistivities ranging between 10^{-4} Ω·cm - 10^{13} Ω·cm have been reported [38, 39, 40].

Different works already reported in the literature about the deposition of ZnO thin films, demonstrating that both DC [36, 41, 42, 43, 44, 45] and RF [33, 46, 47] magnetron sputtering are eligible for growing high-quality thin films with a preferential orientation of the grains along the *c*-axis direction. DC-sputtered ZnO thin films are usually resistive [36], and with high texture if grown under low working pressures and by heating the substrates [48, 49]. ZnO depositions can be carried out by using a different composition of the gas species, namely in an inert argon atmosphere, or in a mixture of argon and oxygen. This last case is referred to as the reactive sputtering technique. The gas atmosphere is reported to affect the final characteristics of ZnO thin films. To this purpose, Tuzemen and Xiong et al. [44, 45] demonstrated that the conductivity of ZnO films could be changed from n-type at low ratio of O_2/Ar, to p-type by using a higher ratio of O_2/Ar. The gas atmosphere is found to influence also the final thickness of ZnO [34], decreasing with increasing the ratio of O_2/Ar. Also the gas pressure strongly influences the final characteristic of the material, especially concerning the crystal structure, the presence of stress and the surface morphology [33, 34]. In particular it is reported that working at pressures higher than 10^{-2} - 10^{-3} Torr involved the growth of amorphous thin films [50], while working with lower values is reported to improve the final crystal structure and stoichiometry. The crystal structure can be improved also by depositing at high substrate temperatures or by post-deposition thermal treatments [34, 46, 47]. In particular, crystals formed more tightly and uniformly with heat treatment under ambient air. The improvement of the crystal quality obtained by post-deposition annealing led also to an improvement of the optical properties of ZnO thin films [51, 52, 53, 54]. To this purpose, Fang et al. [51] deposited ZnO thin films by RF magnetron sputtering in an Ar + O_2 plasma at room temperature. The samples annealed below 600°C showed the higher (002) X-ray diffraction peak and the smaller root-mean-square surface roughness. Moreover the crystallite size and the density increased with increasing annealing temperature above 600°C.

In the last year, electronics on flexible substrates is becoming more and more interesting and a lot of efforts have been made to implement light-weight, flexible technologies for sensor arrays, curved circuits, curved detector arrays, sensor skins, and other large area electronics [55, 56, 57]. The use of plastic substrates is preferable in this case, since it provides devices that are lighter in weight and more resistant to impact damage, making them suitable for portable devices. The use of polymeric substrates for these applications, which have poor thermal endurance, implies more strict requirements concerning the PVD deposition of thin films, that should be deposited at low temperatures. The substrate materials, commonly used for the above applications include polycarbonate (PC), polyestersulfone (PES), polyimide (PI), polyethylene terephthalate (PET), polytetrafluoroethylene (PTFE), polyethylene naphthalate (PEN), etc. [58, 59, 60, 61, 62, 63]. Some of their thermal and mechanical characteristics are listed in Table 4.4.

Among the above materials, PET and PC are the most commonly used substrates in plastic display applications because of their superior optical properties over other polymer substrates, while PI is widely used thanks to its superior mechanical and thermal stability properties, in view of using high-temperature deposition processes. It is demonstrated that ZnO may be a suitable material for integration into flexible electronics platforms because it has good compatibility with plastic or flexible substrate materials [64].

Polymer	T_g[°C]	Tensile strength [MPa]
PC	150	70
PES	170	83
PI	360	280
PET	70	230
PTFE	115	43
PEN	120	280

Table 4.4. Typical glass-temperature (T_g) and tensile strength values reported for some class of polymers.

Many researchers have grown ZnO on different kind of the aforementioned polymeric flexible substrates. Mofor and coworkers reported on the successful deposition of ZnO layers on PI foil of 125 μm thickness [65]. This foil can be used on long-term basis up to a temperature of 230°C, being able of supporting higher temperatures for the ZnO deposition. Furthermore, they also demonstrated that the ZnO layer on the polymer foil is structured lithographically for device realization, showing a total compatibility with semiconductor technological processes like lithography.

Recently great attention was paid to the study of ZnO nanomaterials thanks to the coexistence of both semiconducting and piezoelectric properties, which can be exploited in the fabrication of sensors and energy harvesting systems of new generation. High piezoelectric coefficient d_{33} values, ranging from 14.3 pmV^{-1} to 26.7 pmV^{-1} were found in the characterization of ZnO nanobelts [31] while the first attempts of converting mechanical energy into electrical energy was carried out by means of ZnO NWs [32]. In addition flexible nanogenerators based on ZnO NWs were successfully demonstrated [66]. These results supported the application of ZnO nanostructures as nanosensors and nanogenerators. The possibility of regulating the charge-carrier transport properties in ZnO-based nanomaterials was also reported on either hard and flexible devices based on 1D ZnO nanostructures [67, 68]. Although 1D nanostructures are attractive for fundamental research studies, some limitations restrict their use in industrial applications. Indeed, the synthesis techniques for 1D nanostructures still do not guarantee sufficient uniformity of the as-grown materials, especially in terms of dimensions and morphology, with a strong lack of reproducibility and a worsening in the performance of the obtained devices. For this reason, the well-known thin film technology could be a valid alternative for the synthesis of piezoelectric materials, being fully compatible with the semiconductor technology and with the microfabrication processes. Piezoelectric ZnO thin films have been widely used for the fabrication of pressure sensors [69], actuators [70], ultra-high frequency surface acoustic wave devices [71], and energy harvesting architectures [72]. However, the piezoelectric properties and the charge-generation phenomena of this semiconductor are still under investigation. Recently, the piezoelectric response of porous ZnO films was successfully demonstrated [73]. However, the presence of a polycrystalline structure in this case is expected to lower the piezoresponse, since highly (002) oriented ZnO films, together with a compact nanostructure, should be pursued in order to maximize the piezoelectricity of the material [74]. Sputtered ZnO thin films commonly grow with a preferential (002) crystal orientation, and d_{33} values ranging from 2 pmV^{-1} up to 12.4 pmV^{-1} were already reported for highly (002)-oriented ZnO films grown by different techniques [30] and analyzed by the Piezoresponse Force Microscopy (PFM), which is a commonly used technique for the investigation of the polarity distribution, local piezoelectric properties, and for the estimation of the longitudinal piezoelectric coefficient (d_{33}) [31, 75]. A helpful approach for maximizing the piezoelectric response of ZnO films is the use of thermal treatments, which are generally required in order to increase the resistivity of ZnO films and to promote their (002) crystal orientation [76]. However room-temperature depositions are

preferable in view of using polymeric substrates for the fabrication of flexible devices.

Energy harvesting from ambient environments is an attractive issue in scientific and industrial fields for the purpose of building self-powered systems. A piezoelectric nanogenerator is one promising way to scavenge the energy from various sources, including body movements, [77] waves, [78] sounds, [79] air/ liquid pressures, and heartbeats [80]. Thin-film based nanogenerators have been proven to be suitable for scavenging irregular mechanical sources from bending or rolling motions [81]. Wurtzite nanostructures based on ZnO are one of the piezoelectric materials that can be applied in piezoelectric energy generation, thanks to the presence of a non-centrosymmetric structure in the crystalline phase. The fabrication and characterization of a new flexible PET-based energy harvesting system was already reported [82]. It consisted of piezoelectric ZnO thin film on composite cantilevers. One of the advantages of the reported structure was the use of PET. The piezoelectric member active area on the PET substrate was reported to achieve a large displacement with low residual stress without the bending deformation. Compared with the conventional Silicon-On-Insulator structures or other metal substrates layer, a low elastic constant of the PET layer could get larger displacement. Another example showing the integration of piezoelectric ZnO thin films in flexible structures is reported by Kuoni et al., which successfully demonstrated the fabrication and characterization of ZnO thin film piezoelectric sensors on a PI membrane [83]. As a test device a differential pressure liquid flow sensor was fabricated. The pressure sensor membrane consisted of a thin PI sheet bonded to a Si wafer, and the sputtered ZnO piezoelectric thin film as the sensing material. The fabricated liquid flow sensor was tested with a piezoelectric micropump. The strain in the piezoelectric layer was modeled and a transverse piezoelectric coefficient of e_{31} = -0.294 Cm^{-2} was determined. The flow sensor was based on the measurement of the pressure across a fluidic restriction, without having a direct contact between the sensing material and the liquid probe.

One of the very successful applications of hexagonal ZnO films is when integrated in thin-film Surface Acoustic Wave (SAW) devices. Thin-film SAW devices need a piezoelectric thin film material [36], which is a natural property of ZnO because of its anisotropic wurtzite structure. As mentioned before, ZnO thin films grown by the sputtering technique have excellent qualities, such as a textured crystalline structure, oriented along the *c*-axis direction and surface smoothness [84]. All these characteristics allow to reach high effective surface wave coupling coefficients, often greater than 90% with respect to the theoretical value, and with a high reproducibility. Thanks to all these amazing properties, piezoelectric ZnO thin films have been deposited on glass and metal substrates by RF magnetron sputtering, and successfully applied to SAW filters, and for temperature-compensated electronic-watch oscillators. Piezoelectric ZnO thin films also found applications in the fabrication of impact sensors [85]. Joshy and coworkers reported about the fabrication of an impact sensing element based on a thin circular diaphragm of flexible Phynox alloy. The ZnO film, acting as the impact sensing layer, was deposited on to the Phynox alloy diaphragm by RF reactive magnetron sputtering. A d_{31} piezoelectric coefficient of 4.7 pmV^{-1} was estimated, and the resulting piezoelectric ZnO-based sensing element was properly packaged in a highly sensitive, reliable, and cost-effective housing system. Piezoelectric ZnO thin films deposited by the sputtering technique were successfully exploited also in the technology of microcantilevers, for nanoactuation and nanosensing [86, 87]. This technology can be also used for the estimation of the transverse d_{31} piezoelectric constant of ZnO. The calculated transverse piezoelectric constant d_{31} of the ZnO thin film reported from Wang and coworkers, for a Au/Ti/ZnO/Au/Ti/SiO_2/Si microcantilever structure, was around -3.27 pCN^{-1} [88]. The piezoelectric effect in sputter-deposited ZnO thin films was demonstrated to be exploited in the preparation of a tactile sensor array [89]. A 64-element piezoelectric tactile-sensor array, integrated on a silicon chip, was successfully fabricated and tested. The sensor array consisted

of 1 μm-thick sputtered ZnO piezoelectric capacitors in an 8 x 8 matrix, with each sensing element measuring 70 x 70 μm^2, and spaced with a pitch of 70 μm. Each sensor element was then connected to an on-chip NMOS buffer-amplifier. The measured piezoelectric coefficient d_{33} in the ZnO films was 14.4 pCN^{-1}.

Recently, it is growing up the interest in studying the memristive behavior of metal oxide materials in the form of thin film. Memristor devices have been rapidly getting popularity in the field of nonvolatile random access memory (RAM) devices, making its scope applicable towards sensitive research areas like neural networks, image processing, and artificial intelligence [90, 91, 92, 93]. Memristor, also known as memory resistor, has the potential to replace several transistors mainly because of its reduced dimensions and low power consumption [94, 95]. It is considered to be the fourth passive element following resistor, capacitor, and inductor. Since Strukov et al. [96] succeeded in fabricating a memristor based on titanium dioxide film, many groups have been interested in this field. The memristor exhibits resistive switching effects, which have been observed in various material systems such as organic films [97, 98, 99, 100], chalcogenides [101, 102], and metal oxides [103, 104, 105, 106, 107]. Among the materials for Resistive RAM (ReRAM) application, metal oxides have attracted an increasing interest in material choice because of controllable compositions. The metal oxide thin film is usually deposited by electron beam evaporation, sputtering or atomic layer deposition, or by dip coating or spin casting [108, 109, 110, 111]. Moreover, various methods including doping [112], interface engineering [113] and nanoparticle incorporation [114, 115] were used to improve the performance of ReRAM devices. Making a high-quality metal oxide layer with a bistable resistance state is a key issue in achieving a high performance ReRAM device. A typical configuration of the ReRAM device usually consists of metal/insulator/metal structures, and the operation is based on the switching of high resistance state (HRS) and low resistance state (LRS) (off and on states) after a larger bias was applied, and due to the formation of a conductive bridge/path [116]. In general, the switching behaviors can be classified into two types in terms of current–voltage (I-V) behaviors, namely bipolar and unipolar switching [117, 118]. The bipolar resistive switching shows a directional resistive switching depending on the polarity of the applied voltage, while the unipolar resistive switching depends on the amplitude of the applied voltage without any polarity.

Among the resistance switching materials, ZnO is especially attractive for its several unique advantages, such as the coexistence of unipolar and bipolar switching behaviour [119, 120], the larger high resistance state to low resistance state (HRS/LRS) window and the transparent and flexible application aspects [119]. The doping method has already been adopted to optimize the switching performance of ZnO, including Ti, Mn, Co, Cu and Ga [119, 120, 121, 122, 123, 124], but the switching properties were not as optimized as for practical applications. Usually, ZnO is an n-type semiconductor oxide due to the presence of unintentionally introduced donor centers, which is identified as oxygen vacancies. Villafuerte et al. [120] reported the electric-pulse-induced resistance switching based on S and Co doped ZnO thin films using magnetron sputtering and laser ablation. The resistance ratio of HRS to LRS was less than 10. Peng et al. [121] studied the Mn-doped ZnO thin films, revealing the different mechanisms of resistive switching. Although the ZnO films have been studied before, there were still some issues: the resistance ratio of HRS to LRS was not high enough [125], electroforming process is required to initiate the resistive switching behavior [126], and especially, the mechanism of the memristive behavior has not been consentient. Although ZnO-based thin film ReRAM devices were found to have promising resistive switching characteristics with either unipolar or bipolar resistive switching behaviors, the detailed switching behavior is still not clear. The memristive switching behavior in metal oxides has been specifically attributed to the motion of oxygen vacancies [127]. Recently, the existence of conductive bridges/paths has been confirmed and observed by different methods. Pan et al. used transmission electron mi-

croscopy (TEM) to observe the formation of the conductive bridge/path in a Au/ZnO/Au system, after a couple of set/reset processes [128]. Takimoto et al. used conducting atomic force microscopy to locate the formation of the conducting filament [129]. However, these methods for the observation of the conducting filament formation can only be considered as ex-situ observations. Some controversies regarding resistive switching mechanisms remain, and the underlying physical mechanism of the resistive switching is still not fully understood. Consequently, a direct observation of conductive bridge/path formation in real time is imperative. Chang et al. reported about the resistive switching behavior observed in highly (002)-oriented and columnar-grained ZnO thin films prepared by radio frequency magnetron sputtering at room temperature [130]. The obtained Pt/ZnO/ Pt devices exhibited reversible and steady bistable resistance switching behaviors with a narrow dispersion of the resistance states and switching voltage. Only a low forming electric field was required to induce the resistive switching characteristics. The resistance ratios of HRS to LRS were in the range of 3 – 4 orders of magnitude within 100 cycles of test. It was also found that the conduction mechanisms dominating the low and high resistance states were Ohmic behavior and Poole-Frenkel emission, respectively. Further attempts to the study of ZnO memristive behavior, and the possibility of integrating into flexible structures, have also been reported. To this purpose, a resistive switching device based on Au/ZnO/stainless steel (SS) structures, and its applicability as a flexible ReRAM device was demonstrated [131]. The Au/ZnO/SS structure was fabricated by radio frequency sputtering deposition of a ZnO thin film on the SS substrate. The fabricated device showed stable unipolar and bipolar resistive switching behaviors with reliable switching responses over 100 cycles. The device performance was not degraded upon bending, indicating a high potential for flexible ReRAM applications.

Bibliography

[1] H. Morkoç, Ü. Özgür, *Zinc Oxide: Fundamentals, Materials and Device Technology* (2009) Wiley-WCH.

[2] Z. L. Wang, *Mater. Sci. Eng. R* **64** (2009) 33-71.

[3] Ü. Özgür, Y. I. Alivov, C. Liu, A. Teke, M. A. Reshchikov, S. Dogan, V. Avrutin, S. -J. Cho, and H. Morkoç, *J. Appl. Phys.* **98** (2005) 041301.

[4] Z. R. Tian, J. A. Voigt, J. Liu, B. McKenzie, M. J. McDermott, M. A. Rodriguez, H. Konishi, and H. Xu, *Nat. Mater.* **2** (2003) 821-826.

[5] J. Gomez, O. Tigli, *J. Mater. Sci.* **48** (2013) 612-624.

[6] Z. L. Wang, *J. Phys.: Condens. Matter.* **16** (2004) R829-R858.

[7] Z. L. Wang, *J. Phys. Chem. Lett.* **1** (2010) 1388-1393.

[8] C. Ottone, M. Laurenti, P. Motto, S. Stassi, D. Demarchi, and Valentina Cauda, *ZnO Nanowires: Synthesis Approaches and Electrical Properties. In: Nanowires. Synthesis, Electrical Properties and Uses in Biological Systems* Nova Publishers (2014) p. 2.

[9] L. Chun, G. Wanlin, K. Yong, and G. Huajian, *Appl. Phys. Lett.* **90** (2007) 033108.

[10] H. Morkoç, Ü. Özgür, *Zinc Oxide: Fundamentals, Materials and Device Technology* (2009) Wiley-WCH, p. 12.

[11] D. Vogel, P. Kruger, and J. Pollmann, *Phys. Rev. B* **52** (1995) 14316-14319.

[12] I. Broser, R. Broser, H. Finkenrath, R. R. Galazka, H. E. Gumlich, A. Hoffmann, J. Kossut, E. Mollwo, H. Nelkowski, G. Nimtz, W. v. d. Osten, M. Rosenzweig, H. J. Schulz, D. Theis, and D. Tschierse, *Semimagnetic Semiconductors* **17b** (1982) 543.

[13] C. Ottone, M. Laurenti, P. Motto, S. Stassi, D. Demarchi, and Valentina Cauda, *ZnO Nanowires: Synthesis Approaches and Electrical Properties. In: Nanowires. Synthesis, Electrical Properties and Uses in Biological Systems* Nova Publishers (2014) p. 3.

[14] T. Minami, H. Sato, H. Nanto,and S. Takata, *J. Appl. Phys.* **24** (1985) L781-L784.

[15] S. B. Zhang, S. H. Wei, and A. Zunger, *Phys. Rev. B* **63** (2001) 205.

[16] E. C. Lee, Y. S. Kim, Y. G. Jin, and K. J. Chang, *Phys. Rev. B* **64** (2001) 085120.

[17] C. G. Van de Walle, *Phys. Rev. Lett.* **85** (2000) 1012-1015.

[18] Z. L. Wang, *ACS Nano* **7** (2013) 9533-9557.

[19] J. Tichý, J. Erhart, E. Kittinger, and J. Přivratská, *Fundamentals of Piezoelectric Sensorics: Mechanical, Dielectric, and Thermodynamical Properties of Piezoelectric Materials* Springer-Verlag Berlin Heidelberg (2010) p. 2.

[20] H. Morkoç, Ü. Özgür, *Zinc Oxide: Fundamentals, Materials and Device Technology* (2009) Wiley-WCH, p. 245.

[21] H. Morkoç, Ü. Özgür, *Zinc Oxide: Fundamentals, Materials and Device Technology* (2009) Wiley-WCH, p. 246-247.

[22] H. Morkoç, Ü. Özgür, *Zinc Oxide: Fundamentals, Materials and Device Technology* (2009) Wiley-WCH, p. 250.

[23] H. Morkoç, Ü. Özgür, *Zinc Oxide: Fundamentals, Materials and Device Technology* (2009) Wiley-WCH, p. 248.

[24] H. Morkoç, Ü. Özgür, *Zinc Oxide: Fundamentals, Materials and Device Technology* (2009) Wiley-WCH, p. 252.

[25] Y. C. Yang, C. Song, X. H. Wang, F. Zeng, and F. Pan, *Appl. Phys. Lett.* **92** 012907 (2008);

[26] J. T. Luo, X. Y. Zhu, G. Chen, F. Zeng, and F. Pan, *Phys. Status Solidi R* **4** (2010) 209-211.

[27] Y. C. Yang, C. Song, X. H. Wang, F. Zeng, and F. Pan, *J. Appl. Phys.* **103** (2008) 074107.

[28] J. T. Luo, Y. C. Yang, X. Y. Zhu, G. Chen, F. Zeng, and F. Pan, *Phys. Rev. B* **82** (2010) 014116.
[29] X. B. Wang, D. M. Li, F. Zeng, and F Pan, *J. Phys. D: Appl. Phys.* **38** (2005) 4104-4108.
[30] I. K. Bdikin, J. Gracio, R. Ayouchi, R. Schwarz, and A. L. Kholkin, *Nanotechnology* **21** (2010) 235703.
[31] M. H. Zhao, Z. L. Wang, and S. X. Mao, *Nano Lett.* **4** (2004) 587-90.
[32] Z. L. Wang and J. Song, *Science* **312** (2006) 242-246.
[33] W.L. Dang, Y.Q. Fu, J.K. Luo, A.J. Flewitt, W.I. Milne, *Superlatt. Microstruct.* **42** (2007) 89-93.
[34] M. Li, N. Chokshi, R. L. DeLeon, G. Tompa, and W. A. Anderson, *Thin Solid Films* **515** (2007) 7357-7363.
[35] J.G.E. Gardeniers, Z.M. Rittersma, G.J. Burger, *J. Appl. Phys.* **83** (1998) 7844-7854.
[36] M. Hezam, N. Tabet, and A. Mekki, *Thin Solid Films* **518** (2010) e161-e164.
[37] S. -M. Lukas and J. L. MacManus-Driscoll, *Materials Today* **10** (2007) 40.
[38] T. Minami, H. Nanto and S. Takata, *Appl. Phys. Lett.* **41** (1982) 958.
[39] R. E. I. Schropp and A. Mada, *J. Appl. Phys.* **66** (1989) 2027.
[40] D. L. Raimondi and E. Kay, *J. Vac. Sci. Technol.* **7** (1969) 96.
[41] K.H. Yoon, J.W. Choi, and D.H. Lee, *Thin Solid Films* **302** (1997) 116.
[42] M.S. Oh, S.H. Kim, T.Y. Seong, *Appl. Phys. Lett.* **87** (2005) 122103.
[43] K. Nakamura, T. Shoji, and H. B. Kang, *Jpn. J. Appl. Phys.* **39** (2002) L534.
[44] S. Tuzemen, G. Xiong, J. Wilkinson, B. Mischuck, K. B. Ucer, and R. T. Williams, *Phys. B: Cond. Matt.* **1197** (2001) 308-310.
[45] G. Xiong, J. Wilkinson, B. Mischuck, S. Tuzemen, K. B. User, and R. T. Williams, *Appl. Phys. Lett.* **80** (2002) 1195.
[46] K.K. Kim, J.H. Song, H.J. Jung, W.K. Choi, S.J. Park, and J.H. Song, *J. Appl. Phys.* **87** (2000) 3573.
[47] K. K. Kim, J. H. Song, H. J. Jung,W. K. Choi, S. J. Park, J.H. Song, and J. Y. Lee, *J. Vac. Sci. Technol. A* **18** (2000) 2864.
[48] F. S. Hickernell, *Proceedings of the IEEE* **64** (1976) 631.
[49] H.L. Hartnagel, *Semiconducting Transparent Thin Films* Institute of Physics Publishing, 1995.
[50] O. Kappertz and R. Drese, *J. Vac. Sci. Technol. A* **20** (2002) 2084.
[51] Z. B. Fang, Z. J. Yan, Y. S. Tan, X. Q. Liu, and Y. Y. Wang, *Appl. Surf. Sci.* **241** (2005) 303.
[52] C. H. Choi, and S. H. Kim, *J. Cryst. Growth* **283** (2005) 170.
[53] K. Ozaki, and M. Gomi, *Jpn. J. Appl. Phys.* **41** (2002) 5614.
[54] M. K. Ryu, S. H. Lee, M. S. Jang, G. N. Panin, and T. W. Kang, *J. Appl. Phys.* **92** (2002) 154.
[55] H. Gleskova and S. Wagner, *IEEE Electron Device Lett.* **20** (1999) 473.
[56] S. Wagner, et al., *SPIE Symp. Proc.* **362** (2001) 19.
[57] P.I. Hsu, et al., *Appl. Phys. Lett.* **81** (2002) 1723.
[58] D. R. Cairns, D. C. Paine, and G. P. Crawford, *SID'01 Digest* (2001) 654.
[59] E. Lueder, *Proc. SPIE* **64** (1998) 3297.
[60] B. G. Lewis and D. C. Paine, *MRS Bull.* **25** (2000) 22.
[61] M.-A. Yanaka, Yutaka Kato, Y. Tsukahara, and N. Takeda, *Thin Solid Films* **337** (1999) 355-356.
[62] B. -S. Chiou and S. -T. Hseih, *Thin Solid Films* **229** (1993) 146.
[63] H. Gleskova, S. Wagner, and Z. Suo, *Appl. Phys. Lett.* **75** (1999) 3011.
[64] Y. -Y. Liu, Y. -L. Zang, G. -X. Wei, J. Li, X. -L. Fan, and C. -F. Cheng, *Mater. Lett.* **63** (2009) 2597-2599.
[65] A. C. Mofor, A. S. Bakin, B. Postels, M. Suleiman, A. Elshaer, and A. Waag, *Thin Solid Films* **516** (2008) 1401-1404.
[66] G. Zhu, R. Yang, S. Wang, and Z. L. Wang, *Nano Lett.* **10** (2010) 3151-3155.
[67] V. F. Rivera, F. Auras, P. Motto, S. Stassi, G. Canavese, E. Celasco, T. Bein, B. Onida, and V. Cauda, *Chem. Eur. J.* **19** (2013) 14665-14674.
[68] F. Xue, L. Zhang, W. Tang, C. Zhang, W. Du, and Z. L. Wang, *ACS Appl. Mater. Interf.* **6** (2014) 5955-5961.
[69] A. Kuoni, R. Holzherr, M. Boillat, and N. F. De Rooij, *J. Micromech. Microeng.* **13** (2003) S103-S107.
[70] T. Shibata, K. Unno, E. Makino, Y. Ito, and S. Shimada, *Sens. Actuat. A-Phys.* **102** (2002) 106-113.

[71] J. Molarius, J. Kaitila, T. Pensala, and M. Ylilammi, *J. Mater. Sci.: Mater. Electron.* **14** (2003) 431-435.
[72] D. Choi, K. Y. Lee, K. H. Lee, E. S. Kim, T. S. Kim, S. Y. Lee, S. -W. Kim, J. -Y. Choi, and J. M. Kim, *Nanotechnology* **21** (2010) 405503.
[73] R. Gazia, P. Motto, S. Stassi, A. Sacco, A. Virga, A. Lamberti, and G. Canavese, *Nano Energy* **2** (2013) 1294-1302.
[74] R. Gazia, G. Canavese, A. Chiodoni, A. Lamberti, S. Stassi, A. Sacco, S. Bianco, A. Virga, E. Tresso, and C. F. Pirri, *J. Alloys Compd.* **586** (2014) S331-S335.
[75] I. K. Bdikin, V. V. Shvartsman, and A. L. Kholkin, *Appl. Phys. Lett.* **83** (2003) 4232-4234.
[76] Y H. Hsu, J. Lin, and W. C. Tang, *J. Mater. Sci.: Mater. Electron.* **19** (2008) 653-661.
[77] R. Yang , Y. Qin , C. Li , G. Zhu , and X. D. Wang , *Nano Lett.* **9** (2009) 1201.
[78] X. Wang , J. Song , J. Liu , and Z. L. Wang , *Science* **316** (2007) 102.
[79] S. N. Cha , J. -S. Seo , S. M. Kim , H. J. Kim , Y. J. Park , S. -W. Kim , and J. M. Kim , *Adv. Mater.* **22** (2010) 4726 .
[80] Z. Li , and Z. L. Wang , *Adv. Mater.* **23** (2011) 84.
[81] Z. L. Wang , R. Yang , J. Zhou , Y. Qin , C. Xu , Y. Hu , and S. Xu , *Mater. Sci. Eng. R* **70** (2010) 320.
[82] C. T. Pan, Z. H. Liu, Y. C. Chen, and C. F. Liu, *Sens. Actuat. A-Phys.* **159** (2010) 96-104.
[83] A. Kuoni, R. Holzherr, M. Boillat, and N. F de Rooij, *J. Micromech. Microeng.* **13** (2003) S103–S107.
[84] T. Shiosaki, T. Yamamoto, A. Kawabata, R.S. Muller, and R.M. White, *IEEE Electron Devices Meeting* **25** (1979) 151-154.
[85] S. Joshi, G. M. Hegde, M. M. Nayak, and K. Rajanna, *Sens. Actuat. A-Phys.* **199** (2013) 272- 282.
[86] P. Wang, H. Du, S. Shen, M. Zhang, and B. Liu, *Nanoscale Res. Lett.* **7** (2012) 176.
[87] N. Gokhale, M. Parmar, K. Rajanna, and M. M.Nayak, *IEEE 3rd International Conference on Sensing Technology, Nov. 30 – Dec. 3, 2008, Tainan, Taiwan* (2008).
[88] P. Wang, H. Du, S. Shen, M. Zhang, and B. Liu, *Nanoscale Res. Lett.* **7** (2012) 176.
[89] D.L. Polla, W.T. Chang, R.S. Muller, R.M. White, *International Electron Devices Meeting* (1985), 133-136.
[90] Prodromakis, and C. Toumazou, *17th IEEE International Conference on Electronics, Circuits, and Systems (ICECS)* (2010) 934-937.
[91] B. Linares-Barranco, and T. Serrano-Gotarredona, *Nat. Prec.* hdl:10101/npre.2009.3010.1 (2009).
[92] L.O. Chua, *Cellular Nanoscale Sensory Wave Computing* Springer New York (1996).
[93] J. Hutchinson, C. Koch, J. Luo, and C. Mead, *Computer* **21** (1988) 52.
[94] L.O. Chua, *IEEE Trans. Circuit Theory* **18** (1971) 507.
[95] D. G. Strukov, G. S. Snider, D. R. Stewart, and S. R. Williams, *Nature* **80** (2008) 453.
[96] D. B. Strukov, G. S. Snider, D. R. Stewart, and R. S. Williams, *Nature* **453** (2008) 80-83.
[97] N. B. Zhitenev, A. Sidorenko, D.M. Tennant, and R. A. Cirelli, *Nat. Nanotechnol.* **2** (2007) 237-242.
[98] T. Berzina, A. Smerieri, M. Bernabo, A. Pucci, G. Ruggeri, V. Erokhin, and M. P. Fontana, *Appl. Phys.* **105** (2009) 124515-1–124515-5.
[99] J. C. Scott, and L. D. Bozano, *Adv. Mater.* **19** (2007) 1452-1463.
[100] S. Patil, Q. Lai, F. Marchioni, M. Jung, Z. Zhu, Y. Chen, and F. Wudl, *J. Mater. Chem.* **16** (2006) 4160-4164.
[101] R. Bhara, V. N. Singh, B. R. Mehta, and P. Datta, *Chalcogenide Lett.* **6** (2009) 189–196.
[102] X. Liu, M. T. Mayer, and D. Wang, *Appl. Phys. Lett.* **96** (2010) 223103-1–223103-3.
[103] R. Yasuhara, K. Fujiwara, K. Horiba, H. Kumigashira,M. Kotsugi,M. Oshima, and H. Takagi, *Appl. Phys. Lett.* **95** (2009) 012110-1–012110-3.
[104] D. Ielmini, F. Nardi, C. Cagli, andA. L. Lacaita, *IEEE Electron Device Lett.* **31** (2010) 353-355.
[105] B. J. Choi, D. S. Jeong, S. K. Kim, C. Rohde, S. Choi, J. H. Oh, H. J. Kim,

C. S. Hwang, K. Szot, R.Waser, B. Reichenberg, and S. Tiedke, *Appl. Phys.* **98** (2005) 033715-1–033715-10.

[106] A. Chen, S. Haddad, Y. C. Wu, T. N. Fang, S. Kaza, and Z. Lan, *Appl. Phys. Lett.* **92** (2008) 013503-1–013503-3.

[107] Y. P. Hai and W. Tom, *Appl. Phys. Lett.* **95** (2009) 152106-1–152106- 3.

[108] G. Jung, et al., *Nano Lett.* **6** (2006) 351.

[109] Q. F. Xia, J. J. Yang, W. Wu, X. Li, and R. S. Williams, *Nano Lett.* **10** (2010) 2909.

[110] F. Verbakel, S. C. J. Mesker, and R. A. J. Janssen, *J. Appl. Phys.* **102** (2007) 083701.

[111] J. Wang, B. Sun, F. Gao, and N. C. Greenham, *Phys. Status Solidi A* **207** (2010) 484.

[112] B. Gao, H. W. Zhang, S. Yu, B. Sun, L. F. Liu, X. Y. Liu, Y. Wang, R. Q. Han, J. F. Kang, B. Yu, and Y. Y. Wang, *IEEE Symposium on VLSI Technology* (2009) 30-31.

[113] A.Sawa, T. Fujii, M. Kawasaki, and Y. Tokura, *Appl. Phys. Lett.* **88** (2006) 232112-232114.

[114] W. -Y. Chang, K. -J. Cheng, J. -M. Tsai, and H. -J. Chen, *Appl. Phys. Lett.* **95** (2009) 042104-042106.

[115] J. H. Yoon, K. M. Kim, M. H. Lee, S. K. Kim, G. H. Kim, S. J. Song, J. Y. Seok, and C. S. Hwang, *Appl. Phys. Lett.* **97** (2010) 232904-232906.

[116] C. Y. Lin, D. Y. Lee, S. Y. Wang, C. C. Lin, and T. Y. Tseng, *Surf. Coat. Technol.* **203** (2008) 628-631.

[117] W. Shen, R. Dittmann, and R. Waser, *J. Appl. Phys.* **107** (2010) 094506.

[118] K. Kim, S. Park, S. G. Hahm, T. J. Lee, D. M. Kim, J. C. Kim, W. Kwon, Y. G. Ko, and M. Ree, *J. Phys. Chem. B* **113** (2009) 9143-9150.

[119] A. Younis, D. Chu, and S. Li, *Nanoscale Res. Lett.* **8** (2013) 154.

[120] M. Villafuerte, S. P. Heluani, G. Juarez, G. Simonelli, G. Braunstein, and S. Duhalde, *Appl. Phys. Lett.* **90** (2007) 052105-052107.

[121] H. Y. Peng, G. P. Li, J. Y. Ye, Z. P. Wei, Z. Zhang, D. D. Wang, G. Z. Xing, and T. Wua, *Appl. Phys. Lett.* **96** (2010) 192113.

[122] Y. C. Yang, F. Pan, F. Zeng, and M. Liu, *J. Appl. Phys.* **106** (2009) 123705-123709.

[123] K. Kinoshtia, T. Okutani, H. Tanaka, T. Hinoki, K. Yazawa, K. Ohmi, and S. Kishita, *Appl. Phys. Lett.* 96 (2010) 143505-143507.

[124] I. -C. Yao, D. -Y. Lee, T. -Y. Tseng, and P. Lin, *Nanotechnology* **23** (2012) 145201-145209.

[125] M. Villafuerte, S. P. Heluani, G. Juàrez, and G. Simonelli, *Appl. Phys. Lett.* **90** (2007) 052105-1–052105-3.

[126] W. Y. Chang, Y. C. Lai, T. B. Wu, S. F. Wang, F. Chen, and M. J. Tsai, *Appl. Phys. Lett.* **92** (2008) 022110-1– 022110-3.

[127] J. J. Yang, M. D. Pickett, X. Li, D. A. A. Ohlberg, D. R. Stewart, and R. S. William, *Nat. Nanotechnol.* **3** (2008) 429.

[128] C. -N. Peng, C. -W. Wang, T. -C. Chan, W. -Y. Chang, Y. -C. Wang, H. -W. Tsai, W. -W. Wu, L. -J. Chen, and Y. -L. Chueh, *Nanoscale Res. Lett.* **7** (2012) 559.

[129] N. Takimoto N, L. Wu, A. Ohira, Y. Takeoka, and M. Rikukawa, *Polymer* **50** (2009) 534-540.

[130] W. -Y. Chang, Y. -C. Lai, T. -B. Wu, S. -F. Wang, F. Chen, and M. -J. Tsai, *Appl. Phys. Lett.* **92** (2008) 022110.

[131] S. Lee, H. Kim, D. -J. Yun, S. -W. Rhee, and K. Yong, *Appl. Phys. Lett.* **95** (2009) 262113.

Chapter 5

Deposition and characterization of dense ZnO thin films on hard and flexible substrates

The aim of this chapter is to present all the scientific results about the deposition and characterization of dense ZnO thin films synthesized by the radio-frequency (RF) magnetron sputtering technique. Different deposition parameters were considered and ZnO thin films were first deposited on hard silicon substrates. The resulting samples were properly characterized in terms of their morphology, crystal structure and chemical composition. On the basis of the characterization results, the set of the optimal deposition parameters was selected and dense ZnO thin films with different thicknesses were deposited on hard and flexible conductive substrates, in order to perform the characterization of their piezoelectric and electrical properties.

5.1. Growth conditions

Dense ZnO thin films were deposited by the RF magnetron sputtering mono-target set-up, previously described (see Chapter 3, Section 3.3.1). Both hard and flexible substrates were used for this work. In particular, silicon (Si) wafers were first considered to provide a hard and flat substrate, and the preliminary characterization of the resulting ZnO/Si samples was performed. This allowed to select the optimal deposition parameters, able to give high-quality ZnO thin films. Then, hard Si/Ti/Au wafers and flexible Cu-coated polyimide (PI/Cu) foils were considered as conductive substrates, needed for the further characterization of the piezoelectric and electrical properties of ZnO thin films deposited with the best deposition parameters selected in the previous step. The set of all the deposition conditions and the average thickness of ZnO thin films deposited on Si and conductive substrates are summarized in Tables 5.1 and 5.2, respectively. All the depositions were carried out at room temperature, with a fixed working pressure value of $5 \cdot 10^{-3}$ Torr , and starting from a 4" diameter ceramic ZnO target (GoodFellow, 99.999% purity). Suitable vacuum conditions, with base pressures ranging between $1.7 \cdot 10^{-7}$ Torr and $4.9 \cdot 10^{-7}$ Torr, were achieved before starting each deposition process, by a two-stage pumping system.

Sample	RF power	Ar flow	O_2 flow	Deposition time	Average thickness
	[W]	[sccm]	[sccm]	[min]	[nm]
ZnO_30	30	40	-	60	80
ZnO_30_R	30	39	2	600	290
ZnO_50	50	40	-	60	210
ZnO_50_R	50	39	2	240	310
ZnO_100	100	40	-	60	800
ZnO_100_R	100	39	2	60	340

Table 5.1. Deposition conditions and average thicknesses of dense ZnO thin films deposited on Si substrates.

Sample	RF power	Ar flow	O_2 flow	Deposition time	Average thickness
	[W]	[sccm]	[sccm]	[min]	[nm]
ZnO_1h	100	39	2	60	285
ZnO_2h	100	39	2	120	710
ZnO_4h	100	39	2	240	1380

Table 5.2. Deposition conditions and average thicknesses of dense ZnO thin films deposited on hard Si/Ti/Au and flexible PI/Cu conductive substrates.

5.2. Analysis of ZnO thin films on silicon substrates

The set of the deposition conditions used for growing dense ZnO thin films on Si substrates is reported in Table 5.1. All the samples were characterized by means of Field Emission Scanning Electron Microscopy (FESEM) and X-Ray Diffraction (XRD) analysis, in order to evaluate the morphology and crystal structure, respectively. The depositions were performed in a pure Ar atmosphere or by the reactive sputtering technique. In this last case, a small percentage of a reactive gas (O_2) was added during the usual sputter deposition with Ar gas. The influence of the sputtering atmosphere on the chemical composition and stoichiometry of the resulting ZnO thin films was analyzed by X-ray Photoelectron Spectroscopy (XPS). On the basis of FESEM, XRD and XPS results, the optimal deposition parameters were selected, in order to get dense ZnO thin films with the right morphology, crystal orientation, chemical composition and stoichiometry.

5.2.1. Morphology analysis

The morphology and thickness of the samples were investigated using a Carl-Zeiss Dual Beam Auriga, consisting of a Field Emission Scanning Electron Microscope (FESEM) and Focused Ion Beam (FIB).

The surface morphology of ZnO thin films deposited at different RF power values, in a pure Ar atmosphere, is shown in Fig. 5.1. A rough surface, with great asperities, is present in the case of sample ZnO_100 (Fig. 5.1(a)), while it changes into a more regular and smooth one for samples ZnO_50 and ZnO_30 (Figs. 5.1(b) and 5.1(c), respectively).

A transition from a rough surface to a smooth one is then obtained when the RF power (and the deposition rate) decrease from 100 W to 30 W. The pronounced roughness of sample ZnO_100 can be ascribed to the high ionic bombardment of the surface during the deposition, caused by the high energy of the atoms impinging on the sample, and is related to the high RF power value used in this case. Moreover, when high-energy particles impinge on the surface of the substrate, their surface mobility is high enough to get the nucleation of big grains. The deposition rate is high in this condition, and when the deposition goes further, the grains can aggregate to each others into bigger ones, thanks to the high amount of particles arriving from the vapor phase. All these factors contribute to determine the surface morphology of sample ZnO_100, which is characterized by big and irregular grains, and promote the growth of a rough but very compact and dense nanostructured film.

When the RF power is lower, the ionic bombardment decreases, as also the deposition rate. The surface mobility of the adatoms is lower too, and they can aggregate into a higher number of grains, which are smaller in dimensions. The low deposition rate, characteristic of samples ZnO_50 and ZnO_30, also allows to growth crystal grains which are more regular in shape. These factors lead to ZnO thin films with a smooth surface and characterized by small, rounded grains, as clearly visible in Figs. 5.1(b) and 5.1(c), representative of samples ZnO_50 and ZnO_30, respectively.

The presence of a columnar growth is observed for all the three samples, independently of the power value used during the deposition. A section evidencing this aspect is reported in Fig. 5.1(d).

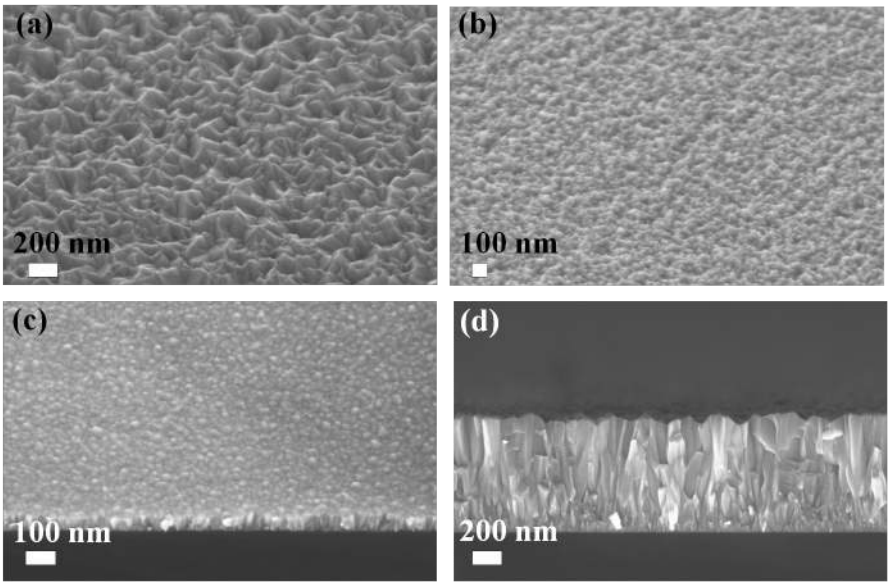

Figure 5.1. FESEM images of ZnO thin films deposited in a pure Ar atmosphere - Top view of samples (a) ZnO_100, (b) ZnO_50, and (c) ZnO_30; (d) cross-sectional image of sample ZnO_100.

Fig. 5.2 shows the FESEM images of ZnO thin films grown by the reactive sputtering technique. In all the cases the surface is characterized by small, densely-packed, rounded grains, with an average dimension comprised between 10 nm and 40 nm. The presence of a columnar growth, typical of sputter-deposited ZnO thin films and already observed for films deposited in an inert Ar atmosphere, is clearly visible from Fig. 5.2(d), and is representative of the preferential orientation of the ZnO films along the *c*-axis direction. This last aspect is further confirmed by the XRD results discussed in the next. Moreover, a strong decrease of the deposition rate can be noticed, if comparing the average thicknesses of ZnO films deposited in an inert and reactive atmosphere, reported in Table 5.1.

Comparing Figs. 5.1 and 5.2 it is clear the influence of the deposition atmosphere on the surface morphology of ZnO films. Despite the RF power value used during each deposition, the presence of a reactive atmosphere helps in growing thin films with a smooth surface, characterized by small, rounded grains. Indeed, this aspect is commonly present for all the samples grown by adding oxygen, as clearly visible from Fig. 5.2.

As reported before for ZnO films deposited in an inert atmosphere, the shape and size of the crystal grains are strongly affected by the RF power value used during the deposition. This aspect is observed also for ZnO films deposited by the reactive sputtering technique. Indeed, the average grains dimension decreases from sample ZnO_100_R deposited at the highest deposition rate (Fig. 5.2(a)), to samples ZnO_50_R and ZnO_30_R grown at lower RF power values, and shown in Figs. 5.2(b) and 5.2(c), respectively. Moreover, the presence of oxygen is considered to be the main factor influencing the grains shape, indeed when no oxygen is used, the shape of the grains results to be more irregular, as previously discussed.

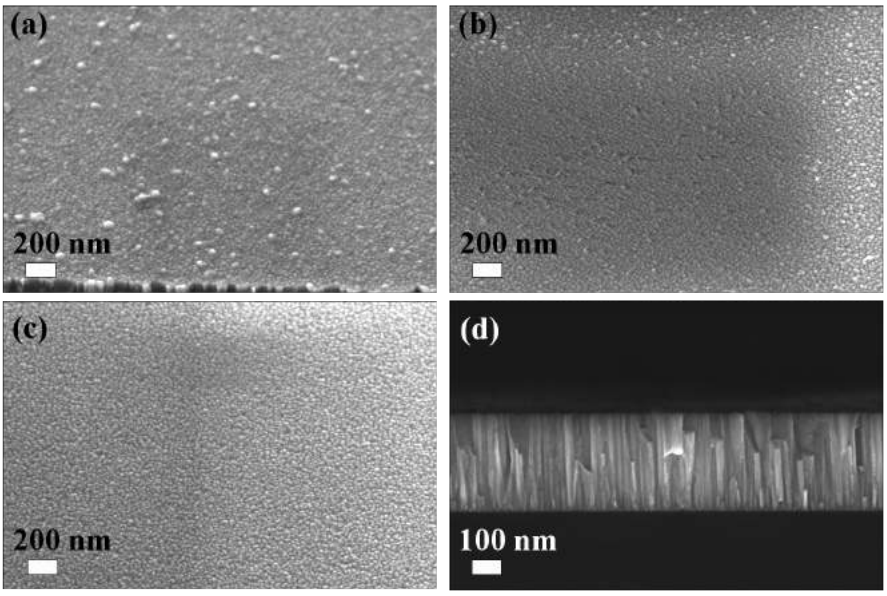

Figure 5.2. FESEM images of ZnO thin films deposited by the reactive sputtering technique - Top view of samples (a) ZnO_100_R, (b) ZnO_50_R, and (c) ZnO_30_R; (d) cross-sectional image of sample ZnO_100_R.

5.2.2. Structural characterization

The crystal structure and orientation of ZnO thin films were analyzed by X-Ray Diffraction (XRD) measurements using a Panalytical X'Pert X-ray diffractometer in the Bragg-Brentano configuration. A Cu K_α monochromatic radiation was used as X-ray source, with a characteristic wavelength $\lambda = 1.54059$ Å. The diffraction peaks position and the Full Width Half Maximum (FWHM) were properly estimated by a linear fit of each spectrum with a gaussian curve.

Highly (002), *c*-axis oriented ZnO thin films are desirable in order to enhance the piezoelectric response of the material [1]. Moreover, a high grain boundary density, characteristic of ZnO thin films with small crystallites, can be somehow detrimental. Indeed, grain boundaries act as trapping sites for the charge carriers, lowering the piezoresponse of ZnO. The different crystal structures of ZnO were previously described (Chapter 4). The most common crystal structure of ZnO thin films deposited by the sputtering technique is the hexagonal wurtzite-like, and generally the growth direction occurs along the *c*-axis. Fig. 5.3 shows the diffraction pattern of samples ZnO_100, ZnO_50 and ZnO_30. Only reflections coming from the (002) crystal planes are detected in all the cases, confirming the presence of the hexagonal wurtzite-like crystal structure and a preferential orientation along the *c*-axis direction. The (002) peak positions and the related FWHM values are reported in Fig. 5.4 for the samples grown in a pure Ar atmosphere. The different diffraction-peak positions are compared with the one reported by the International Center for Diffraction Data, for a randomly-oriented and crystalline ZnO sample. The (002) peak position assumed as reference in the present work for ZnO is 34.37°. All the films show the desired crystal structure and orientation, but some small differences can be appreciated. The (002) diffraction peak slightly shifts towards lower 2θ angles when the films are grown with lower RF power values, while the FWHM of the peaks increases. As the RF power value decreases, the deposition rate decreases too, and thinner films, with small crystallites are obtained, as evidenced from the FESEM characterization discussed in the previous Section 5.2.1. The observed shift towards lower 2θ angles for thinner films is generally due to the increase in uniform strain when the thickness of the film decreases [2]. Indeed,

the average thickness of samples ZnO_100, ZnO_50 and ZnO_30 is 800 nm, 210 nm and 80 nm, respectively. A general increase of the residual stresses can be expected passing from the thickest sample ZnO_100 to the thinnest one ZnO_30, and is confirmed from the XRD characterization results reported in Fig. 5.4.

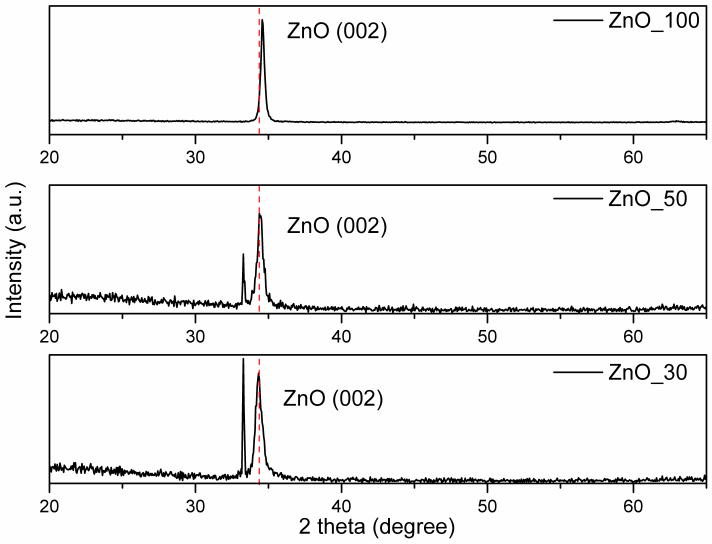

Figure 5.3. XRD pattern of dense ZnO thin films deposited in a pure Ar atmosphere. The narrow peak centered at 33.89° is related to the Si (400) diffraction contribution, coming from the substrate. The dashed red line represents the reference (002) peak position.

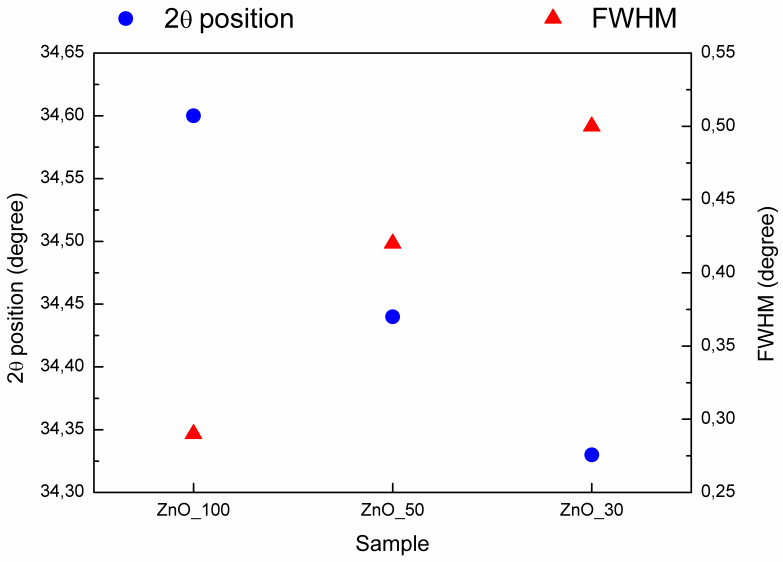

Figure 5.4. (002) diffraction peak positions and related FWHM values, measured for ZnO thin films deposited in a pure Ar atmosphere.

The increase in the film thickness as the deposition rate is raised produces less-defective films featuring larger crystallites [3, 4]. The FWHM depends on the presence of crystal defects; the lowest the FWHM, the highest the quality of the grown crystal planes, and the presence of defects in the ZnO crystal structure is lower too. All these aspects are observed in the present case. The lowest FWHM value of 0.29° is measured for the thickest sample ZnO_100, which is characterized by large crystallites and a more compact structure, as already observed from the FESEM characterization. The quality of the ZnO crystal structure is thus related both to the (002) peak position and to the FWHM value. From the previous considerations, the best quality of sample ZnO_100 can be underlined. Indeed it is characterized by the lowest FWHM value, meaning that a low amount of crystal defects is present in the material. Moreover, the (002) diffraction peak position is the closest one to the standard reference, indicating a lower presence of stresses.

The XRD pattern of ZnO_100_R, ZnO_50_R, and ZnO_30_R films deposited by the reactive sputtering technique are shown in Fig. 5.5. Also in this case, all the samples show the presence of the hexagonal wurtzite-like crystal structure and a preferential orientation along the *c*-axis direction, as confirmed by the presence of the (002) diffraction peak. The (002) peak position and FWHM of the samples grown using the reactive sputtering technique are shown in Fig. 5.6. The peak position of sample ZnO_100_R is in good agreement with the reference value (34.37°). The sample ZnO_30_R, on the contrary, shows the presence of a large amount of non-uniform stresses, with a 2θ angle moving towards higher values. The FWHM of samples ZnO_100_R, ZnO_50_R and ZnO_30_R is quite constant, with the lowest value reported for the sample ZnO_100_R. All the samples are characterized by a similar average thickness, changing from 285 nm of sample ZnO_30_R, to 340 nm of sample ZnO_100_R. Moreover, the surface morphology of all these films is similar, as already discussed in Section 5.2.1. A fine-grained, smooth surface, with small crystal grains is indeed observed for all the samples deposited with a reactive atmosphere. The low FWHM value of sample ZnO_100_R, however, suggests a lower presence of crystal defects with respect to the other samples, and the superior crystal quality of this sample can be underlined.

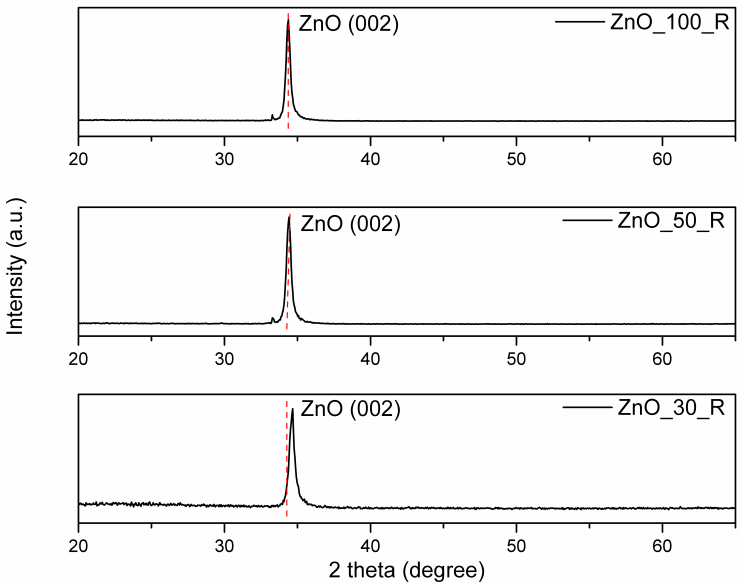

Figure 5.5. XRD pattern of ZnO thin films grown by the reactive sputtering technique. The dashed red line represents the reference (002) peak position.

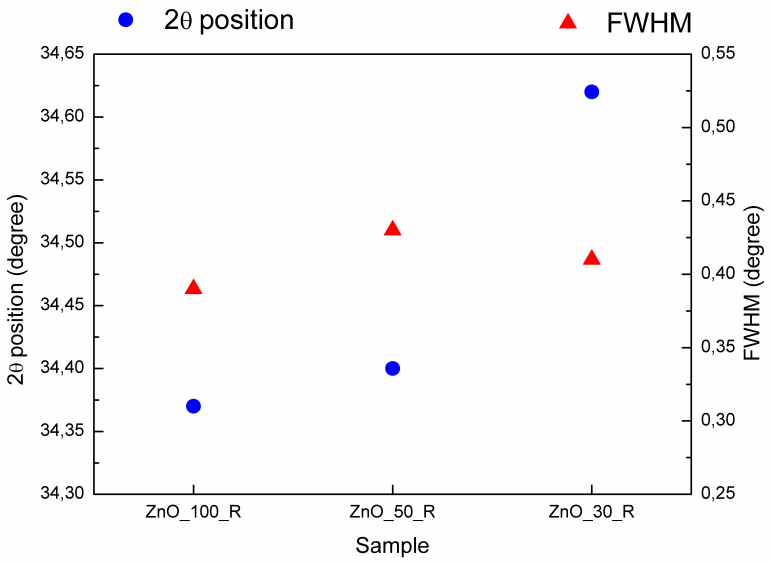

Figure 5.6. (002) diffraction peak positions and related FWHM values, measured for ZnO thin films deposited by the reactive sputtering technique.

Considering the XRD characterization results of all the ZnO thin films, the best crystal quality of samples ZnO_100 and ZnO_100_R, i.e., those grown with the highest deposition rate, can be underlined.

5.2.3. Chemical composition analysis

From the FESEM and XRD characterization results, the best quality of samples ZnO_100 and ZnO_100_R, i.e., those grown with the highest RF power value, can be evidenced. In order to better understand how the sputtering atmosphere can influence the chemical composition and stoichiometry of the resulting ZnO films, X-ray Photoelectron Spectroscopy (XPS) measurements were performed on these two samples by using a PHI 5000 VersaProbe (Physical Electronics) system, equipped with an Ar^+ gun, in order to remove any contaminant or pollutant from the surface of the analyzed materials. The X-ray source was a Al K_α radiation.

First, the survey spectra showing all the characteristics XPS spectra lines of each detected chemical elements composing the samples, and reported in Fig. 5.7, are collected. This preliminary analysis reveals just the presence of the expected Zn and O elements, while the little amount of carbon is due to the contaminants adsorbed on the analyzed area.

One of the factors influencing the characteristics of ZnO thin films is the chemical composition and stoichiometry. In a defect-free ZnO thin film, Zn and O atoms should be present in a 50% atomic percentage, with a stoichiometric ratio equal to one. However, the presence of a metallic phase due to an excess of Zn atoms is generally reported for sputter-deposited ZnO thin films [5]. The consequent oxygen deficiency can be detrimental, worsening the insulating behavior of this material and strongly limiting the piezoelectric response.

XPS analysis confirm that both the samples ZnO_100 and ZnO_100_R are far from the ideal stoichiometry. An excess of Zn atoms is pointed out from the quantitative compositional analysis, reported in Fig. 5.7. The Zn atomic percentage for sample ZnO_100 is reported to be around 55.3%, while it is lower for sample ZnO_100_R (52.7%). The amount of the metallic phase is thus expected to be lower for the sample ZnO_100_R.

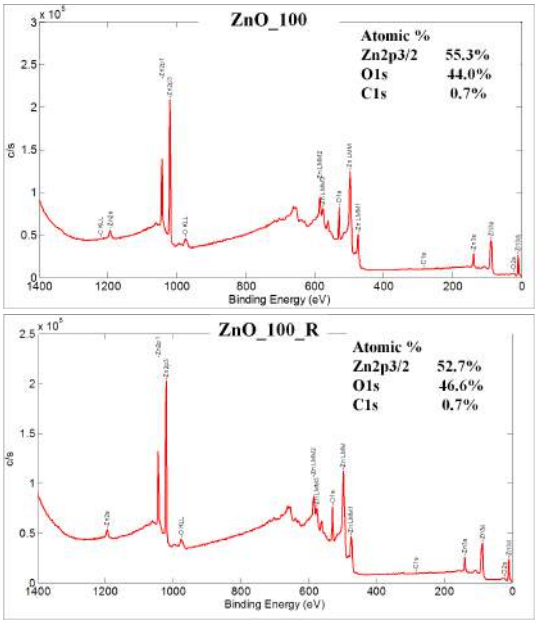

Figure 5.7. XPS survey spectra of samples ZnO_100 and ZnO_100_R.

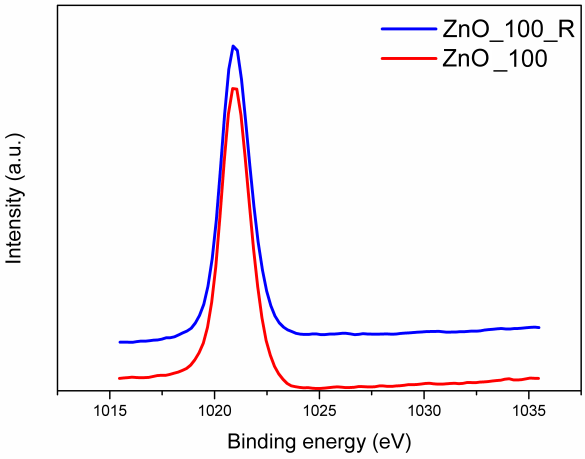

Figure 5.8. HR Zn_{2p} XPS spectrum of sample ZnO_100_R.

The stoichiometric ratio of each sample can be estimated by considering the high-resolution (HR) O_{1s} and Zn_{2p} XPS spectra, and computing the ratio of the area under the Zn_{2p} and O-Zn HR peaks. The HR Zn_{2p} spectra of samples ZnO_100 and ZnO_100_R are shown in Fig. 5.8, described by a single peak located at 1026.9 eV. This single peak is composed by two contributions, that is from Zn_{2p} core electrons involved in both Zn-O chemical bonds and the metallic Zn phase. However, these two contributions can not be distinguished, because their binding energies differ for a quantity that is lower than the instrumental resolution. The situation is different when considering the HR O_{1s} spectra. In this case the presence of different peaks can be observed, and each of them is related to a proper chemical bond involving oxygen atoms. The binding energy of these peaks can be properly extrapolated by fitting the HR O_{1s} curves, as

shown in Fig. 5.9. The binding energy is characteristic of each chemical bond, and can be properly identified by comparing the obtained value with those reported in the National Institute of Standards and Technology database. It comes out that oxygen atoms of samples ZnO_100 and ZnO_100_R can be bonded to Zn or hydrogen, and the binding energies obtained from the linear fit are listed in Table 5.3. Once the two different contributions are identified, i.e., the peaks associated to O-H and O-Zn chemical bonds, the area under the O-Zn peak can be computed and the stoichiometric ratio obtained for samples ZnO_100 and ZnO_100_R are 1.39 and 1.28 respectively.

Sample	Chemical bond	Binding energy [eV]
ZnO_100	O-Zn	529.7
	O-H	531.5
ZnO_100_R	O-Zn	529.8
	O-H	531.3

Table 5.3. Binding energy values of O_{1s} core electrons, for samples ZnO_100 and ZnO_100_R.

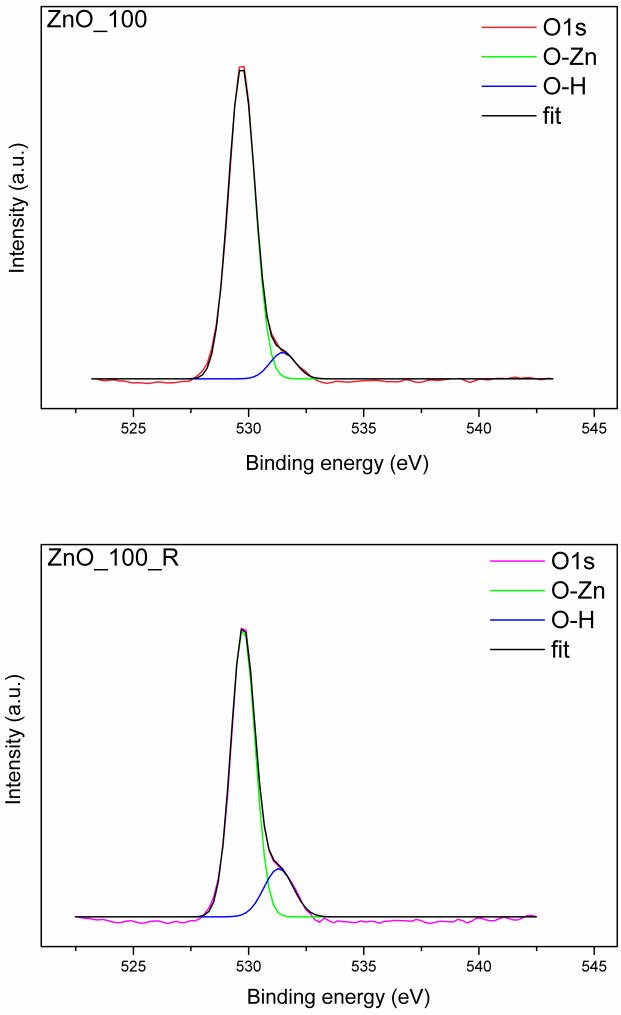

Figure 5.9. HR O_{1s} XPS spectrum of samples ZnO_100 and ZnO_100_R.

From the quantitative analysis described before, and from the estimation of the stoichiometry, it can be concluded that, even if an oxygen deficiency is still present in both cases, the sample ZnO_100_R grown with the reactive sputtering technique is closer to the ideal stoichiometry condition.

All these aspects, together with the high-quality of the crystal structure and morphology, allow to select the deposition conditions of sample ZnO_100_R as the optimal deposition parameters for obtaining highly (002)-oriented, nanostructured, dense ZnO thin films, with the best stoichiometry. The set of the parameters used for the deposition of this sample are thus selected for growing ZnO thin films on conductive substrates. In the next section, all the characterization results obtained for these samples will be discussed.

5.3. Analysis of ZnO thin films on hard and flexible conductive substrates

This section presents all the results obtained from the functional characterization of ZnO thin films deposited on both hard and flexible conductive substrates. In particular, silicon substrates covered with a 100 nm-thick titanium (Ti) / gold (Au) metallic layer were considered as flat conductive supports, on which the piezoelectric response of ZnO thin films with three different thicknesses was evaluated by Piezoresponse Force Microscopy. As flexible substrates, a commercial polyimide (PI) foil covered with a conductive copper (Cu) layer was considered, and these were used as flexible supports in order to show the possibility of integrating ZnO thin films in flexible devices. In this case, the charge generation coming from the exploitation of the direct piezoelectric effect was considered, and the piezoelectric output voltage generated under the application of a periodical mechanical deformation of the ZnO film was taken in consideration.

5.3.1. Morphology and structural analysis

Fig. 5.10 shows FESEM images of ZnO thin films deposited on hard and flexible substrates. The average grain size increases with increasing the film thickness. In the case of Si/Ti/Au substrates, a fine-grained, smooth surface, with small rounded grains (average grain size between 20 nm and 40 nm), together with the presence of some voids, is obtained for sample ZnO_1h (see Fig. 5.10(a)). When the film thickness is increased up to 710 nm, the ZnO surface is characterized by irregularly sized, densely packed grains, with no voids and an average dimension between 30 nm and 80 nm (see Fig. 5.10(b)). Fig. 5.10(c) shows the surface morphology of sample ZnO_4h. Despite the grain size does not further increase (the average grain size is similar to the one of sample ZnO_2h), a change in the grains shape can be highlighted. In particular, it can be observed that the crystal grains grow as long hexagonal rods for sample ZnO_4h, while circular grains are still present in samples ZnO_1h and ZnO_2h.

FESEM results of ZnO films deposited on PI/Cu foils are shown in Figs. 5.10(d) - 5.10(f). A strong influence on the ZnO morphology coming from the underlying PI/Cu foil is clearly observed, which decreases by increasing the ZnO thickness.

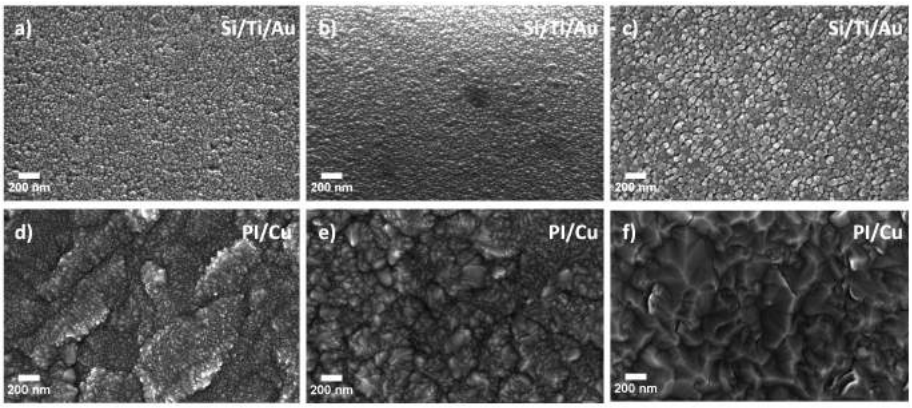

Figure 5.10. FESEM images of (a) - (d) ZnO_1h, (b) - (e) ZnO_2h, and (c) - (f) ZnO_4h samples, deposited on hard and flexible conductive substrates.

Indeed the surface morphology changes from the island-shaped small-crystal grains of samples ZnO_1h and ZnO_2h (see Figs. 5.10(d) and 5.10(e)) to the more compact and uniform one of sample ZnO_4h (see Fig. 5.10(f)). Basically the different morphologies observed in Fig. 5.10 can be related to the increase of ZnO film thickness. For thinner ZnO films (samples ZnO_1h), the surface is mainly formed by small grains. When the ZnO deposition goes on, it results in thicker films, and grains further grow in lateral size and height (samples ZnO_2h and ZnO_4h). These aspects are in accordance with the two-regimes growth model, already proposed by Vasco et al. [6]. Moreover a further influence of the underlying substrate on ZnO morphology is pointed out when PI/Cu foils are used (Fig. 5.11).

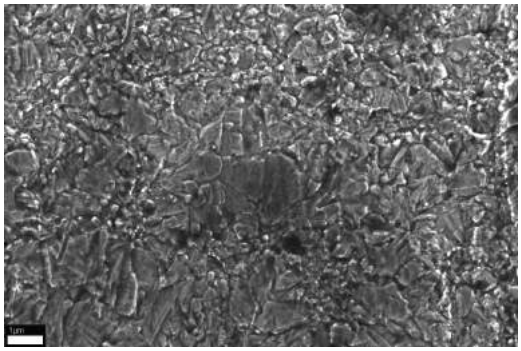

Figure 5.11. FESEM image of the Cu-coated PI foil used as a flexible conductive substrate for the deposition of ZnO films.

The XRD pattern of ZnO_1h, ZnO_2h and ZnO_4h films deposited on hard and flexible conductive substrates are shown in Figs. 5.12 and 5.13. Only reflections coming from the (002) crystal planes are detected in both cases, confirming that all the ZnO films exhibit the hexagonal wurtzite-like crystal structure, with a preferential orientation along the *c*-axis direction. Independently from the kind of substrate, the intensity of the (002) peak increases with increasing the film thickness. The (002) peak position for ZnO reported by JCPDS-ICDD (card n. 89-1397), and considered as reference in this work, is $2\theta = 34.37°$. Comparing this value with those reported in Table 5.4 it can be observed that the peak position of the thickest sample ZnO_4h (34.44°) is closer to the reference one while it slightly shifts towards higher 2θ angles for thinner films.

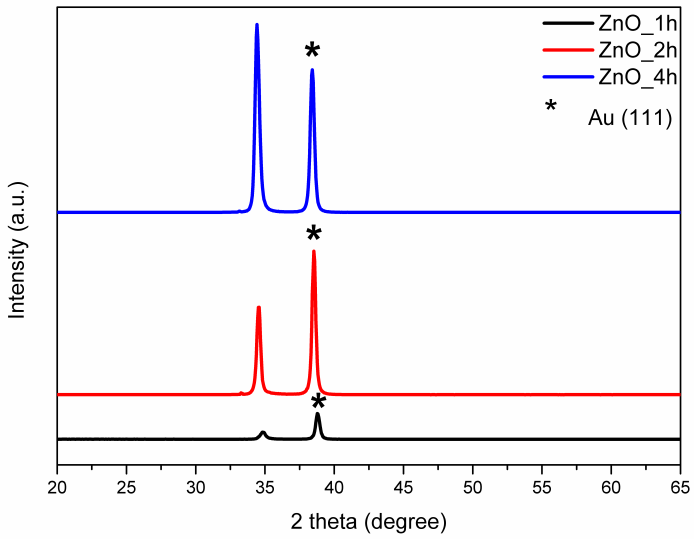

Figure 5.12. XRD spectra of ZnO_1h, ZnO_2h and ZnO_4h samples deposited on hard Si/Ti/Au conductive substrates.

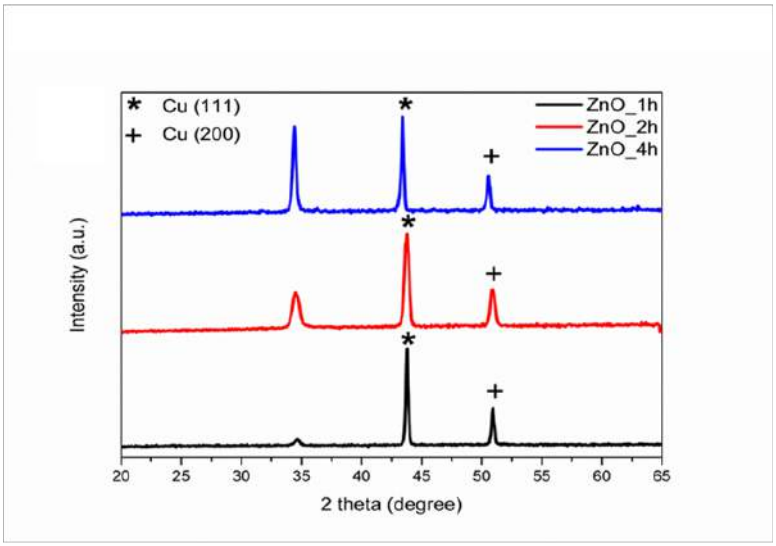

Figure 5.13. XRD spectra of ZnO_1h, ZnO_2h and ZnO_4h samples deposited on flexible PI/Cu conductive substrates.

Substrate	Sample	(002) peak position
Si/Ti/Au	ZnO_1h	34.86°
	ZnO_2h	34.72°
	ZnO_4h	34.44°
PI/Cu	ZnO_1h	34.62°
	ZnO_2h	34.54°
	ZnO_4h	34.43°

Table 5.4. XRD peak positions for ZnO thin films deposited on hard Si/Ti/Au substrates and flexible PI/Cu foils.

From Fig. 5.10 it can be pointed out that a high grain boundary density is present in the thinnest film, whereas it is lower for the other samples ZnO_2h and ZnO_4h, which are characterized by larger grains. It is reported that grain boundaries act as trapping sites for charge carriers. This aspect, together with the presence of a (002) preferential orientation, are believed to strongly influence the final piezoelectric response of ZnO film [1]. From XRD and FESEM characterizations, the high-quality of hard and flexible samples can be confirmed having highly (002)-oriented crystallites together with large and regular grains, characterized by a low grain boundary density.

5.3.2. Characterization of the piezoelectric properties

Piezoresponse Force Microscopy analysis

Piezoresponse Force Microscopy (PFM) measurements were performed in order to study the local piezoelectric properties of the sputtered ZnO thin films deposited on hard Si/Ti/Au substrates. For the measurements carried out in this work only the vertical displacement was considered, using the so-called single frequency PFM. In order to slightly enhance the piezoresponse, but avoiding excessive topographic cross-talk, the working frequency was set below the contact resonance (off peak). In this condition the amplitude signal can be related to the longitudinal piezoelectric coefficient d_{33} by estimating the quality factor Q, as described below. The experimental measurements were performed using MFP-3D (Asylum Research Inc., USA), at the first mode contact resonance of 300 kHz, with a Silicon Pt-coated cantilever (AC240TM Olympus "ElectriLever") with nominal stiffness of 2 N/m and a first mode resonance frequency of 70 kHz. In order to get a semi-quantitative information the PFM setup was calibrated on a standard sample and then the following measures performed in the same condition using the same tip. The Periodically Poled Lithium Niobate Test Sample (AR-PPLN) consists of a 3 mm x 3 mm $LiNbO_3$ transparent die that is 0.5 mm-thick. The active area is an alternating pattern of oppositely poled stripe domains that are parallel to one axis of the die and cover the entire die surface. The pitch of the domains is 10 μm. By comparing expected and measured vertical displacement on the reference test sample the Q factor was calculated. Thus assuming only vertical polarization, the piezoelectric constant d_{33} can be evaluated as:

$$d_{33} = A/(V_{AC} * Q)$$

, where A is the amplitude signal during scan, V_{AC} the alternate bias applied during scan and Q the quality factor, estimated on the reference sample as $Q \approx 10$.

PFM characterization highlighted the better piezoelectric properties of the sample ZnO_4h (i.e. the thickest film prepared with the longest sputtering time), with respect to the other samples. This sample presents a more uniform response over the whole scanned region and a higher value of d_{33} constant with respect to the ZnO_1h and ZnO_2h samples. Indeed, as underlined also by the XRD characterization, the thickest film has a high level of crystallinity, similar to the bulk material for what concerns the piezoelectric properties [7]. The d_{33} values estimated for the ZnO thin films on hard substrates are reported in Table 5.5 and are comparable with those already reported in literature for sputtered ZnO films.

Sample	Average thickness [nm]	d_{33}[pmV^{-1}]
ZnO_1h	285	5.0
ZnO_2h	710	5.3
ZnO_4h	1380	8.0

Table 5.5. Average d_{33} values of sputtered ZnO thin films with their different average thicknesses.

Fig. 5.14 shows the topography, the amplitude of the out-of-plane displacement and the phase obtained with PFM on the three samples. The bright area in the topography maps represents the top of the ZnO grains (or cluster of grains). These zones, compared with the amplitude image, result in the regions with the highest piezoresponse. In contrast, the regions around the top of the grains are darker in the amplitude map, since the piezoelectric properties are reduced or almost null in the proximity of the grain boundaries. All the piezoresponses are oriented in the same direction, because no phase shift is observable, most likely due to the controlled growth direction during deposition on the (002) crystal orientation. The average phase value on the grains is close to 0° indicating that the polarization vector is directed upward, parallel with the direction of the applied field between the tip and the substrate. The amplitude and phase images related to the thinnest samples (ZnO_1h) register a high cross-talk with the topography map, because of a strong electrostatic coupling between the metallic tip and the gold layer underneath. Despite this problem, from the measurements it is possible to evaluate the piezoelectric d_{33} constant and the surface roughness as RMS. The increase in surface roughness with increasing the thickness of ZnO films on hard substrates observed from the FESEM characterization is confirmed by PFM topographic images, which are shown in Fig. 5.14. The root mean square (RMS) values of roughness for samples ZnO_1h, ZnO_2h and ZnO_4h are 1.9 nm, 2.5 nm and 2.9 nm, respectively.

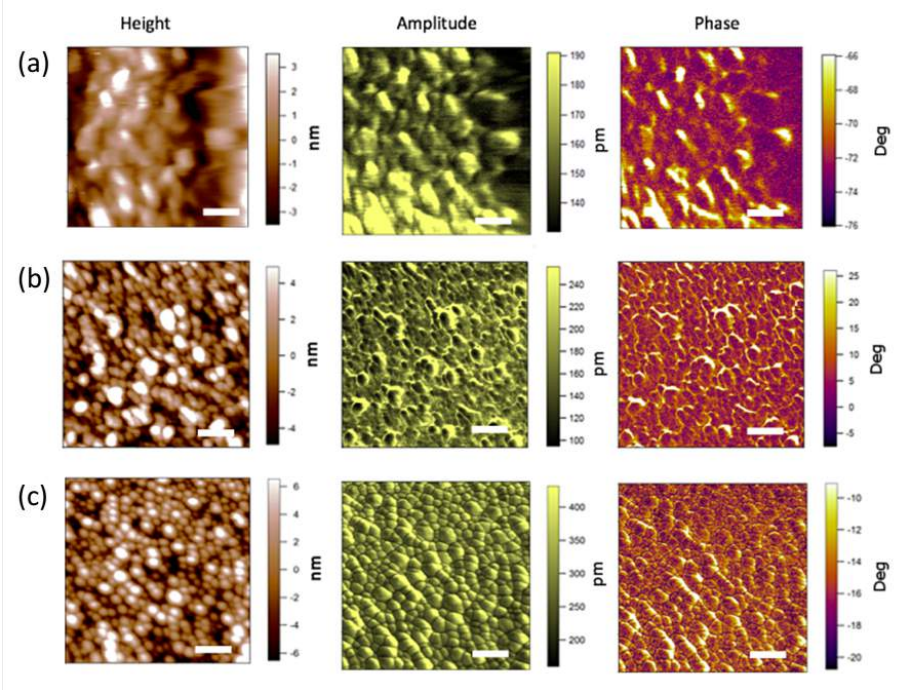

Figure 5.14. Vertical PFM scans of the (a) ZnO_1h, (b) ZnO_2h, and (c) ZnO_4h samples. In the three columns are presented, from left to right, the topography, amplitude and phase maps respectively. The maps correspond to a scanned area of 1 μm x 1 μm.

PFM spectroscopy was performed on the center of a ZnO grain of the sample ZnO_4h (Fig. 5.15(a)). The amplitude signal evidences the deformation of the crystalline cell under the effect of the applied electric field. From the slope of the amplitude curve in Fig. 5.15(b) it is possible to evaluate the d_{33} constant of this grain (8.7 pmV^{-1}) that is in line with the average piezoelectric properties computed from the amplitude image (Fig. 5.14(c)) and reported in Table 5.5. When the applied voltage has positive values, the ZnO grain locally expands, while when the voltage values become negative the material contracts and thus the phase has a switch of around 180° (as visible in the graph of Fig. 5.15(b)). Theoretically the phase inversion should happen at zero voltage value, as well as the amplitude response should be symmetric around this value. However, these behaviors are normally modified by surface charge defects that generate a local electric field in contrast or in phase with the tip applied signal [8]. This phenomenon is observable in the ZnO_4h spectroscopy graphs, where the inversion point occurs at around 1.5 V.

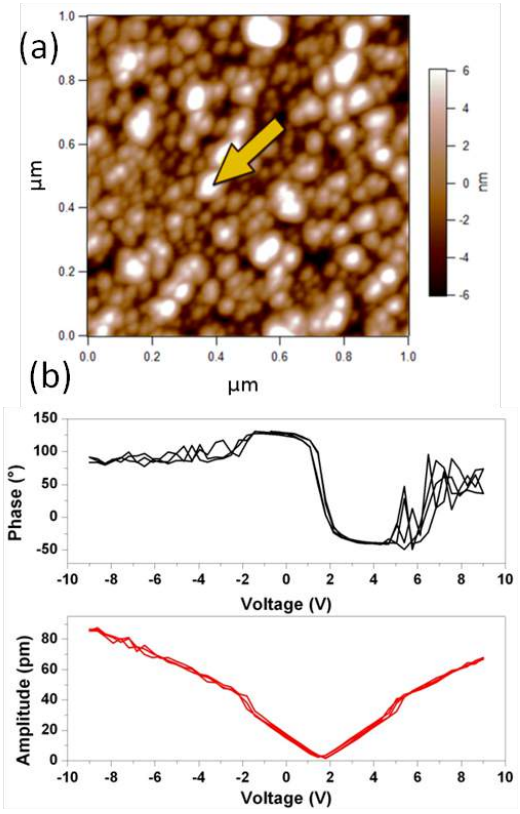

Figure 5.15. Single point spectroscopy performed on sample ZnO_4h. Phase (upper) and amplitude (lower) signals recorded applying a voltage sweep (5 cycles +/- 10 V) at 0.5 Hz. No sign of hysteresis appears in either amplitude or phase signal.

Direct piezoelectric response

Under the application of a periodical mechanical deformation, the piezoelectric thin film samples generate a synchronous voltage signal. Piezoelectric output voltage measurements were performed supplying the dynamic conditions to the ZnO film samples with a mechanical shaker (TV51110, Tira Gmbh, Germany). The shaker was driven at different voltages and frequencies by means of a function generator and a controller (VR 9500, Vibration Research, USA) in order to produce a cyclic force stimulus with the desired magnitude and period.

Force and acceleration were controlled with a load cell and an accelerometer screwed on the plate of the shaker (as shown in Fig. 5.16). The samples were attached to the plate and brought in compression during each cycle by pressing on a fixed metallic structure placed above the shaker, as shown in Fig. 5.17. The piezoelectric voltage from the ZnO film was recorded with a data acquisition board (NI BNC-2110, National Instruments, USA) in an open circuit configuration [9]. In order to avoid damages to the piezoelectric films and to the silicon substrates induced by the mechanical deformations, for these characterizations the ZnO samples prepared on flexible PI/Cu foils with and area of 10 mm x 10 mm were used and coupled to another PI/Cu foil, working as top electrode.

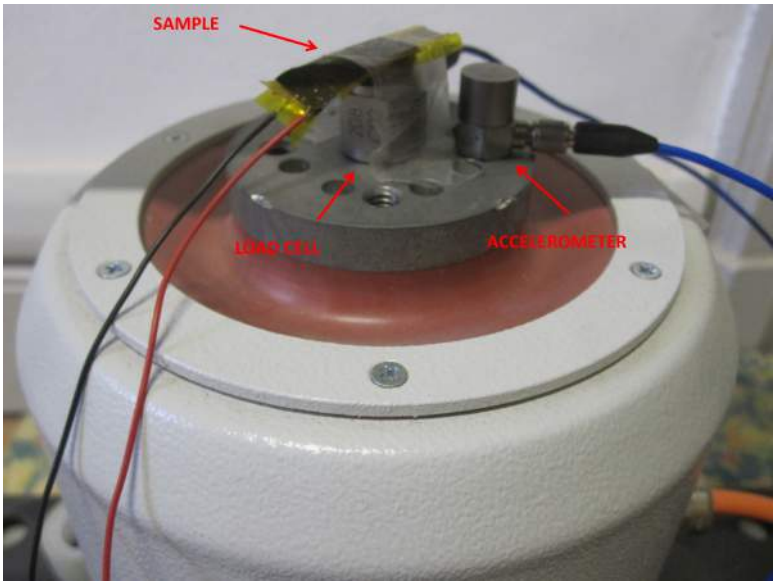

Figure 5.16. Image of the plate of the mechanical shaker with screwed the accelerometer and load cell sensors. The ZnO thin film sample is attached to the top of the load cell.

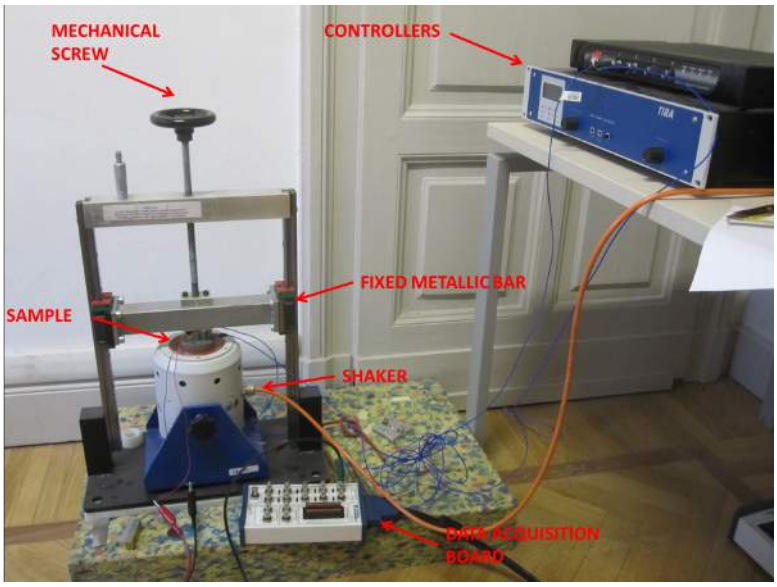

Figure 5.17. Image of the whole set-up for the piezoelectric output voltage generation measurements, including the mechanical shaker, the controllers, the data acquisition board and the fixed structure for compression measurements.

The high-quality of ZnO films deposited on flexible substrates is confirmed by FESEM and XRD measurements discussed before. These aspects, together with the PFM characterizations, suggest higher piezoelectric voltage generation for the thicker sample, as reported in Fig. 5.18(a).

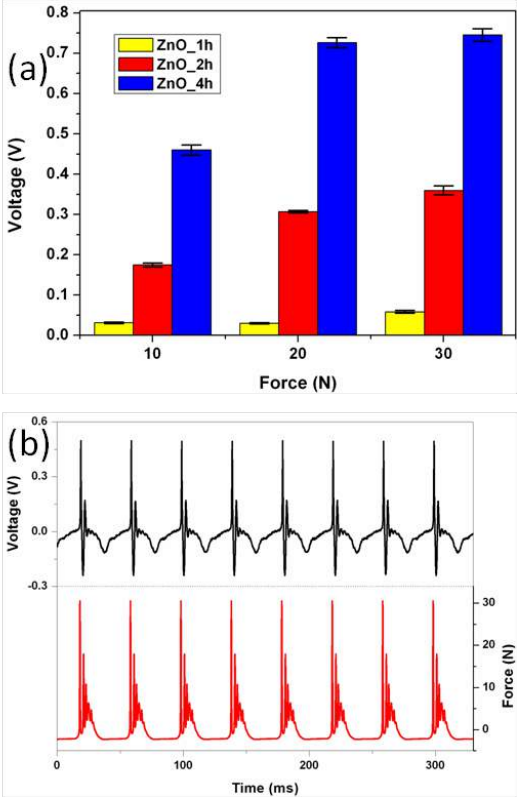

Figure 5.18. (a) Piezoelectric peak-to-peak voltage generation upon mechanical stimulation of the ZnO samples. (b) Piezoelectric voltage (up) as function of time generated by the ZnO_4h sample upon the application of a force signal (down).

The generated peak-to-peak voltage with a periodic mechanical stimulus of 30 N was 0.058 V for the ZnO_1h sample, 0.361 V for the ZnO_2h sample and 0.746 V for the ZnO_4h one. Comparing the generated voltage at 10, 20 and 30 N, the signal is not linear as expected, but tends to saturate for higher forces because of the shape of the mechanical applied stimulus. Indeed even if the actuation shaker signal had a sinusoidal shape, the force stimulus recorded by the load cell has the trend shown in Fig. 5.18(b), because of a recoil effect during the compression of the sample on the fixed bar that increases mutually with the force amplitude. When the sample is compressed against the fixed bar, the crystalline cell of the ZnO is deformed and the center of gravity of the negative charges will no longer coincide with the positive one, producing an electric dipole. This deformation will induce globally a generation of electric potential between the two faces of the piezoelectric thin film, moving the electrons inside the external circuit to compensate the piezoelectric potential. The variation of the force signal, due to the recoil effect and elastic properties of the material, will produce oscillation of the voltage signal up to the decompression step. Indeed when the stress is released, the electric dipole in the ZnO cell disappears and the electrons flow back through the external circuit producing a negative electrical potential.

5.4. Conclusions

In this chapter, all the scientific results obtained about the deposition and characterization of dense ZnO thin films were presented and discussed. ZnO thin films were first deposited on Si substrates by the RF sputtering technique. The morphology and crystal structure of the resulting samples was analyzed by means of FESEM and XRD measurements, while the chemical composition and stoichiometry of two different samples grown in different sputtering atmospheres were evaluated by XPS. On the basis of the characterization results, suitable deposition parameters were selected, in order to deposit high quality ZnO thin films, with a proper surface morphology, a *c*-axis oriented crystal structure, and the right stoichiometry. After this, hard and flexible conductive substrates were considered, and ZnO thin films with different thicknesses deposited with the set of the deposition parameters selected previously. The as-deposited films were characterized in terms of their morphology and crystal structure, just to check the quality of the samples. Then the piezoelectric behavior of ZnO films was analyzed by means of PFM and piezoelectric voltage generation measurements. Results showed that all the ZnO films are characterized by a good piezoelectric response, with a d_{33} piezoelectric coefficient value in agreement with those reported in literature and reaching a maximum value of 8.0 pm V^{-1} for the thickest ZnO film. Also piezoelectric output voltage measurements conducted on the flexible structures pointed out a good response of all the samples, with a maximum output voltage of 0.746 V obtained for the thickest sample. All these results encourage in exploiting and using dense ZnO thin films as high-performing, reliable functional materials, to be integrated in the fabrication of pressure sensors and for energy harvesting applications.

Bibliography

[1] J. G. E. Gardeniers, Z. M. Rittersma, and G. J. Burger, *J. Appl. Phys.* **83** (1998) 7844-7854.

[2] R. Menon, V. Gupta, H. H. Tan, K. Sreenivas, and C. Jagadish, *J. Appl. Phys.* **109** (2011) 064905.

[3] V. Tvarozek, I. Novotny, P. Sutta, S. Flickyngerova, K. Schtereva, and E. Vavrinsky, *Thin Solid Films* **515** (2007) 8756-8760.

[4] S. -S. Lin, J. -L. Huang, D. -F. Lii, *Surf. Coat. Technol.* **176** (2004) 173-181.

[5] K.G. Saw, K. Ibrahim, Y.T. Lim, and M.K. Chai, *Thin Solid Films* **515** (2007) 2879-2884.

[6] E. Vasco, J. Rubio-Zuazo, L. Vázquez, C. Prieto, and C. Zaldo, *J. Vac. Sci. Technol. B* **19** (2001) 224-229.

[7] M. H. Zhao, Z. L. Wang, and S. X. Mao, *Nano Lett.* **4** (2004) 587-590.

[8] A. N. Morozovska , S. V. Svechnikov, E. A. Eliseev, B. J. Rodriguez, S. Jesse, and S. V. Kalinin, *Phys. Rev. B* **78** (2008) 054101.

[9] Z. L. Wang, *Mater. Sci. Eng. R* **64** (2009) 33-71.

Chapter 6

Dense ZnO thin films as seed layers for growing ZnO nanowires

As stated in Chapter 4, in the last years, many efforts of the scientific research were devoted to the study of ZnO, thanks to the intriguing possibility of synthesizing this material with different morphologies and shapes, both at the micro- and nano- scale. Among them, zinc oxide nanowires (ZnO NWs) have received much more attention, because of their interesting electrical and piezoelectric properties, combined with the presence of nanoconfinement quantum mechanical effects. Moreover, the presence of a high surface area allows to functionalize the nanostructures with different functional agents, for the fabrication of biosensors, gas sensors and protective coatings.

In literature it is reported that growing ZnO NWs requires the presence of proper metal catalysts or crystalline seed layers, for starting and promoting the growth [1, 2]. Concerning metal catalysts, gold nanoparticles (NPs) are widely used and high-quality ZnO NWs can be grown [3]. However, the presence of metal NPs is somehow undesirable because their incorporation in the final NWs generates deep-level traps, which worsen optical and electrical NWs properties [2]. In alternative to this, a thin ZnO layer can be deposited on substrates before growing NWs, in a very simple way and with a large variety of synthesis techniques. The most diffused and promising seems to be the sol-gel and sputtering ones, and a lot of works reported the growth of high-quality ZnO NWs on substrates seeded with these two methods [1].

In the following, all the scientific results will be reported about using sputtered and sol-gel/spin-coated ZnO thin films as seed layers for the growth of ZnO NWs. Sputtered ZnO seed layers were deposited by the RF magnetron sputtering technique, with the system described in Chapter 3, Section 3.3.1. High-quality ZnO NWs were grown by a hydrothermal method on the sputtered and spin-coated seed layers. The morphology and crystallographic orientation of the seed layers and of the resulting NWs were investigated, with the aim of correlating the characteristics of the underlying seed layer to the resulting NWs. In order to investigate a possible influence of the wetting properties of the seed layer on the grown NWs, optical contact angle measurements were also performed, both on ZnO seed layers and NWs. Results showed that is possible to control the wetting behavior of ZnO NWs by properly selecting the kind of seed layer used to promote the growth of the wires. In particular, ZnO NWs grown on spin-coated seed layers showed a highly hydrophilic behavior, while super hydrophobic NWs can be obtained when sputtered seed layers are used for starting the growth.

6.1. Growth conditions of ZnO thin films

Sputtered ZnO seed layers ZnO seed layers were synthesized by the RF magnetron sputtering, and used for promoting the growth of high quality ZnO NWs. Sputtered seed layers were grown both on Si and conductive Si/Ti/Au substrates. Before the deposition processes, substrates were cleaned in an ultrasonic bath of both acetone and ethanol (10 min for each washing cycle) and dried under nitrogen flow. Suitable vacuum conditions with base pressure values ranging from $1.4 \cdot 10^{-7}$ Torr to $5.7 \cdot 10^{-7}$ Torr were obtained with a rotary and a turbo molecular pump. A RF voltage at a working frequency of 13.56 MHz was employed to create the plasma and a fixed power value of 100 W was used for all the deposition processes. ZnO seed layers were grown from both a metallic Zn

target and a ceramic ZnO target, with a target-to-substrate distance of about 8 cm. All the depositions were carried out at room temperature in a mixture of Ar and O_2. In order to prevent any incorporation of contaminants in the films the target was cleaned with a 15-min sputtering process in a pure Ar atmosphere before each deposition. The sputtering growth conditions and thickness of all the samples are summarized in Table 6.1.

Sample	Target	Pressure [mTorr]	Ar flow [sccm]	O_2flow [sccm]	Deposition time [min]	Thickness [nm]
M_1	Zn	5	9	1	60	180
M_2	Zn	5	34	6	60	110
C_1	ZnO	5	39	2	120	260
C_2	ZnO	20	39	2	120	260

Table 6.1. Growth conditions of sputtered ZnO seed layers.

Spin-coated ZnO seed layers Spin-coated ZnO seed layers were deposited on conductive Si/Ti/Au substrates by using solutions of zinc acetate (Sigma, purity 98%) in ethanol with three different concentrations (5, 10 and 20 mM). Spin coating of the solutions on the cleaned substrates was carried out at 1000 rpm for 20 s and 3000 rpm for 30 s. The substrates were then washed for few seconds in ethanol and dried under nitrogen flow. This process was repeated five times. The substrates were then calcined in air at 250°C for 20 minutes (heating rate 5°C/min) to decompose the salt and obtain the full crystallization of the ZnO seed layer. The resulting seed layers consist of ultrathin films of textured ZnO nuclei which can be used to grow high vertically-oriented and crystalline ZnO nanowires [4].

6.2. Synthesis of ZnO nanowires

ZnO NWs were grown by hydrothermal route on sputtered and spin-coated ZnO seed layers. Two different synthesis solutions, labeled A and B, were used for growing the NWs.

Solution A consisted of zinc nitrate hexahydrate (50 mL, 30 mm, purity 98%, Sigma–Aldrich) and hexamethylenetetramine (HMT, 50 mL, 30 mm, purity 98 %, Sigma–Aldrich) in bidistilled water (from a Direct-Q Millipore purification system)[5]. The seeded substrates were placed vertically face to walls into a PP reactor with a Teflon® sample holder. The synthesis occurred under slight magnetic stirring at 75°C for 1 hour. After growth, the samples were washed thoroughly with bi-distilled water to remove any residual impurity from the surface and dried under nitrogen flow.

Solution B was prepared according to [6] and consisted of $Zn(NO_3)_2{\cdot}6H_2O$ (25 mM), HMT (12.5 mM), polyethyleneimine (PEI, average $M_w \approx 800$, 5 mm, Sigma–Aldrich), and ammonium hydroxide (28%, 320 mm, Sigma–Aldrich) in bidistilled water. The final volume of the growth solution was 100 mL. Substrates were located vertically face to walls into a PP reactor with a Teflon sample holder, and the synthesis occurred under slight magnetic stirring at 88°C for 1 hour. After growth, the samples were washed and dried as reported for solution A.

6.3. Structural, morphological and wetting analysis of ZnO seed layers

ZnO sputtered seed layers The list of seed layers obtained by RF magnetron sputtering is reported in Table 6.1 with the corresponding process parameters.

Samples grown from metal (Zn) and ceramic (ZnO) targets are labeled with M and C, respectively. The growth parameters like gas pressures and flows influence the morphology of the final thin films and affect their performance if used as seed layers. This aspect was exploited and several growth conditions were used to obtain seed layers with different surface features, such as surface morphology and roughness. The best growth conditions, suitable for obtaining a seed layer with the appropriate surface characteristics, were selected after having analyzed the quality of the NWs grown on ZnO/Si seed layers. As shown later, the best resulting NWs were those grown on sample C_1, so its growth conditions were selected as the best ones and used to deposit ZnO thin films also on conductive Si/Ti/Au substrates.

The morphology and thickness of the samples were investigated using a Carl-Zeiss Dual Beam Auriga, consisting of a Field Emission Scanning Electron Microscope (FESEM) and Focused Ion Beam (FIB). Additionally the surface morphology and roughness of the sputtered seed layers were evaluated by an Atomic Force Microscope (AFM DME-SPM DualScopeTM Microscope from Danish Micro Engineering) in contact mode using DME DS 95-xxx DC rectangular silicon probe, with pyramidal tip with curvature radius < 10 nm.

FESEM images of the ZnO seed layers grown on Si are reported in Fig. 6.1, whereas AFM topographic images are shown in Fig. 6.2. The surfaces were mainly characterized by densely packed grains, with diameter ranging between about 20 and 40 nm. However, some small differences can be appreciated: the surface of sample M_1 (shown in Figs. 6.1(a) and 6.2(a)) has irregular size and shape grains (some grain diameters exceed the average grain size range with an averaged maximum peak height of 17.4 nm), with a root mean square (RMS) surface roughness of 5.5 nm, as reported in Table 6.2. A rough surface (4.4 nm, see Table 6.2), with great asperities (8.6 nm averaged maximum peak height) also characterizes sample C_2 (Figs. 6.1(d) and 6.2(d)). As far as samples M_2 and C_1 are concerned, the surface is more homogeneous and smooth (2.3 and 1.9 nm in roughness, respectively, see also Figs. 6.2(b) and 6.2(c)). The more pronounced surface roughness of sample M_1 is also clearly visible from Fig. 6.2(a), where the presence of big ZnO grains on the sample surface is represented by the bright spots. This aspect is in accordance with FESEM analysis of the same sample, and reported in Fig. 6.1(a). The presence of a columnar and oriented ZnO structure is evident for all the samples from cross-section images, reported in the insets of Figs. 6.1(a) – 6.1(d).

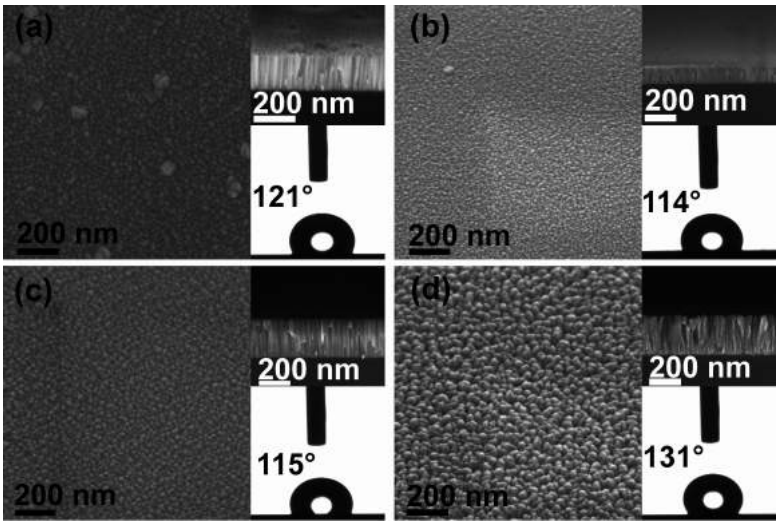

Figure 6.1. FESEM images of (a) M_1, (b) M_2, (c) C_1 and (d) C_2 ZnO aged sputtered seed layers deposited on Si. The top-right insets show the cross-section images of the seed layers, and the bottom-right insets show the water contact angles.

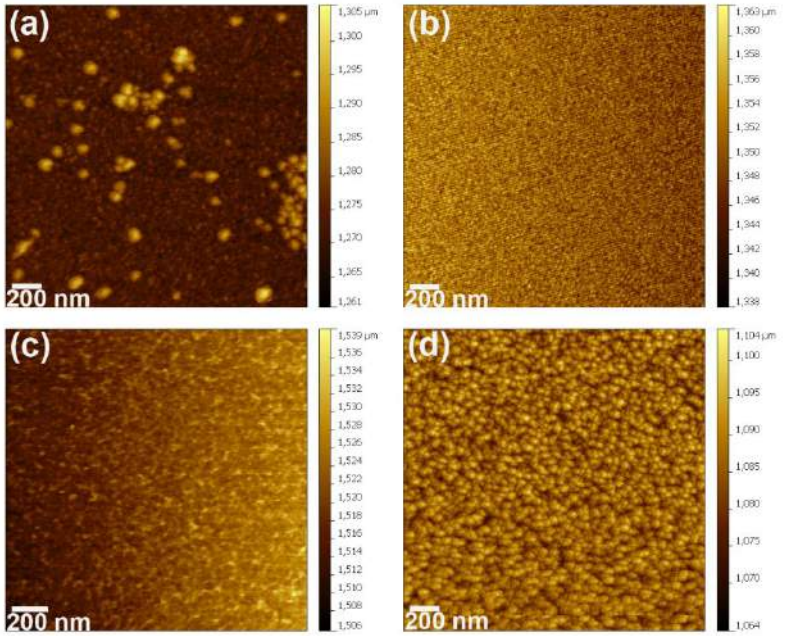

Figure 6.2. Atomic Force Microscope topographic images of ZnO sputtered seed layers: (a) M_1; (b) M_2; (c) C_1; (d) C_2 samples.

Sample	RMS Surface roughness [nm]	WCA [°]	Surface free energy [mN/m]
M_1	5.5	121	37.7
M_2	2.3	114	39.0
C_1	1.9	115	45.0
C_2	4.4	131	37.1

Table 6.2. Surface roughness and wettability properties of two-week aged sputtered ZnO seed layers.

The wettability and surface free energy of ZnO seed layers and NWs were evaluated by optical contact angle (OCA) measurements with the sessile drop technique, using an OCAH 200 (DataPhysic Instruments GmbH). A liquid drop with a volume of 1.5 µl was dispensed and the image of the drop on the sample was acquired with the integrated camera. The drop profile was extracted and fitted with a dedicated software returning the contact angle value at the liquid – solid interface. When required (e.g., in the case of non symmetric drops) the tangent leaning method was applied. To compute the surface free energy, the Owens-Wendt method was applied [7]. In this case the use of two different liquid probes was required, in order to get the polar and dispersive components of the total surface free energy. Water and diiodomethane were used in this case. For each sample and liquid, three drops were dispensed at three different positions on the surface of the sample and the average value was obtained from the software. In order to evaluate the aging effects on the wettability properties, the samples were stored in ambient conditions for two weeks.

In the case of sputtered ZnO seed layers, the evolution of the wetting behavior of seed layer C_1 with time was analyzed. The fresh sputtered sample exhibited a typical hydrophilic behavior with a water contact angle (WCA) of 38° and a surface free energy (SFE) of 62.9 mN/m. Two weeks later, the

surface turned into hydrophobic, with a higher WCA (115°) and a lower SFE (45.0 mN/m). Therefore a transition from a hydrophilic (WCA lower than 90°) to hydrophobic (WCA greater than 90°) behavior was obtained by aging the sputtered seed layers. This change in the wettability behavior of the surface is clearly visible in Fig. 6.3. The initial hydrophilic behavior can be explained with the action of the plasma created in a mixture of Ar/O_2 during the deposition process, which activates the surface and promotes its hydroxylation.

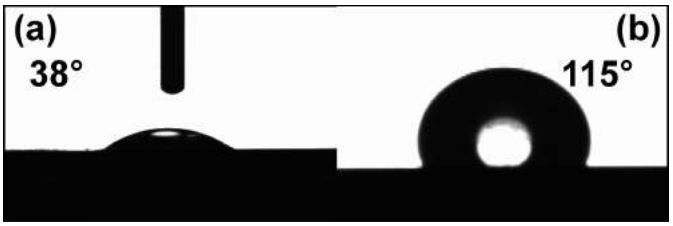

Figure 6.3. Water contact angle on ZnO sputtered seed layers C_1 deposited on Si (a) just after the deposition process and (b) two weeks later.

Sample	**Fresh seed layers**		
	SFE [mN/m]	Polar component [mN/m]	Dispersive component [mN/m]
C_1	62.9	34.5	28.4
SC_5	61.2	30.7	30.5
SC_10	63.4	31.5	31.9
SC_20	63.9	29.6	34.3
NWs/C_1	90.1	27.0	63.1
NWs/SC_5	n.a.	n.a.	n.a.
NWs/SC_10	n.a.	n.a.	n.a.
NWs/SC_20	69.6	35.0	34.6
Sample	**Two week aged seed layers**		
	SFE [mN/m]	Polar component [mN/m]	Dispersive component [mN/m]
C_1	45.0	1.8	43.2
SC_5	39.6	0.4	39.2
SC_10	39.0	0.1	38.9
SC_20	40.6	7.4	33.2
NWs/C_1	95.6	28.6	67.0
NWs/SC_5	61.7	23.8	37.9
NWs/SC_10	66.0	29.1	36.9
NWs/SC_20	66.3	29.4	36.9

Table 6.3. Total surface free energy (SFE) and its component for fresh and aged ZnO seed layers and of NWs grown on fresh and aged seed layers.

The formation of OH groups causes an increase of the hydrophilicity and of the SFE (Table 6.3). A surface rich of hydroxyl groups is energetically unstable, whereas oxygen adsorption is thermodynamically favored [8]. Thus, the hydroxyl groups adsorbed on the surface of the seed layer are gradually replaced by oxygen atoms. The transition to hydrophobicity is then achieved by simply aging the samples in ambient air. After two weeks of aging, no further changes in the WCA were observed. By considering the whole set of sputtered seed layers, a relationship between the WCA (in Table 6.2 for the aged seeds) and

the surface morphology can also be pointed out. An increase of the contact angle is noticed when the surface roughness is higher, as can be observed by correlating FESEM and AFM images with the water contact angles in Figs. 6.1(c) and 6.1(d).

ZnO spin-coated seed layers Seed layers were also prepared by sol-gel approach, thus by spin coating a solution of zinc acetate in ethanol with three different concentrations (5, 10 and 20 mM) on a Si/Ti/Au wafer and decomposing the salt at 250°C. The resulting seed layers consist of ultrathin films of textured ZnO nuclei which can be used to grow high vertically-oriented and crystalline ZnO nanowires [4]. Similarly to the sputtered seed layers, the spin coated ones (hereafter called SC_5 from the 5 mM solution, SC_10 from the 10 mM and SC_20 from the 20 mM one) were immediately characterized and used for the nanowires growth, or aged for two weeks in ambient condition, prior to further analysis and NWs synthesis. FESEM imaging cannot be carried out on these ultrathin seed layers, whereas X-ray diffraction pattern were acquired using a Panalytical X'Pert MRD PRO diffractometer, in parallel beam configuration. A Cu K_α monochromatic radiation was used as X-ray source, with a characteristic wavelength $\lambda = 1.54059$ Å. XRD measurements show the presence of (002) reflection, indicating their c-axis orientation (see Fig. 6.4).

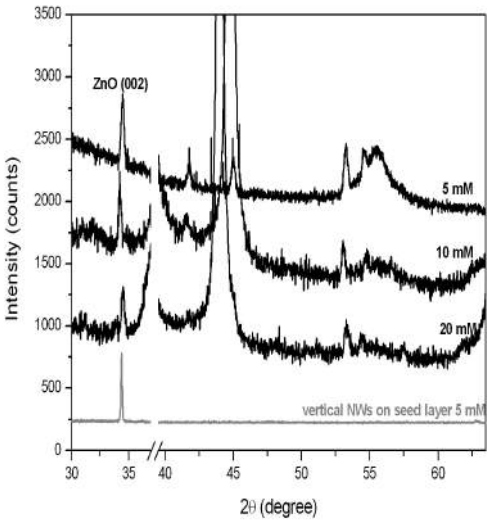

Figure 6.4. X-ray diffraction patterns of the spin-coated seed layers at different concentrations, i.e. 5, 10 and 20 mM of the starting solution of zinc acetate in ethanol. For comparison, the pattern of the ZnO NWs grown on the 5 mM seed layer is also reported.

The wettability behavior of fresh and two weeks aged ZnO spin coated seed layers was analyzed by OCA measurements. As in the case of the sputtered layers, the fresh SC samples exhibited a hydrophilic behavior, with WCA average values lower than 90° in all cases (Table 6.4). OCA measurements were repeated two weeks after the synthesis process. A WCA greater than 90° was observed for samples SC_5 and SC_10, indicating a transition from a hydrophilic to hydrophobic behavior, although not so pronounced as in the case of the sputtered seed layers. A WCA lower than 90° was observed for the fresh SC_20 sample and a hydrophilic behavior was still present two weeks after the deposition process. The surface wettability evolution from fresh to two weeks aged SC_5 and SC_20 samples is also shown in Fig. 6.5.

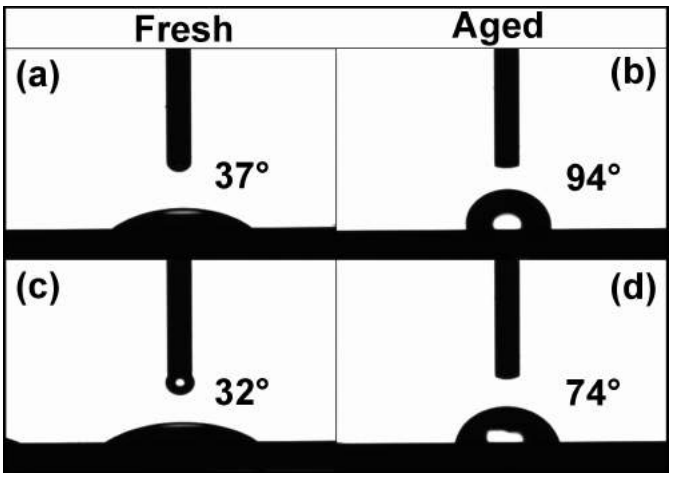

Figure 6.5. WCA on (a) 5 mM fresh, (b) 5 mM two-week aged, (c) 20 mM fresh, and (d) 20 mM two-week aged spin-coated seed layers deposited on Si/Ti/Au substrates.

Sample	Fresh seed layers WCA [°]	Two-week aged seed layers WCA [°]
C_1	38	115
SC_5	37	94
SC_10	34	98
SC_20	32	74

Table 6.4. WCA values of fresh and two-week aged ZnO seed layers on conductive (Si/Ti/Au) substrates.

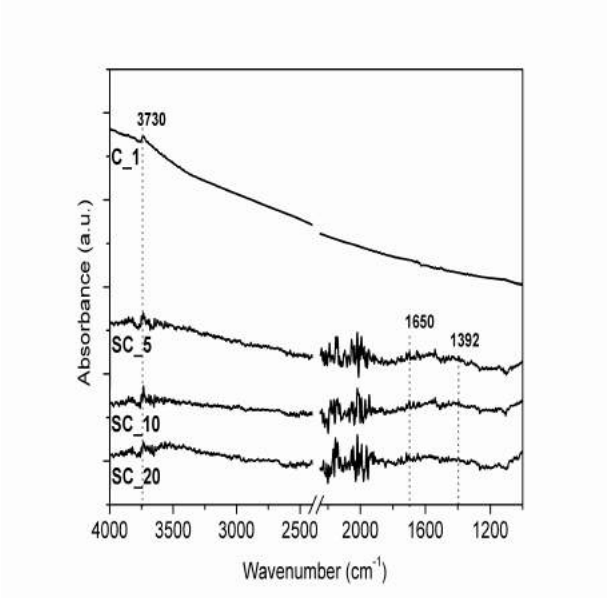

Figure 6.6. Infrared spectra of the seed layers prepared by sputtering (C_1) and by spin-coating from the solutions 5 mM (SC_5), 10 mM (SC_10) and 20 mM (SC_20).

In all cases the SFE diminishes with the aging time (Table 6.3). This time dependence can be explained as in the case of the sputtered seed layers, where the hydroxyl groups are replaced with time to more thermodynamically stable oxygen sites, non-polar, thus increasing the surface hydrophobicity [8]. This substitution can be also driven by the continuous condensation of the ≡Zn-OH species into ≡Zn-O-Zn≡ ones with time, as generally observed during aging processes of sol-gel chemistry [9].

Thus, the aging phase promotes the complete condensation of ZnO network, increasing its connectivity and leading to less defective and less polar seed layer films. It can be also noticed an influence of the precursor solution concentrations on the hydroxyl groups content in the films. Based on the sol-gel theory, it can be assumed that a high amount of ≡Zn-OH species are present in the seed layer obtained from precursor solutions with high concentration, thus leading to a longer condensation process in time. The presence of a slightly higher number of hydroxyl groups on the aged SC_20 sample is indeed visible from IR spectra (Fig. 6.6), with respect to both SC_5 and SC_10 layers and to the sputtered seed layer C_1, where an almost hydroxyl-free surface is observed. This result is confirmed by the WCA value for aged SC_20 layer, which is significantly lower than that of the other two SC samples.

6.4. Characterization of ZnO nanowires grown on ZnO seed layers

ZnO NWs grown on sputtered ZnO seed layers As a preliminary test on the quality of the sputtered seed layers in leading highly oriented nanowires, the solution A, consisting of only $Zn(NO_3)$ and hexamethylene tetrammine (HMT), was used for growing NWs on the two weeks aged sputtered seed layers.

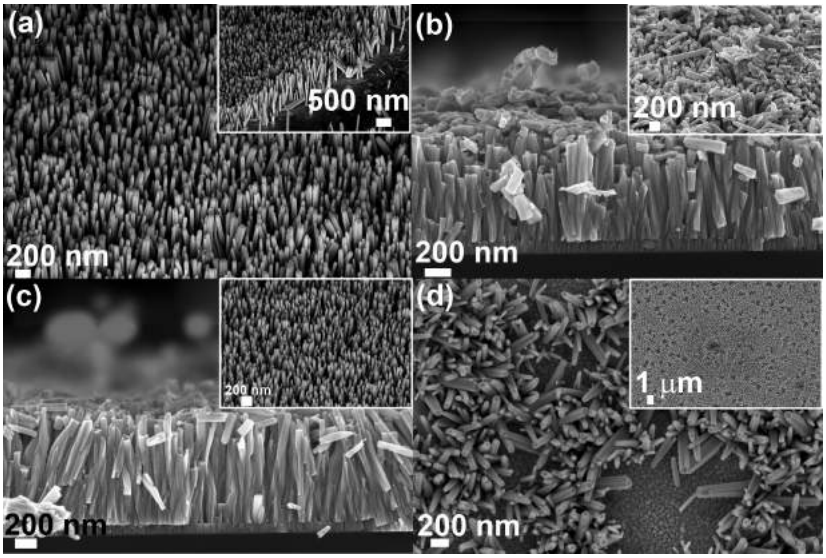

Figure 6.7. FESEM images of the ZnO NWs (top and cross-section views) grown with solution A on ZnO sputtered seed layers deposited on Si: (a) M_1, (b) M_2, (c) C_1 and (d) C_2.

FESEM images of ZnO NWs grown with solution A on ZnO/Si sputtered seed layers aged two weeks (layers M_1, M_2, C_1 and C_2) are reported in Fig. 6.7. The morphology of the NWs can be ascribed to the morphology of each seed layer. ZnO NWs grown on seed layer M_1 did not cover the whole surface, and this may be due to the large grains present on the surface of the

film, as can be observed in Fig. 6.1(a). The low quality but dense NWs grown on sample M_2 may be attributed to the small size of its closely-packed grains. Sample C_2 (showing a high roughness as clearly visible from images reported in Fig. 6.1(d) and confirmed by the higher WCA values) contributed to the growth of short, non-uniform and not well-aligned NWs. In contrast, vertically oriented and highly dense ZnO NWs covering the whole seed layer surface were obtained only on seed layer C_1.

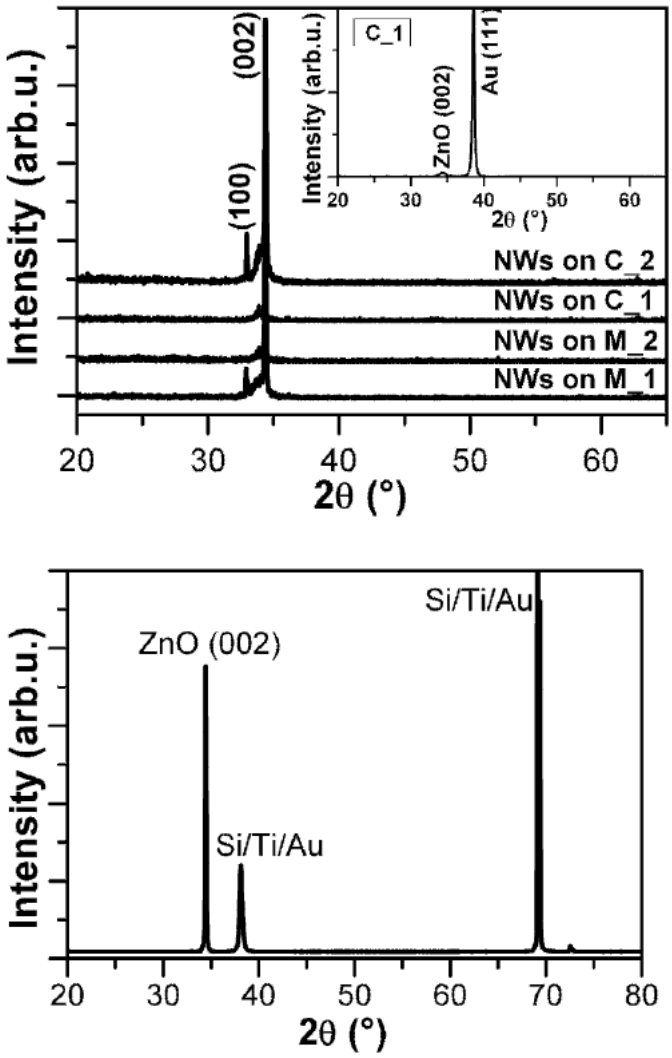

Figure 6.8. (TOP) X-ray diffraction patterns of the ZnO NWs grown on the sputtered seed layers (M_1, M_2, C_1 and C_2) using the synthesis solution A. The inset reports the XRD diffraction pattern of seed layer C_1 (BOTTOM) XRD pattern of the ZnO NWs grown with the high growth rate solution B on the aged sputtered seed layer C_1.

ZnO NWs crystal structure was evaluated using a Panalytical X'Pert X-ray diffractometer in the Bragg-Brentano configuration. A Cu K_α monochromatic radiation was used as X-ray source, with a characteristic wavelength $\lambda = 1.54059$ Å. XRD characterization shows the wurtzite structure of the nanowires, with the predominance of the (002) reflection (top panel of Fig. 6.8). On the basis of the preliminary results discussed above, the growth conditions of seed layer C_1 were selected for the synthesis of other seed layers on conductive substrates

(Si/Ti/Au). The XRD pattern acquired on sample C_1 is reported in the inset of the top panel in Fig. 6.8. The newly sputtered seed layers C_1 were used fresh or aged for growing the ZnO NWs using solution B. This solution combines the use of $Zn(NO_3)$ and HMT with polyethyleneimine (PEI) and ammonium hydroxide (NH_4OH). Indeed PEI acts as a capping agent, adsorbing onto the side surfaces of the ZnO nanowires, and thus enhancing the vertical growth [10]. In addition both PEI and NH_4OH are reported to suppress the homogeneous nucleation process in the growth solution, thus avoiding contamination from other ZnO structures, while allowing the ZnO nanowires growth on the seeded substrate at a high growth rate and high aspect ratio (length to diameter, L/D)[6].

FESEM images of the nanowires grown on both fresh and aged seed layers using conductive substrates (reported in Figs. 6.9(a) and 6.9(b), respectively) show that the NWs grown in these conditions are longer, denser and more vertically-oriented than those synthesized with the solution A. In particular the best results in terms of vertical alignment and morphology are obtained for the NWs grown on the aged seed layer (Fig. 6.9(b)), whereas the aspect ratio of the NWs on fresh seed layer is quite higher (L/D=28) than those on the aged one (L/D=12).

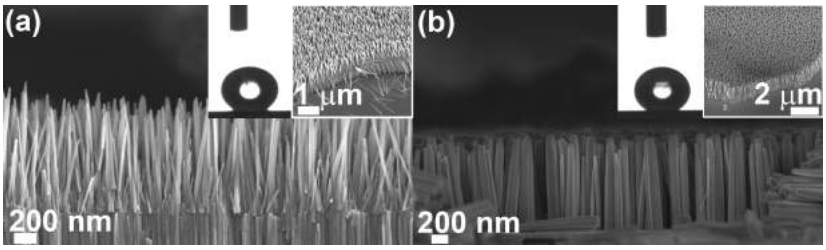

Figure 6.9. FESEM images of the ZnO NWs grown with solution B on seed layer C_1 deposited on Si/Ti/Au (a) freshly sputtered and (b) aged for two weeks in ambient conditions. The insets show the top view of the NW array.

Sample	**Fresh seed layers**			
	Length	Diameter	Aspect ratio	WCA
	[μm]	[nm]	[L/D]	[°]
NWs on C_1	1.1	40	28	179
NWs on SC_5	1.0	70	15	63
NWs on SC_10	1.1	50	22	45
NWs on SC_20	1.2	40	30	24
Sample	**Two-week aged seed layers**			
	Length	Diameter	Aspect ratio	WCA
	[μm]	[nm]	[L/D]	[°]
NWs on C_1	1.5	125	12	179
NWs on SC_5	1.2	80	15	42
NWs on SC_10	1.3	110	12	33
NWs on SC_20	1.7	90	19	33

Table 6.5. Morphological features and WCA values of the ZnO NWs (solution B) grown on both fresh and two-week aged seed layers deposited on conductive (Si/Ti/Au) substrates prepared by sputtering and spin-coating methods.

The XRD pattern of NWs grown on seed layer C_1 using solution B is reported in the bottom panel of Fig. 6.8. It should also be added that the

homogenous array of nanowires covers a quite broad surface area, typically in the order of cm^2-size, of the wafer substrate. OCA measurements were carried out to study the NWs wettability behavior. The results were also compared with those of ZnO sputtered seed layer C_1 in order to establish a possible relationship between the wetting behavior of the starting seed layers and the grown NWs. In spite of the wettability properties of the starting seed layer (hydrophilic when fresh, hydrophobic after two weeks from the synthesis), a superhydrophobic behavior was revealed in both the NW arrays, with WCA values of almost 180° (Table 6.5). Surfaces are indeed defined super-hydrophobic when the WCA is larger than 150°.

ZnO NWs grown on spin-coated ZnO seed layers ZnO NWs were grown on ZnO SC seed layers, using both the solution A (Fig. 6.10) and the high growth rate synthesis solution B (Fig. 6.11). In this last case, both fresh and aged SC seed layers are used, obtaining an increase of the NWs density by increasing the solution concentration used for the seed layer preparation. The highest density was indeed observed for the NWs grown on sample SC_20, both in the case of fresh and aged substrates. It is then assumed that seed layers prepared from high concentrated solutions results in highly packed crystalline grains of ZnO, leading to a dense array of nanowires. In all sample cases, high quality ZnO NWs with good vertical alignment and high aspect ratio were observed, covering broad areas of the substrate. All the nanowires presented pointed tips. However, the NWs grown on the aged seed layers are longer and larger, with lower aspect ratio, than those grown on the fresh SC seed layer (see Table 6.5).

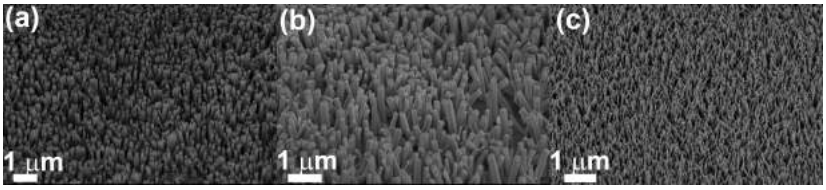

Figure 6.10. FESEM images of ZnO NWs (solution A) grown on fresh spin coated seed layers with the concentration of (a) 5 mM, (b) 10 mM, and (c) 20 mM.

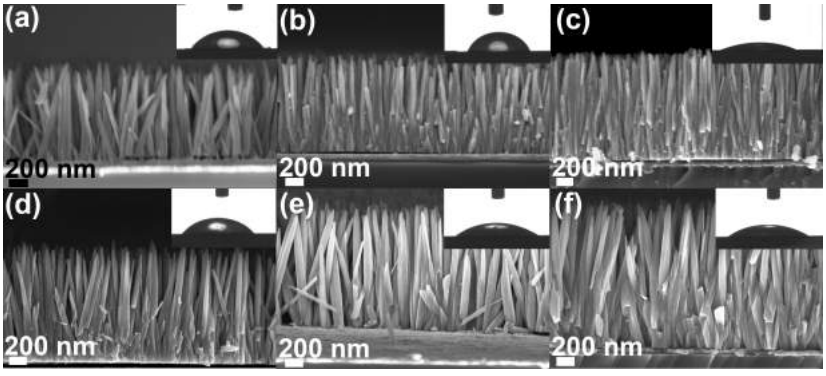

Figure 6.11. FESEM images of ZnO NWs (solution B) grown on fresh spin-coated seed layers (Si/Ti/Au substrates) with concentrations of (a) 5 mM, (b) 10 mM, and (c) 20 mM and on seed layers aged for two weeks at room temperature in ambient conditions with the same concentrations: (d) 5 mM, (e) 10 mM, and (f) 20 mM.

XRD results are reported in the top panel of Fig. 6.12. Notably, all the NW arrays are hydrophilic, as demonstrated by their WCAs (Table 6.5) and

IR spectra. Indeed, it is noted from IR spectroscopy (Fig. 6.12, bottom panel) that the surface of the NWs grown on SC seed layers is rich of hydroxyl groups. In particular, the signal of isolated surface hydroxyl groups are observed at 3730 cm^{-1}. The broad band in the range 3600-3100 cm^{-1} is attributed to OH stretching of the water of crystallization in the solid state, and that at 1600 cm^{-1} is attributed to OH deformation.

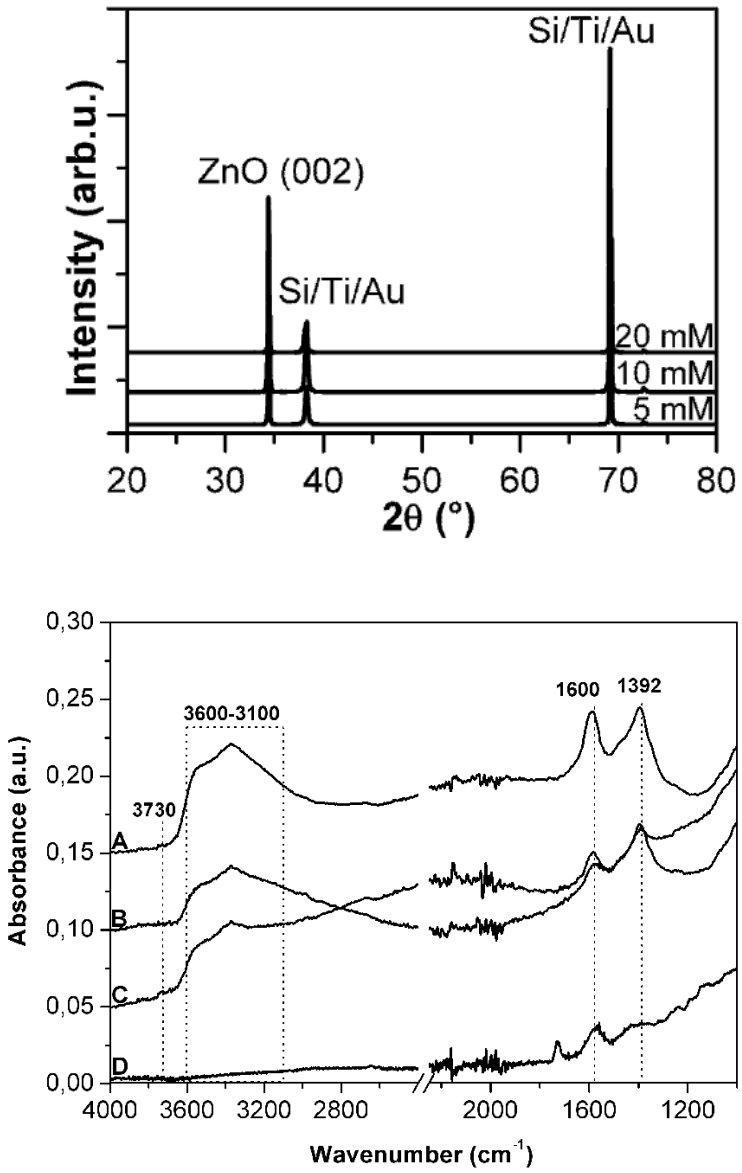

Figure 6.12. (TOP) X-ray diffraction patterns of the ZnO NWs grown on the spin coated seed layers at different concentrations, i.e. 5, 10 and 20 mM (BOTTOM) Attenuated total reflectance (ATR) IR spectra of the ZnO NWs grown on fresh seed layers. Trace A: NWs on fresh seed SC_5, trace B: NWs on fresh seed SC_10, trace C: NWs on fresh seed SC_20, trace D: NWs on fresh sputtered seed C_1.

6.5. Comparison between ZnO NWs grown on sputtered and spin-coated seed layers

Since the nanowires growing synthesis was the same for both kinds of seed layers, i.e., sputtered or spin coated, the morphology and wettability behavior of the obtained nanowires on the different seed layers can be compared, as summarized in Table 6.5. In general, whereas similar NWs lengths or diameters can be achieved starting from both kinds of seed layers, it is first noted that the aging of the seed layer, whatever sputtered or spin coated, produces longer and thicker ZnO nanowires. These features are attributed to the highly-condensed ZnO seed layer due to the aging effect, as previously explained. Indeed oxygen-rich and less defective surfaces (as evidenced by the high contact angle) can be obtained upon aging, thus leading to highly condensed ZnO crystalline grains, possibly larger than the fresh ones. These features should induce a higher growth rate of the nanowires, resulting in longer and thicker nanostructures. Concerning the wettability properties, the NWs grown on the sputtered seed layer C_1, either fresh or aged, show a superhydrophobic behavior (WCA about 180°). In contrast, the NWs on spin coated seed layers (from SC_5 to SC_20) are quite hydrophilic (averaged WCA about 40°). This behavior is confirmed by infrared spectroscopy (Fig. 6.12), evidencing, as previously explained, a hydroxyl-rich surface of the NWs from SC layers. In contrast, the NWs grown on the sputtered seed layer C_1 evidence a lower amount of OH groups, thus confirming their superhydrophobic behavior. An evident relationship was found between the kind of seed layer used and the wetting behavior of the ZnO NWs. Although most of studies on the growth of nanowires report on a hydrophobic behavior for as-grown ZnO nanowires [10], hydrophilic surfaces are obtained when NWs were grown onto spin-coated ZnO films. In order to explain such phenomenon some evidences from the literature can be recalled. The mechanism of photoinduced hydrophilicity in ZnO NWs is well known [8]. Briefly, the formation of electron-hole couples generates oxygen vacancies due to the reaction between photogenerated holes and the lattice oxygen. The presence of vacancies favors the adsorption of hydroxyl groups. Thus, material surfaces characterized by high defect density tend to react with more OH groups [10]. Usually, hydrothermal techniques (here used for all the synthesis of ZnO NWs) do not allow for a perfect control of the impurities and defects in the final nanostructure. Therefore NWs synthesized by this technique can have a density of lattice defects not entirely negligible, especially those grown onto spin-coated layers. In addition, the surface exhibited from the ultra-thin spin-coated films is expected to be less homogeneous and more defective with respect to the 100-nm-thick sputtered seed layer. Thus spin-coated seed layers may promote the growth of ZnO NWs with higher density of defects than the sputtered films. This defective structure is indeed confirmed by the NWs morphology from FESEM characterization. NWs with homogeneous diameter from the bottom to the top are obtained on the sputtered seed layer C_1 (Fig. 6.9). In contrast, all the NWs grown on the sol-gel seed layers present a sharpening of the tips, with a reduction of the diameter from the bottom to the top of the wire (Fig. 6.11). This size reduction is indicative of the presence of defects and vacancies in the lattice planes, which usually corresponds to a higher concentration of OH groups, as evidenced by IR measurements (Fig. 6.12). Concerning a possible correlation between the wetting behavior of the NWs grown on fresh and aged seed layers, any change is observed in the wetting behavior, with time. Even if some small variations in the WCA were observed among the NWs grown on fresh and aged seed layers, the overall wetting behavior of the wires do not change significantly. Moreover, no significant differences in the wetting behavior of the nanowires themselves is observed upon their aging time: both as synthesized and long time aged ZnO nanonowires maintain their wetting behavior, either highly hydrophilic when grown on spin-coated seed layers, either superhydrophobic, when on sputtered seeds. This stability is highly desired in view of an application in operating devices.

6.6. Conclusions

Zinc oxide seed layers were synthesized by the spin coating and the RF magnetron sputtering techniques and used for promoting the growth of well-aligned ZnO nanowires via a hydrothermal method, using two different growth solutions. The influence of the seed layer characteristics, deriving from the different synthesis conditions, on the final morphology and wettability properties of the ZnO NWs was analyzed. A time-dependent behavior of the wetting properties was found for both sputtered and spin coated seed layers. In particular, a marked transition from a hydrophilic to hydrophobic state, associated to a change of the surface free energy of the films, was obtained for sputtered seed layers. In the case of spin-coated films this transition towards higher contact angles was still present but less pronounced and dependent on the precursor concentration. The surface of the aged spin coated seed layer synthesized from a higher precursor concentration was still hydrophilic after two weeks from its deposition. A strong relationship between the kind of seed layer, i.e., sputtered or spin-coated, and the final NWs morphology, surface chemistry and thus wettability was noticed. In particular NWs grown on sputtered seed layers show a columnar morphology, high aspect ratio and a superhydrophobic behavior, with contact angles of around 180°. In contrast, on spin coated seed layers, highly hydrophilic NWs with hydroxyl-rich surfaces, conical-shape morphology and high aspect ratio were obtained. In addition, densely packed ZnO nanowires can be obtained by increasing the concentration of the starting seed layer by spin-coating. It can be also noted in general that fresh seed layers (both sputtered and spin coated) lead to thinner but shorter nanowires, whereas NWs on aged seed layers are longer and thicker. It is therefore demonstrated that ZnO nanowire arrays with tunable density, aspect ratio and wetting properties can be easily produced on broad surface areas (typically cm^2-sized). Depending on their surface chemistry and wetting behavior, superhydrophobic nanowires, ideal for self-cleaning, anti-fogging or microfluidic devices can be obtained. In contrast the hydroxyl-rich and hydrophilic surface makes the ZnO nanowires ideal candidate for further surface functionalization with enhanced adsorption properties towards biological agents or dye for imaging, diagnostic, optical or photovoltaic applications.

Bibliography

[1] M. Laurenti, V. Cauda, R. Gazia, M. Fontana, V. F. Rivéra, S. Bianco, and G. Canavese, *Eur. J. Inorg. Chem.* **2013** (2013) 2520-2527.

[2] M. Laurenti, A. Verna, M. Fontana, M. Quaglio, and S. Porro, *Appl. Phys. A* **117** (2014) 901-907.

[3] S. -W. Kim, S. Fujita, and S. Fujita, *Appl. Phys. Lett.* **86** (2005) 153119.

[4] L. E. Greene, M. Law, D. H. Tan, M. Montano, J. Goldberger, G. Somorjai, and P. Yang, *Nano Lett.* **5** (2005) 1231-1236.

[5] L. Vayssieres, *Adv. Mater.* **15** (2003) 464-466.

[6] C. Xu, P. Shin, L. Cao, and D. Gao, *J. Phys. Chem. C* **114** (2010) 125-129.

[7] K. Grundke, *Handbook of Applied Surface and Colloid Chemistry* (2001) Krister Holmberg, John Wiley & Sons, Ltd, p. 120.

[8] E. L. Papadopoulou, M. Barberoglou, V. Zorba, A. Manousaki, A. Pagkozidis, E. Stratakis, and C. Fotakis, *J. Phys. Chem. C* **113** (2009) 2891-2895.

[9] C. J. Brinker, and G. W. Scherer, *Sol-Gel Science* (1990) Academic Press, San Diego.

[10] S. Xu, and Z. L. Wang, *Nano Res.* **4** (2011) 1013-1098.

Chapter 7

Deposition and characterization of sponge-like ZnO thin films

The aim of this Chapter is to present and describe the two-step growth method used for obtaining ZnO thin films with the so-called sponge-like nanostructure. The final aim was first to investigate if also porous nanostructured ZnO film could be characterized by the presence of piezoelectric properties to be further exploited in the fabrication of piezoelectric-based devices. Moreover, the presence of a nanoporous structure suggested a way for doping ZnO with a simple method, properly described in Chapter 8.

In the first step of the synthesis process, metallic zinc (Zn) films were grown on different kind of substrates by the RF magnetron sputtering technique, with the system described in Chapter 3, Section 3.3.1. Different deposition conditions, like the RF power and the gas pressure, were properly changed and the set of the optimal deposition parameters was selected according to the characterization results, in order to get Zn films with the desired properties. After the sputter deposition, the oxidation of Zn layers was performed with two different methods, described in the next part. The first one, namely the thermal oxidation method, was performed at high temperatures in ambient air, while the second one, which is called water-vapor oxidation method, was a low-temperature process, and can be considered a simple and efficient method for the oxidation of Zn films when high temperature processes should be avoided. This is, for example, important in case when flexible substrates are needed, where polymer materials, which cannot support high-temperature treatments, are widely used as substrates.

7.1. Growth conditions

The set of all the deposition parameters used for growing Zn films by the RF magnetron sputtering technique is summarized in Table 7.1. A 4" diameter Zn target (GoodFellow, purity 99.99%) was used as the source material. All the depositions were performed at a fixed target-to-substrate distance of around 8 cm, in a pure Ar atmosphere. Depositions were carried out in different conditions: in particular the influence of the RF power and of the gas pressure on the properties of the resulting samples was considered. Each film was deposited at room temperature, i.e., no intentional heating was provided to the substrates, with a fixed Ar flow of 10 sccm. Before each deposition process, suitable base pressures ranging between $2.7 \cdot 10^{-7}$ Torr and $3.6 \cdot 10^{-7}$ Torr were obtained by a two-stage pumping system.

Sample	RF power	Pressure	Deposition time	Average thickness
	[W]	[mTorr]	[min]	[μm]
Zn_30	30	5	60	3.7
Zn_50	50	5	60	4.0
Zn_50_10	50	10	60	4.5
Zn_100	100	5	120	16.9

Table 7.1. Deposition conditions and average thicknesses of sponge-like Zn films deposited on Si substrates.

Thermal oxidation method After the sputter deposition, the metallic Zn films were placed in a muffle and treated at 380°C for 120 min in ambient air, in order to oxidize the Zn layer and to obtain the conversion of the Zn film into ZnO nanostructured layers.

Water-vapor oxidation method The sputtered Zn layers were fixed into a clamping system and exposed for 120 min to the water vapor deriving from De-Ionized (DI)-water (18 $M\Omega \cdot cm^{-1}$ at 25°C) heated at 90°C by an hot plate. The temperature of the substrate was monitored by a Pt100 thermocouple.

7.2. Analysis of sponge-like Zn and thermally oxidized ZnO thin films

The aim of this section is to present all the scientific results obtained from the characterization of sponge-like Zn films and of sponge-like ZnO films obtained with the thermal oxidation method. Samples deposited with different deposition parameters are compared in terms of their morphology and crystal structure. On the basis of FESEM and XRD characterization results, the best deposition conditions are selected in order to get the desired sponge-like nanostructure in both Zn and ZnO films. A further insight into the properties of sponge-like ZnO films is obtained from the XPS characterization of the chemical composition, and from the evaluation of the piezoelectric behavior.

7.2.1. Morphology and structural analysis

The set of the deposition parameters used for growing metallic Zn films on Si substrates is reported in Table 7.1. The effects of using different process conditions on the characteristics of the resulting Zn films was first investigated by means of FESEM and XRD measurements. In particular, the change in the morphology and in the crystal structure of the as-grown Zn films was considered, and the set of the optimal deposition parameters was selected, according to the characterization results. The morphology and thickness of sponge-like Zn and ZnO samples were investigated using a Carl-Zeiss Dual Beam Auriga, consisting of a Field Emission Scanning Electron Microscope (FESEM) and Focused Ion Beam (FIB). The crystal structure and orientation of the sponge-like samples were analyzed by X-Ray Diffraction (XRD) measurements using a Panalytical X'Pert X-ray diffractometer in the Bragg-Brentano configuration. A Cu K_α monochromatic radiation was used as X-ray source, with a characteristic wavelength $\lambda = 1.54059$ Å. FESEM analyses were performed also after the thermal treatment carried out to get the conversion of the metallic Zn layers into ZnO films, in order to check that the sponge-like morphology of the starting material was still present after the thermal treatment.

Figs. 7.1 and 7.2 reports the FESEM top-view images acquired on the surface of Zn films grown at different RF power and pressure values, while the FESEM cross-sectional images are shown in Fig. 7.3. As it can be seen, the difference in the deposition conditions affected the final structure of the metallic Zn layer. Figs. 7.1(a), 7.1(b) and 7.1(d) refers to the samples Zn_100, Zn_50 and Zn_30, deposited with the same gas pressure and flow values, but using a different RF power for each case (100 W, 50 W and 30 W, respectively). A strong change in the morphology was clearly visible when sample Zn_100 was compared to the others. When the highest RF power was used for the deposition (100 W), the resulting sample Zn_100 was characterized by a compact structure together with a very pronounced surface roughness. No porous structure was observed in this case, and the surface was mainly characterized by the presence of large and irregular micrometer-sized grains, which can be clearly seen in Fig. 7.2(a). Figs. 7.1(b) and 7.1(d) refer to samples Zn_50 and Zn_30, grown with a lower RF power of 50 W and 30 W, respectively. When the RF power was decreased up to these levels, a net transition of the Zn morphology from the

compact structure of sample Zn_100 to a porous one was observed. Even if both Zn_50 and Zn_30 samples gave evidence of nanostructures characterized by a similar sponge-like morphology, some small differences were appreciated. The presence of pores in sample Zn_50 was still limited. Big crystals agglomerated to each others were visible in this case, limiting the formation of voids between them and the pore dimensions. Fig. 7.1(d) refers to sample Zn_30, which was grown with the lowest RF power (30 W). The decrease in the energy of the sputtered atoms, related to the lower RF power used in this case, promoted the growth of a Zn film with a high degree of porosity, and helped in growing branched-like nanostructures with voids (see Fig. 7.2(d)). The presence of such a nanostructure favoured the formation of nanopores which were not visible in samples Zn_50 and Zn_100.

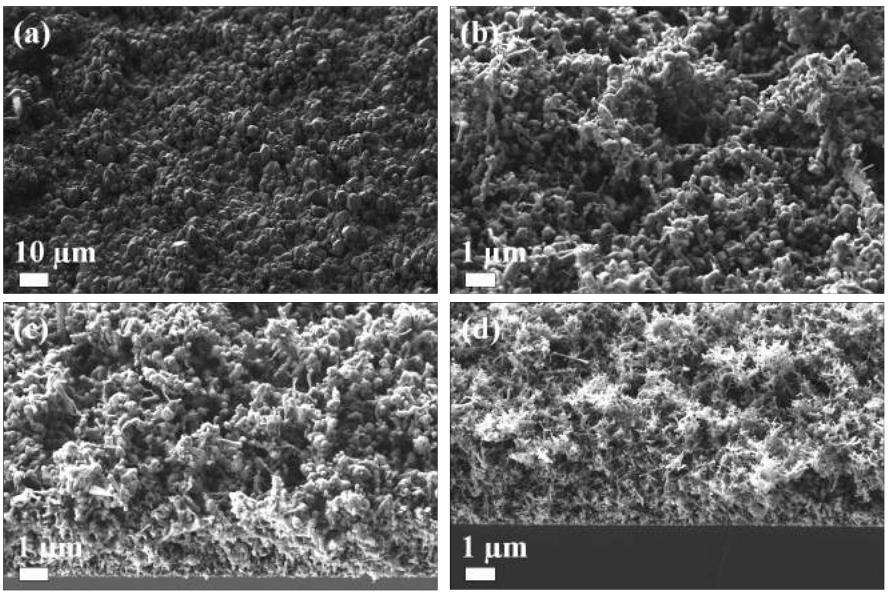

Figure 7.1. FESEM top-view images of Zn films deposited on Si substrates in different conditions: (a) 100 W, 5 mTorr; (b) 50 W, 5 mTorr; (c) 50 W, 10 mTorr; (d) 30 W, 5 mTorr.

In order to study a possible effect of the gas pressure on the Zn morphology, a comparison of two samples grown at a different gas pressure (5 mTorr and 10 mTorr), but with the same RF power (50 W) and for a fixed deposition time (60 min) was also carried out, but from the morphological characterization reported in Figs. 7.1(b) and 7.1(c) no substantial changes were observed between the two samples.

The existence and formation of such a particular kind of sponge-like nanostructure in Zn films can be explained with the model proposed by Jankowski and Hayes [1], which can be considered as an integration to the Thornton's "structure zone" model [2]. This last is, in turn, an extension of the model proposed by Movchan and Demchinshin [2]. This model predicts the existence of three structural zones as a function of the ratio T/T_m, where T is the substrate temperature and T_m is the coating-material melting point. Zone 1 consists of tapered crystals separated by voided boundaries. Zone 2 consists of columnar grains separated by distinct and dense intercrystalline boundaries. Zone 3 is composed of equiaxed grains with a bright surface. Thornton introduced a transition region, the so-called Zone T, standing between Zone 1 and Zone 2, characterized by a more fibrous morphology. An additional zone corresponding to the so-called stable "sponge-like" morphology, and positioned between Zone T and Zone 2, was then introduced by Jankowski and Hayes. This zone can be

obtained at a substrate temperature lying in a range centered at $T/T_m \approx 0.5$, where surface diffusion still dominates but the onset of faceting that plays the dominant role in Zone 2 occurs. Depending on the ratio between the substrate temperature and the melting-point temperature of the interested material, the formation of a stable sponge-like morphology can thus be obtained. In the particular case of Zn films deposited at room temperature, the energy-transfer mechanism from the incident particles to the substrate can locally increase the temperature by tens of degrees Celsius, allowing the achievement of the aforementioned condition and the formation of the resulting morphology. Zinc has a low melting temperature (≈ 420°C), and the substrate temperature required for obtaining a value of 0.5 is ≈ 80°C. The increase in the substrate temperature during sputtering deposition, and related to the energy released by incident particles [3], was thus the condition for obtaining such a nanostructure without intentional heating of the substrates.

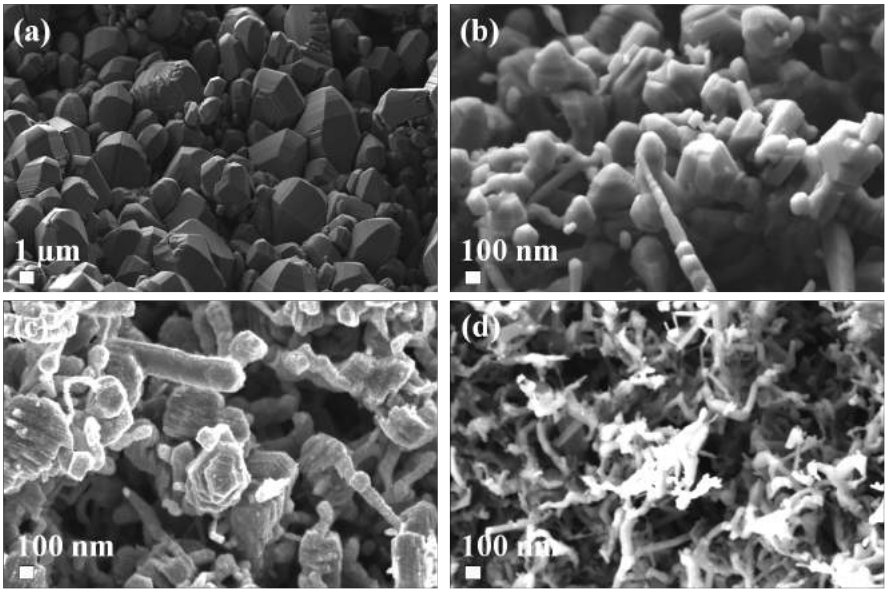

Figure 7.2. Particular of the surface morphology for Zn films deposited at: (a) 100 W, 5 mTorr; (b) 50 W, 5 mTorr; (c) 50 W, 10 mTorr; (d) 30 W, 5mTorr.

Fig. 7.3 shows the FESEM cross-section view of Zn films deposited on Si substrates. The average thickness was estimated to be in the range of 3.7 µm - 16.9 µm. It could be generally observed that the thickness values were different because of the different deposition conditions adopted for the growth of the films, and their variation was consistent with the mechanisms of growth involved in a sputtering process [4, 5]. In particular, the effect of the increase in the deposition rate with the increase of the RF power was clearly visible, as the thickest and thinnest samples Zn_100 and Zn_30 were obtained in the case of using the highest and the lowest RF power, respectively. The influence of the RF power on the deposition rate and on the final thickness was not linear as expected, being less pronounced for samples Zn_50 and Zn_30. Indeed, in this case just a slight decrease of the thickness was observed, with final values of 4.5 µm and 3.7 µm, respectively. Except for sample Zn_100, the presence of a porous nanostructure throughout the whole sample was observed from the cross-sectional analysis, confirming that the spatial distribution of this particular kind of nanostructure was uniform along all the film structure, from the surface up to the substrate. This aspect confirmed the formation of the porous structure in the Zn layer since the initial step of the deposition process.

From the analysis of the morphological characteristics of Zn films, the high quality of the sponge-like nanostructure of sample Zn_30, with a fine nanoporosity, could thus be highlighted. Indeed, only in this case the presence of nanostructures with a nanometer sized porous morphology was obtained, while it could be concluded that working with higher RF powers (50 W and 100 W) gradually changed the structure from a porous to a dense and compact one, completely loosing the sponge-like nanostructure. This is more evident from the comparison of samples Zn_30 and Zn_100, but a more compact structure respect to sample Zn_30 was also underlined for sample Zn_50.

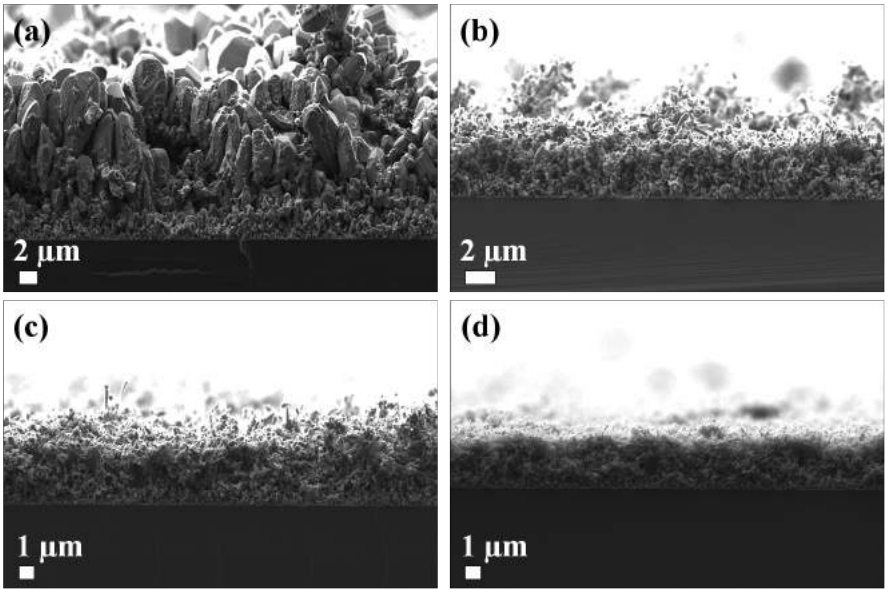

Figure 7.3. FESEM cross-sectional images of Zn films deposited on Si substrates in different conditions: (a) 100 W, 5 mTorr; (b) 50 W, 5 mTorr; (c) 50 W, 10 mTorr; (d) 30 W, 5mTorr.

In order to further investigate the possibility of obtaining sponge-like ZnO nanostructured layers starting from the Zn films deposited by sputtering, all the samples were oxidized by thermal treatment in air at 380°C for 120 min and the morphology of the oxidized samples was analyzed by FESEM. After the thermal treatment, the film morphology did not undergo any substantial modification, thus demonstrating the non-destructive nature of the oxidation step towards the morphology of the as-sputtered Zn films. This situation is well-represented by the FESEM images acquired on the sample Zn_30 after the thermal oxidation process, and reported in Fig. 7.4. From the cross-sectional view (Fig. 7.4(a)) it was clear that the thickness of the final ZnO layer was similar to the one of the starting Zn layer, while the top-view images acquired at different magnifications (Fig. 7.4(b)-(d)) showed that, although Zn and ZnO films had similar morphology, some small differences could be noticed. The as-grown Zn film consisted of branches that were slightly more elongated than those of the ZnO film. In addition, a compact layer appeared in the lowest part of the ZnO film (Fig. 7.4(a)) after the thermal oxidation. This modification of the porous structure can be probably due to a local softening of the material and the resulting local collapse of the pores.

The crystal structure and orientation of both Zn and thermally oxidized Zn films were investigated by XRD measurements. The XRD patterns were acquired on each sample, before and after the thermal oxidation process. Figs. 7.5 and 7.6 show the XRD pattern for all the Zn (black line) and oxidized Zn

(red line) samples, while Tables 7.2 and 7.3 summarize the diffraction peak positions detected for each sample, for the corresponding diffraction planes.

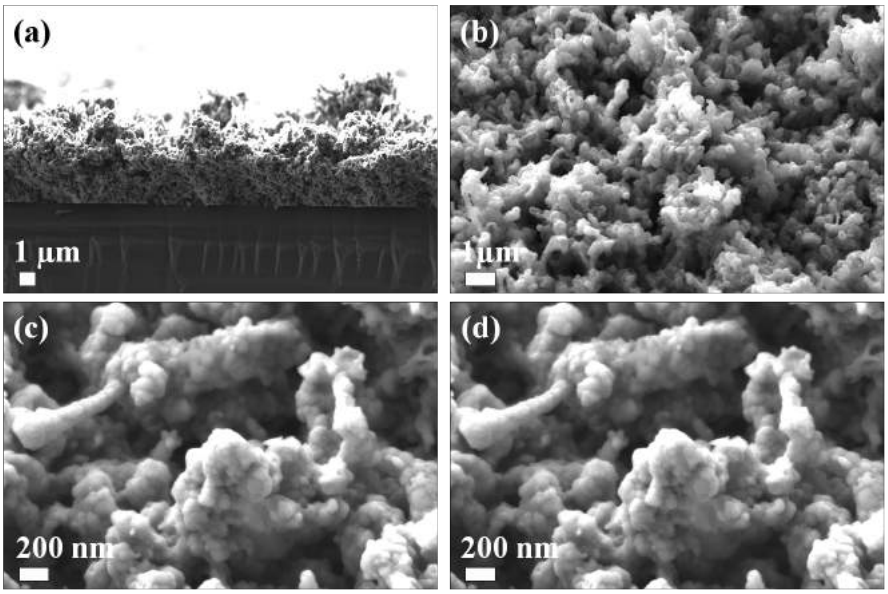

Figure 7.4. (a) Cross-sectional and (b) top-view FESEM images of sample Zn_30_OX - (c) and (d) show two particular aspects of sample Zn_30_OX acquired with a higher magnification.

The crystal structure of all the metallic Zn films was characterized by the presence of different diffraction peaks (labeled in the corresponding figures), associated to the Zn (002), Zn (100) and Zn (101) crystallographic planes. The strongest one was related to the Zn (101) phase, according to the ICDD database (JCPDS reference: Zn 87–0713).

The XRD patterns acquired on Zn films after the thermal treatment revealed the presence of the oxide phase in all the cases, thus representing the conversion of the starting Zn layer into ZnO. The presence of different peaks (labeled in the figure) corresponding to ZnO (100), ZnO (002), ZnO (101) and ZnO (102) crystal planes confirmed the presence of a randomly oriented polycrystalline structure in all the samples [6]. No residual crystallographic phases related to metallic Zn were detected in the diffraction pattern of the oxidized samples Zn_30, Zn_50 and Zn_50_10, confirming that a complete oxidation of the material was achieved. On the contrary, sample Zn_100 showed a residual contribution of zinc represented by the presence of Zn (100) and Zn (101) diffraction peaks, which were still present also after the oxidation treatment. This was representative of only a partial conversion of the metallic Zn layer into the oxide one.

	2ϑ position		
Sample	Zn (002)	Zn (100)	Zn (101)
Zn_30	36.28°	38.97°	43.22°
Zn_50	36.31°	38.97°	43.23°
Zn_50_10	36.30°	38.95°	43.22°
Zn_100	36.28°	38.96°	43.22°

Table 7.2. XRD peak positions of sponge-like Zn films.

	2ϑ position			
Sample	ZnO (100)	ZnO (002)	ZnO (101)	ZnO (102)
Zn_30_OX	31.93°	34.54°	36.53°	63.17°
Zn_50_OX	31.85°	34.63°	36.57°	63.12°
Zn_50_10_OX	31.88°	34.67°	36.58°	63.17°
Zn_100_OX	31.78°	34.43°	36.28°	62.92°

Table 7.3. XRD peak positions of sponge-like ZnO films.

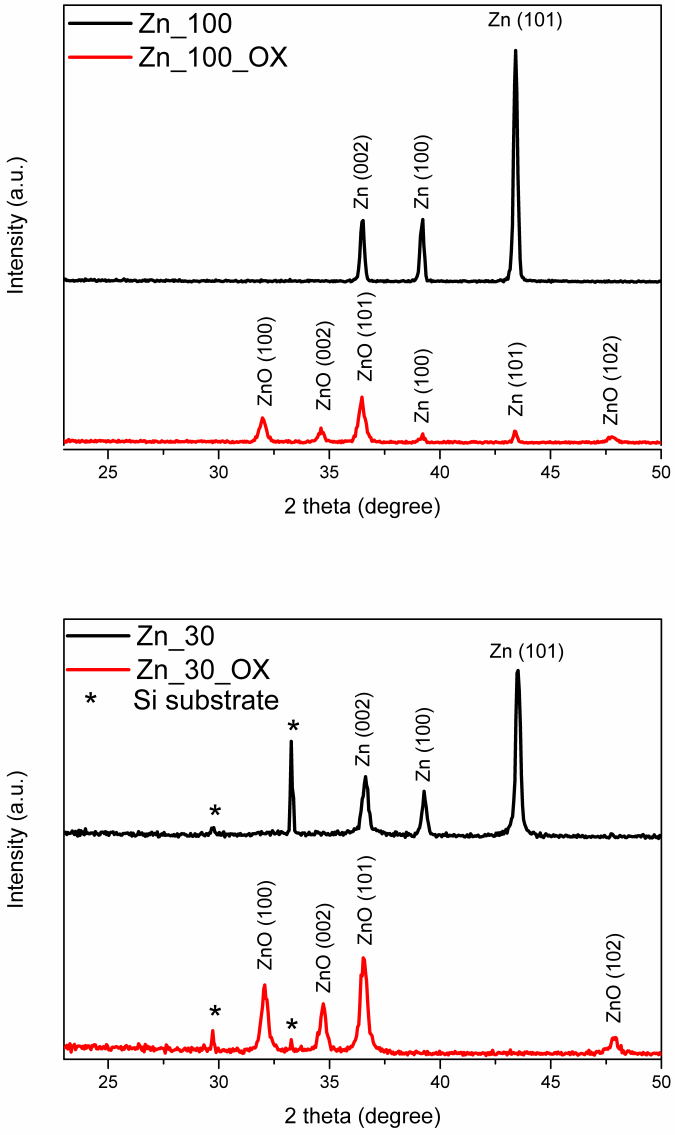

Figure 7.5. XRD pattern of sponge-like Zn (black line) and ZnO (red line) films - Samples Zn_30 and Zn_100.

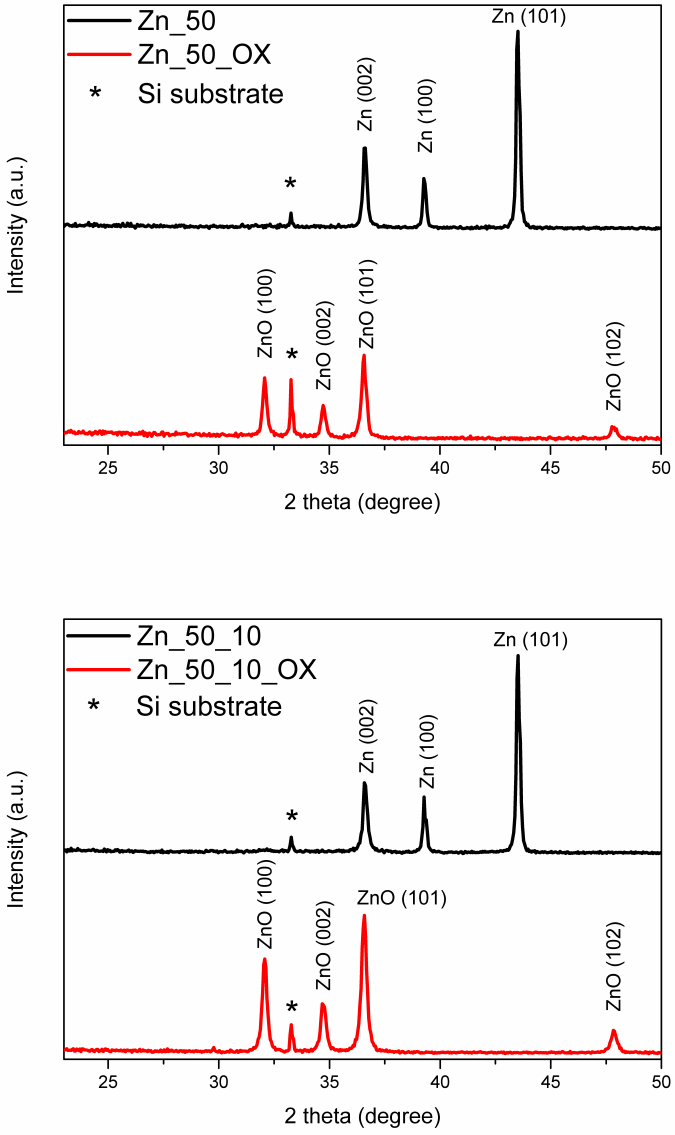

Figure 7.6. XRD pattern of sponge-like Zn (black line) and ZnO (red line) films - Samples Zn_50 and Zn_50_10.

From the diffraction pattern of samples grown at 30 W and 50 W, the good crystalline quality of the film, with the presence of a pure hexagonal structure could be confirmed. A good control in oxide stoichiometry could be evidenced, because no peaks related to metallic Zn were present after the thermal treatment, as stated before. The detected peaks were compared with the ICDD database (JCPDS reference: ZnO 89–1397) and the best agreement with the typical ZnO pattern was achieved in the case of sample Zn_30.

Since the XRD pattern revealed a polycrystalline structure, the texture coefficient (TC) associated to each crystallographic plane was estimated, in order to establish the presence of possible preferred crystal orientations. The TC was estimated according to the following equation [7, 8]:

$$TC\,(hkl) = \frac{I(hkl)/I_0(hkl)}{\frac{1}{n}\sum I(hkl)/I_0(hkl)}$$

, where (hkl) indicates the Miller indices of a particular crystal direction plane, n is the number of diffraction peaks considered, $I(hkl)$ and $I_0(hkl)$ are respectively the relative intensity of the diffracted peak associated to the (hkl) crystal planes and the one reported in JCPDS reference, for the same crystal plane in a ZnO reference sample with randomly oriented crystallites. If the TC of a particular crystal direction is found to be greater than one, an abundance of crystal grains with that crystal orientation is found, and a preferred orientation along the corresponding crystal direction can be supposed. The TC values of the different samples considerably changed, depending on the corresponding deposition conditions, and different crystal orientations were found. A slight preferred [101] orientation was found in sample Zn_100_OX. This turned into a [100] crystal orientation for the samples grown at 50 W, then it changed again for sample Zn_30_OX, for which a slight preferred orientation along the [001] direction was revealed. This last situation is the one of main interest in view of exploiting the piezoelectricity of sponge-like ZnO films. Indeed, the presence of a [001] crystal orientation is found to be mandatory for the promotion and the enhancement of ZnO piezoelectricity, as already widely discussed in Chapters 4 and 5.

7.2.2. Chemical composition analysis

FESEM and XRD characterization results highlighted the best quality of the oxidized sample Zn_30. In order to better investigate its properties, the chemical composition of this sample was analyzed by means of X-ray Photoelectron Spectroscopy (XPS), using a PHI 5000 VersaProbe (Physical Electronics) system, equipped with an Ar^+ gun, in order to remove any contaminant or pollutant from the surface of the analyzed material. The X-ray source was a Al K_α radiation. The XPS survey pattern, giving the global chemical composition of the analyzed sample, is reported in Fig. 7.7. This pattern was acquired after the cleaning process performed on the analyzed region, and before starting the measure. Contributions coming from Zn, O and C were detected. The sponge-like material, due to its high surface-to-volume ratio, is expected to expose a large surface area within the analyzed region. Thus, even after a cleaning process, there was still a large part of the surface, not subject to the ion bombardment, that was reached by the X-rays and analyzed. The presence of a so high C contribution, related to this aspect and ascribed to the presence of impurities, did not allow to make a precise estimation of the stoichiometry in the analyzed sample.

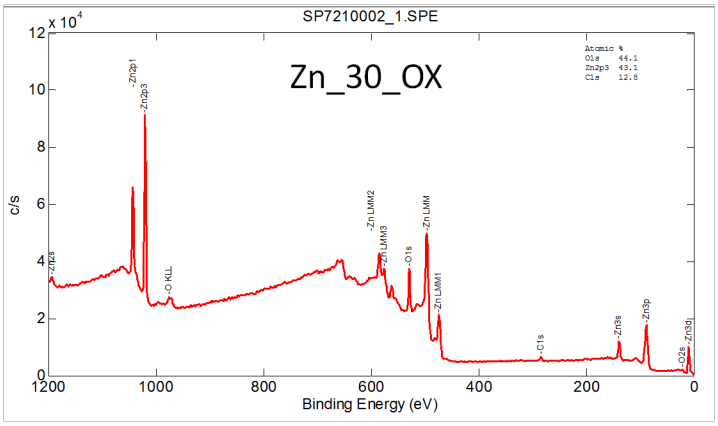

Figure 7.7. XPS survey pattern of sponge-like Zn films deposited on Si substrates, after the thermal oxidation treatment.

Nevertheless, an estimation of the amount of oxygen atoms bonded to zinc atoms was performed from the acquisition of high-resolution (HR) XPS spectra, by collecting the contribution coming from the O_{1s} and Zn_{2p} core electrons. The binding energies of Zn core electrons in the Zn\O and Zn\Zn bond configurations are very close to each other (1021.7 eV and 1021.5 eV, respectively) [9], thus the two corresponding peaks, which should be present in Fig. 7.8, were not resolved. As a consequence, there was no way of precisely estimating the percentage of Zn\O bonds from the Zn peaks. It was possible however to assert that oxygen was present in the sample and partially bonded to Zn atoms.

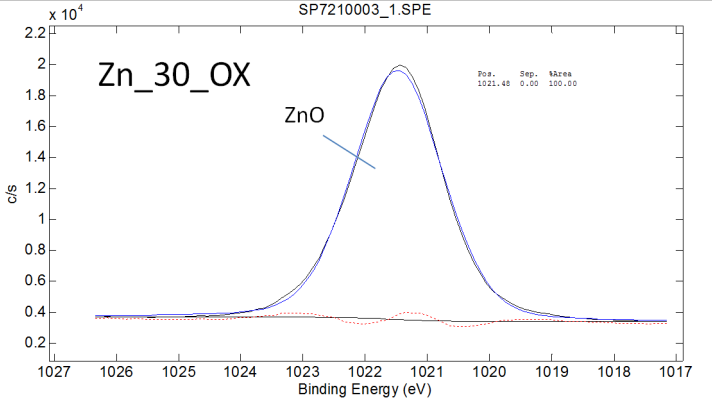

Figure 7.8. High-resolution XPS pattern of sponge-like ZnO films, related to Zn_{2p} core electrons.

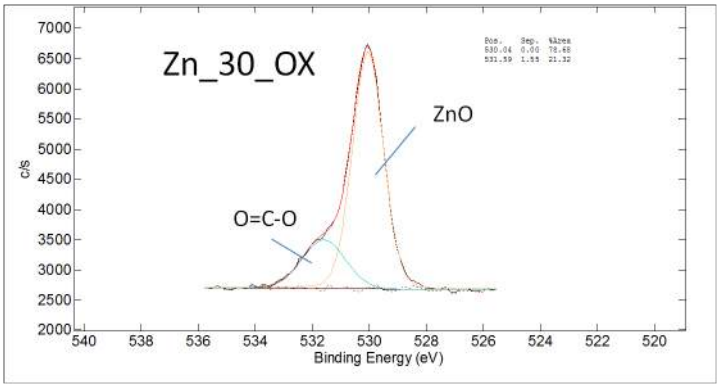

Figure 7.9. High-resolution XPS pattern of sponge-like ZnO films, related to O_{1s} core electrons.

The O_{1s} peak shown in Fig. 7.9 was fitted with two peaks centered at about 530.0 eV [10] and 531.5 eV [11], related to O\Zn bonds and O\H bonds, respectively. The area of the last peak, related to the presence of residual humidity in the chamber, was around 22% of the total O_{1s} peak area. The remaining part of oxygen (78%) was bound to zinc. Since part of the oxygen atoms was related to the presence of impurities, a slight oxygen deficiency in the ZnO layer can be supposed, thus the resulting sponge-like ZnO film was characterized by an excess of Zn atoms, in agreement with the results reported in the literature for ZnO-based nanomaterials.

7.2.3. Piezoelectric characterization of sponge-like ZnO thin films

The evaluation of the piezoelectric properties was performed on sponge-like ZnO films deposited on commercial glass substrates covered with a transparent conducting oxide, used as the bottom electrode. 100 nm-thick Pt metallic circular pads were deposited on the film surface by the co-sputtering system described in Chapter 3, Section 3.3.2, and used to contact the film surface to a probe. Displacement curves were collected by using a Piezo Evaluation System (PES, TFAnalyzer 2000HS, Aixacct) coupled to a single point laser vibrometer (Polytec OVF-505).

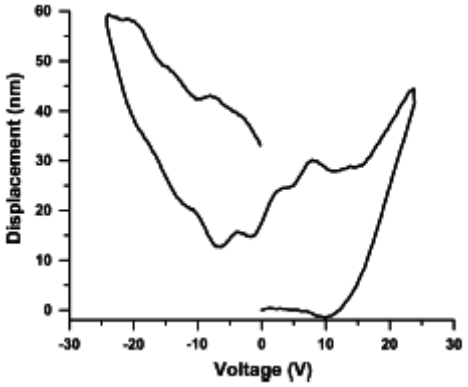

Figure 7.10. Typical displacement curve of sponge-like ZnO films deposited on a conductive glass substrate.

Fig. 7.10 reports the typical displacement curve of the sponge-like ZnO film. The anomalously high values (compared with the literature data [12]) of the displacement occurred at the different polarization conditions could be ascribed to a combination of different contributions. Indeed, in addition to the piezoelectric effect and to the displacement induced by the bending of the supporting substrate [13], a thermal contribution may also be considered, which could be addressed to the low resistivity of ZnO (if compared with PZT or $BaTiO_3$). With regard to the thermal contribution, the high leakage current flowing through the sample could be responsible for the expansion of the material due to joule heating. This hypothesis is further supported by the residual deformation collected at the end of the polarization cycles. The supporting substrate bending, instead, is caused by the stress induced by the piezoelectric material during the polarization step. It has been demonstrated that this effect can only be canceled by using interferential methods [13]. Thus a correct calculation of the piezoelectric constant is not possible because the thermal and the substrate bending contributions to the measured sample displacement could not be precisely estimated. Generally, the orientation of ZnO in the [001] direction helps maximizing the piezoelectric response of the material. In the present case, the random orientation of the polycrystalline structure, confirmed by XRD results, is expected to affect the piezoelectric performances.

7.3. Analysis of sponge-like Zn and water-vapor oxidized ZnO thin films

In the last years, one of the main goals of the scientific research was the fabrication of flexible devices. In view of this, one of the main challenges of the materials scientists was the development of functional materials through synthesis processes suitable for flexible applications. Generally, one way of improving

the properties of PVD grown materials is to exploit the positive effects of increasing the deposition temperatures or by performing post-deposition thermal treatments. However, this aspect cannot be considered when the final device might be conformable and flexible. Indeed, in the major part of these cases, polymers are used as substrates. It is generally known that this class of materials is not compatible with high-temperature processes, otherwise all the related characteristics in terms of mechanical and thermal stability would be lost. Thus, room-temperature synthesis methods need to be implemented. The two-step deposition method discussed up to now for growing sponge-like ZnO films is partially made without any heating, since the sputter deposition of the metallic Zn films was carried out at room temperature. However, in order to convert the metallic Zn layer into ZnO films, a thermal treatment was performed. In view of exploiting the physical properties of sponge-like ZnO films into flexible devices, a different method for the oxidation of the as-grown Zn films was implemented, being a completely low-temperature process and fully compatible with the use of polymeric substrates. The aim of the following section is to present and discuss the results obtained by the water-vapor oxidation technique applied to metallic Zn films, in order to show that a fully low-temperature method for the synthesis of sponge-like ZnO films was pursued, and could be successfully used for the integration of this material in flexible devices.

7.3.1. Morphology and structural analysis

Sponge-like metallic Zn films were deposited on hard Si substrates and commercial glass substrates covered with a transparent conducting oxide layer, by the RF magnetron sputtering technique. The set of the optimal deposition parameters selected in the previous section was used (30 W, 5 mTorr, Ar flow 10 sccm, 60 min). The resulting Zn films were oxidized at room temperature by the water-vapor oxidation method, already described in Section 7.1. Briefly, the sputtered Zn layers were fixed into a clamping system and exposed for 120 min to the water vapor deriving from De-Ionized (DI)-water (18 $M\Omega \cdot cm^{-1}$ at 25°C) heated at 90°C by an hot plate. The temperature of the substrate was monitored by a Pt100 thermocouple. The morphology and crystal structure of the samples were analyzed by means of FESEM and XRD characterization, with the set-up described in Section 7.3.1.

The morphological analysis confirmed that a sponge-like nanostructure was still present also in the water-vapor oxidized Zn films, as visible from the FE-SEM images reported in Fig. 7.11. The water-vapor oxidized sample exhibited slightly larger branches near the top of the film, with further nanostructuration of the branch surface; however, the overall sponge-like structure was preserved through the oxidation treatment.

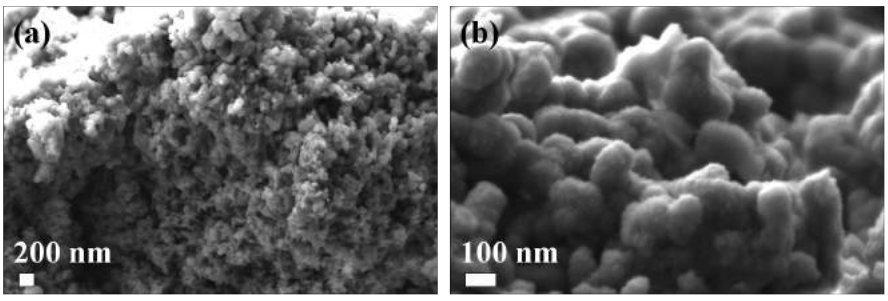

Figure 7.11. FESEM images of sponge-like Zn film oxidized at room temperature by water vapor.

The water vapor treatment can be described as a corrosion mechanism. The interaction of a metal surface exposed to water vapor is a highly complex in-

terfacial system since three phases (gas, liquid, and solid) and their interfaces (solid/liquid, liquid/gas and solid/gas) are involved [14]. Moreover the nanostructuration of the metal increases the complexity of the reaction affecting the oxidation rate. Leygraf and coworkers [15, 16, 17] have extensively investigated the corrosion mechanism of zinc exposed to water vapor at room temperature. Even though their studies were devoted to understand the atmospheric corrosion, the same approach can be useful to describe the low-temperature oxidation reported in this work. When the as-prepared samples were exposed to air, it was reasonable to believe that a thin oxide layer could form on the substrate surface. The exposure of the metal oxide surface to a water vapor led to the formation of a thin water film where the reversible processes of adsorption and desorption of water from the zinc surface could take place [15]. This aqueous layer was the medium in which the corrosion reaction occurred. Afterwards, electrochemistry guided the atmospheric corrosion process through the Zn/Zn^{2+} and O_2/H_2O redox couples, and anodic regions, where the zinc ions were released, and cathodic sites, where the electrons were consumed by forming hydroxide ions, could be localized [17]. The oxidation could be described by the subsequent chemical and electrochemical reactions:

$$Zn \rightarrow Zn^{2+} + 2e^-$$
$$\tfrac{1}{2}O_2 + H_2O + 2e^- \rightarrow 2OH^-$$
$$Zn^{2+} + 2(OH)^- \rightarrow Zn(OH)_2 \rightarrow ZnO + H_2O$$

At the end of the exposure treatment, the full oxidation of the nanostructured Zn layer occured, as clearly visible by the presence of diffraction peaks related to the hexagonal ZnO structure, reported in Fig. 7.12. As a comparison, the diffraction patterns of the as-grown Zn film and of the thermally oxidized ZnO film are also reported in Fig. 7.12. After both the oxidation treatments (i.e. thermal and water-vapor), a complete conversion of the material from metal to oxide was observed, without the occurrence of Zn residuals, as witnessed by the disappearance of the main Zn diffraction peak at 43.2° (2ϑ). As for the thermally treated samples, also the water-vapor assisted process gave rise to the formation of a randomly oriented polycrystalline network.

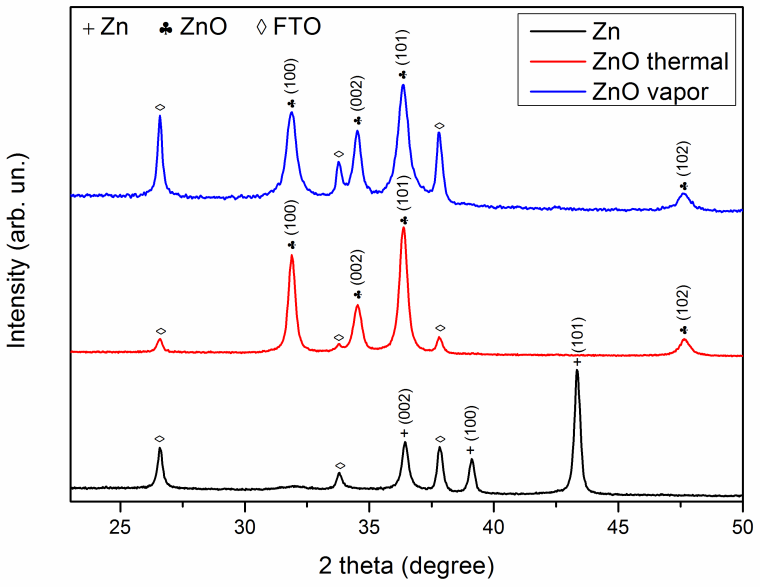

Figure 7.12. XRD pattern of sponge-like Zn film (black pattern), and of sponge-like ZnO films get by thermal (red pattern) and water-vapor (blue pattern) oxidation methods.

7.3.2. Chemical composition analysis

The chemical composition of water-vapor oxidized sponge-like ZnO films was evaluated by means of EDX measurements, carried out by a Oxford Instruments X-Max 50 mm^2 Silicon Drift Detector (SDD) for EDX analysis, coupled to the previously described FESEM set-up. A further insight into the analysis of the surface properties of sponge-like Zn and ZnO films came from Optical Contact Angle measurements, performed with an OCAH 200 instrument (DataPhysic Instruments GmbH). A water droplet with a volume of 1.5 µL was used and for each sample two drops were dispensed at two different positions on the sample surface.

The EDX spectrometry conducted on the water-vapor oxidized ZnO film is shown in Fig. 7.13 and confirmed the oxidation of the starting Zn layer. From this measure it could be possible to estimate the presence of a 57% and 43% atomic percentage for zinc and oxygen atoms, respectively.

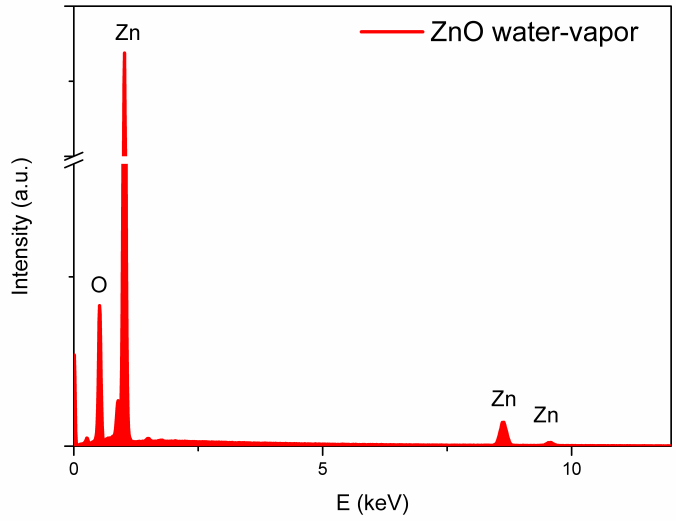

Figure 7.13. EDX spectroscopy on water-vapor oxidized sponge-like ZnO film.

The wetting behavior exhibited from both Zn and oxidized ZnO films is reported in Fig. 7.14, and was typical of a hydrophilic surface, with CA values by far lesser than 90°. However, some differences could be appreciated. The lowest CA value (Fig. 7.14(a)) was measured in the case of the metallic Zn layer. A slightly increase of the CA was observed for the water-vapor oxidized ZnO film (Fig. 7.14(b)) while the highest CA value was reported for the thermally oxidized one (Fig. 7.14(c)). Since the sponge-like structure of the starting Zn layer was maintained in both oxidized ZnO films, as visible by the comparison of FESEM results reported in Section 7.3.1 and 7.4.1, the differences observed could not be related to a possible variation in the nanostructure. Xu et al.[18] reported that the presence of surface defects like oxygen vacancies can promote the adsorption of hydroxyl groups (OH^-) on the surface of ZnO, inducing a hydrophilic behavior. A strong decrease in the number of adsorption sites for (OH^-) groups must be expected, leading to the observed wettability decrease of thermally oxidized ZnO films. Indeed thermal treatments are usually exploited to improve the crystal quality of metal oxides, reducing the presence of oxygen vacancies [19]. A more hydrophilic behavior was observed for the vapor oxidized

film. This could be ascribed to the water vapor-oxidation process, which was responsible for the introduction of a high number of surface defects, acting as adsorption sites for (OH^-) groups as stated previously.

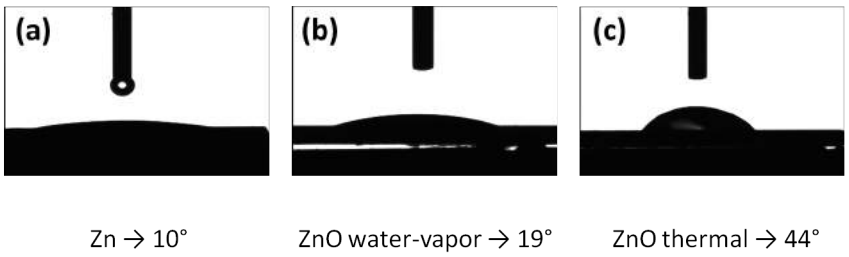

Figure 7.14. OCA measurements performed on (a) sponge-like Zn film, and on Zn films oxidized by (b) water-vapor and (c) thermal oxidation methods.

7.4. Conclusions

A simple two-step method, developed for growing sponge-like nanostructured zinc oxide films, was presented and the resulting materials were properly analyzed. The first step of this process consisted of growing metallic zinc films by the RF magnetron sputtering technique. Different deposition conditions were used and the resulting samples were properly analyzed by means of FESEM and XRD measurements. The morphology of the zinc films was found to be strictly dependent on the RF power used for the deposition, where compact zinc films were obtained with the highest value, while the sponge-like morphology was found to be present only when the lowest value was used. The presence of such a particular nanostructure was discussed and explained by the Thornton's "structure zone" model. XRD patterns highlighted the presence of the metallic phase in all the Zn samples, independently of the deposition conditions. The conversion of the metallic film into zinc oxide was achieved by a standard thermal oxidation process, carried out at 380°C for 120 min in ambient air. FESEM analysis confirmed that the morphological characteristics of the starting Zn layer were still present after the oxidation process while XRD confirmed the presence of the oxide phase after the thermal treatment, meaning that the conversion of Zn into ZnO was successfully achieved. This last condition, however, was only partially achieved in the case of the sample deposited at the highest RF power. The set of the optimal deposition parameters for growing sponge-like nanostructured ZnO films with a thickness of few micrometers was then selected according to the characterization results. The chemical composition of the sponge-like ZnO films was also analyzed by means of XPS, confirming the presence of oxygen atoms bonded to zinc atoms. Sponge-like ZnO films were also grown on conductive substrates, and the converse piezoelectric effect was analyzed.

In view of exploiting the properties of sponge-like ZnO films in the fabrication of flexible devices, a fully low-temperature oxidation approach to convert Zn nanostructures into sponge-like ZnO films was also presented. In this case, the prolonged exposure of the Zn metallic film to the action of water-vapor resulted in the conversion of Zn into ZnO. This was confirmed by the XRD characterization results, emphasizing the presence of diffraction peaks related to the oxide phase, which showed a hexagonal wurtzite-like crystal structure. FESEM analysis evidenced the sussistance of the sponge-like morphology of the starting Zn film after the water-vapor oxidation, as was noticed in the case of thermally treated samples. The chemical composition analysis further confirmed the presence of the oxide in the water-vapor oxidized Zn films, while optical

contact angle measurements highlighted the hydrophilic behavior of metallic, thermally oxidized and water-vapor oxidized sample surfaces.

Bibliography

[1] A.F. Jankowski, and J.P. Hayes, *J. Vac. Sci. Technol. A* **21** (2003) 422.
[2] J.A. Thornton, *Annu. Rev. Mater. Sci.* **7** (1977) 239.
[3] J. Musil, J. Matouš, and V. Valvoda, *Vacuum* **46** (1995) 203.
[4] K.B. Sundaram, and A. Khan, *Thin Solid Films* **295** (1997) 87.
[5] Z.X. Chen, B. Lu, Q. Huang, L. Wang, and B. Huang, *Mater. Sci. Eng. B* **117** (2005) 81.
[6] I. Petrov, P.B. Barna, L. Hultman, and J.E. Greene, *J. Vac. Sci. Technol. A* **21** (2003) S117.
[7] M.T. Htay, Y. Hashimoto, N. Momose, and K. Ito, *J. Cryst. Growth* **311** (2009) 4499.
[8] H.W. Kang, J. Yeo, J.O. Hwang, S. Hong, P. Lee, S.Y. Han, J.H. Lee, Y.S. Rho, S.O. Kim, S.H. Ko, and H.J. Sung, *J. Phys. Chem. C* **115** (2011) 11435.
[9] J.C. Klein, and D.M. Hercules, *J. Catal.* **82** (1983) 424.
[10] M. Chen, X. Wang, Y.H. Yu, Z.L. Pei, X.D. Bai, C. Sun, R.F. Huang, and L.S. Wen, *Appl. Surf. Sci.* **158** (2000) 134.
[11] L. Avalle, E. Santos, E. Leiva, and V.A. Macagno, *Thin Solid Films* **219** (1992) 7.
[12] Y.Q. Fu, J.K. Luo, X.Y. Du, A.J. Flewitt, Y. Li, G.H. Markx, A.J. Walton, and W.I. Milne, *Sens. Actuators, B* **143** (2010) 606-619.
[13] A.L. Kholkin, C. Wutchrich, D.V. Taylor, and N. Setter, *Rev. Sci. Instrum.* **67** (1996) 1935-1941.
[14] T.E. Graedel, *Corros. Sci.* **38** (1996) 2153-2180.
[15] P. Qiu, D. Persson, and C. Leygraf, *J. Electrochem. Soc.* **156** (2009) C81-C86.
[16] J. Hedberg, S. Baldelli, and C. Leygraf, *J. Phys. Chem. C* **113** (2009) 6169-6173.
[17] J. Hedberg, J. Henriquez, S. Baldelli, C.M. Johnson, and C. Leygraf, *J. Phys. Chem. C* **113** (2008) 2088-2095.
[18] S. Xu, and Z.L. Wang, *Nano Res.* **4** (2011) 1013-1098.
[19] R. Hong, J. Huang, H. He, Z. Fan, and J. Shao, *Appl. Surf. Sci.* **242** (2005) 346-352.

Chapter 8

Synthesis and characterization of Mn-doped and Sb- doped sponge-like ZnO thin films

Doping of ZnO is considered as one of the main challenges for material scientists. Generally undoped ZnO thin films are reported to have an intrinsic n-type behavior, which makes them highly suitable for transparent conducting oxides production. A high electrical conductivity is required in these cases. However, this intrinsic n-type conductivity is detrimental when ZnO piezoelectricity wants to be pursued. Higher values of the electrical resistance would be preferable for this purpose, but this aspect is strongly limited by the presence of native defects like oxygen vacancies and/or zinc interstitials, which give to undoped ZnO its natural n-type behavior.

In the last years a lot of efforts of the scientific research were devoted to compensate the n-type characteristic of undoped ZnO thin films through p-type doping. The main goal of this technique is the lowering of the electrical conductivity of the undoped specimens, promoting the piezoresponse from more insulating, p-type doped ZnO films. Generally, substitutional doping consists in the substitution of atoms with other chemical elements, having an atomic radius as much as possible similar to the substituted one. In the case of ZnO, Zn atoms are substituted by bigger or smaller doping elements, which should in turn result in the lattice distortion of the crystal cell. In addition to this, it is expected a compensating effect of the introduced dopant on the crystal defects like oxygen vacancies and/or zinc interstitials, which are considered as the main factors causing the n-type behavior of the undoped specimens, as previously discussed.

This Chapter reports on a simple and effective way for doping sponge-like ZnO thin films with two different doping elements, i.e., antimony (Sb) and manganese (Mn). The synthesis process consists of three main steps. In the first one, metallic Zn films are deposited by the RF magnetron sputtering technique, with the system described in Chapter 3, Section 3.3.1. Suitable deposition parameters are selected on the basis of the results described in Chapter 7, in order to obtain a sponge-like structure, with nanometer-sized pores and exposing a highly active surface area. The presence of the porous structure is fully exploited in the second step of the synthesis process, when the sponge-like Zn films are soaked in two different solutions, containing the doping element. Sb-based and Mn-based solutions are used for this scope. For each doping solution, different soaking times are used. Finally, all the impregnated samples are thermally oxidized, in order to achieve the conversion of the metallic Zn film into ZnO, and to promote the diffusion and the insertion of the dopant into the crystal structure of the final ZnO film.

8.1. Growth conditions

The synthesis technique for the preparation of Sb-doped and Mn-doped ZnO thin films can be described as a simple, three-step method. Briefly, sponge-like Zn films were first deposited on commercial glass covered with Fluorine-doped Tin Oxide (FTO), by the RF magnetron sputtering technique. In addition to this, commercial glass slides covered with Indium Tin Oxide (ITO) were also used as substrates, in order to easily perform cross-sectional FESEM analysis of the doped ZnO samples, because of the reduced thickness of ITO/glass slides with respect to the FTO/glass ones. The as-grown Zn films were then soaked with two different solutions, one for each doping agent. After different soak-

ing times, the samples were thermally treated in ambient air, in order to get the conversion of the metallic Zn film into ZnO, and to promote the diffusion and the subsequent substitution of the dopant into the crystal structure of the sponge-like ZnO film. In the following, each of these steps will be properly described.

Commercial FTO/glass and ITO/glass slides were used as substrates, in order to provide a conductive support, and being also able of undergoing the final thermal treatment. Before starting the deposition process each substrate was properly cleaned with a Piranha solution for 10 min, then with ultrasound baths of bidistilled water, and finally treated with a 5 min plasma cleaning, in Ar atmosphere. A small area of the substrate surface was properly masked, in order to prevent the deposition of the sputtered material onto the whole substrate surface, providing in this way the free area acting as bottom electrical contact necessary for carrying out the further electrical and piezoelectrical characterizations.

Zn films were deposited by the RF magnetron sputtering technique. The deposition process used for growing sponge-like Zn films was already discussed in Chapter 7, Section 7.1. Briefly, a 4" diameter Zn target was used as the starting source material, and connected to a RF signal generator, working at a frequency of 13.56 MHz. A fixed power value of 30 W was used for the deposition of all the samples. All the depositions were performed in a pure Ar atmosphere, by setting the gas flow and pressure at 10 sccm and 5 mTorr, respectively. No intentional heating was provided to the substrates. The as-reported deposition conditions resulted from the optimization process accurately described in Chapter 7, for growing sponge-like ZnO films with a highly active surface area and characterized by the presence of interconnected nanometer-sized pores throughout the whole film structure.

The sputtered Zn films were then soaked with Sb-based and Mn-based dopant solutions. Antimony acetate ($C_6H_9O_6Sb$, Sigma Aldrich, 99.98% purity) and manganese acetate ($(CH_3CO_2)_2Mn$, Sigma Aldrich, 99.99% purity) were used as the starting chemical precursors, providing the desired doping elements. Both the solutions were prepared by the addition of the starting precursors to bi-distilled water, and by stirring until their complete dissolution. The final concentrations for the Mn-based and Sb-based solutions were of 2 mg/ml and of 0.25 mg/ml, respectively. Both the solutions were pH 7, with a final total volume of 50 ml. Then, the Zn films were soaked in the as-prepared solutions under stirring, at different impregnation times. Samples were impregnated for 2h, 4h and 6h in the case of the Mn-based solution, while for the Sb-based one the samples were soaked for 2h and 4h. No 6h impregnation was possible in this case, since after this prolonged time a total dissolution of the Zn film was observed.

The last step of the synthesis process consisted in the thermal treatment of all the impregnated samples at 380°C, for 120 min in a muffle furnace working in ambient air.

8.2. Analysis of Mn-doped sponge-like ZnO thin films

This Section presents all the scientific results obtained from the characterization of sponge-like ZnO thin films doped with Mn. First, the morphology and the crystal structure of the samples are described by Field Emission Scanning Electron Microscopy and X-Ray Diffraction, respectively. After that, the chemical composition is analyzed by two different spectroscopy techniques, the Energy Dispersive X-ray spectrometry and the X-ray Photoelectron Spectroscopy. A further insight into the characterization of the Mn-doped ZnO film is given by the analysis of the vibrational properties, by means of Raman spectroscopy, while the optical properties are studied by UV-Vis measurements. In conclusion, the analysis of the electrical and ferroelectric behavior of the Mn-doped sponge-like ZnO films is discussed.

8.2.1. Morphological and structural characterization

The morphology and thickness of Mn-doped sponge-like ZnO samples were investigated using a Carl-Zeiss Dual Beam Auriga, consisting of a Field Emission Scanning Electron Microscope (FESEM) and Focused Ion Beam (FIB). The crystal structure and orientation of the doped samples were analyzed by X-Ray Diffraction (XRD) measurements using a Panalytical X'Pert X-ray diffractometer in the Bragg-Brentano configuration. A Cu K_α monochromatic radiation was used as X-ray source, with a characteristic wavelength $\lambda = 1.54059$ Å.

The FESEM images of the impregnated samples deposited on FTO/glass substrates are reported in Fig. 8.1 for samples Zn_Mn_2h and Zn_Mn_4h, and in Fig. 8.2 for sample Zn_Mn_6h. All the samples showed a morphology similar to the one of the undoped, sponge-like ZnO sample, already reported in Chapter 7 and obtained by using the set of the optimal deposition parameters of sample ZnO_30. After the impregnation process and the thermal treatment, the presence of uniform nanostructures on the whole surface could be stated for samples impregnated for 2h and 4h. On the contrary, non uniformities were noticed in the surface morphology of sample Zn_Mn_6h, i.e., the sample which undergone to the longest impregnation time. In this case (Figs. 8.2(a) and 8.2(b)), some regions still showed morphological characteristics similar to the ones reported from the samples impregnated for 2h and 4h. However it was observed also the presence of micrometric structures, covering the underlying nanostructures (see Figs. 8.2(c) and 8.2(d)). It was supposed that these microstructures started to take place as a consequence of the formation of Mn precipitates, because of the prolonged impregnation time (6h).

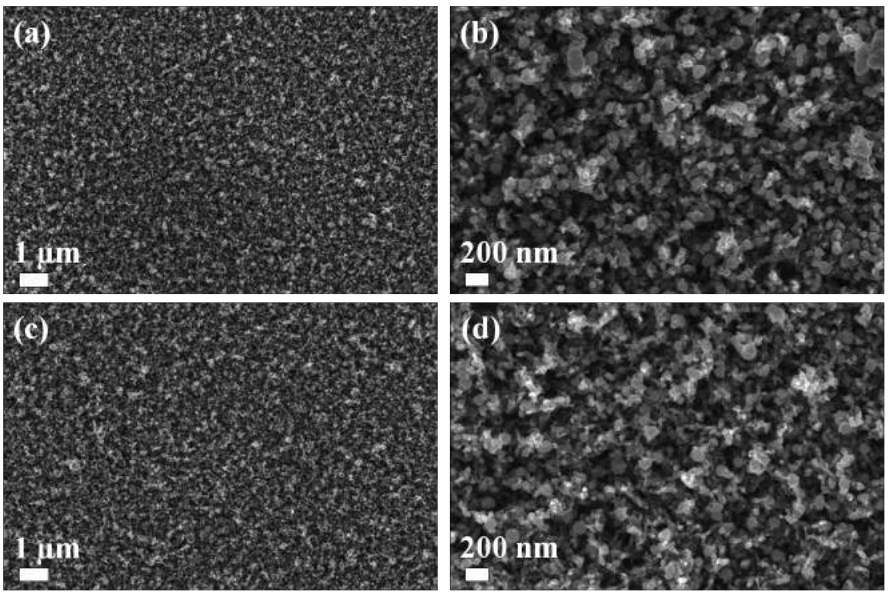

Figure 8.1. FESEM images showing the surface morphology of samples (a-b) Zn_Mn_2h, and (c-d) Zn_Mn_4h.

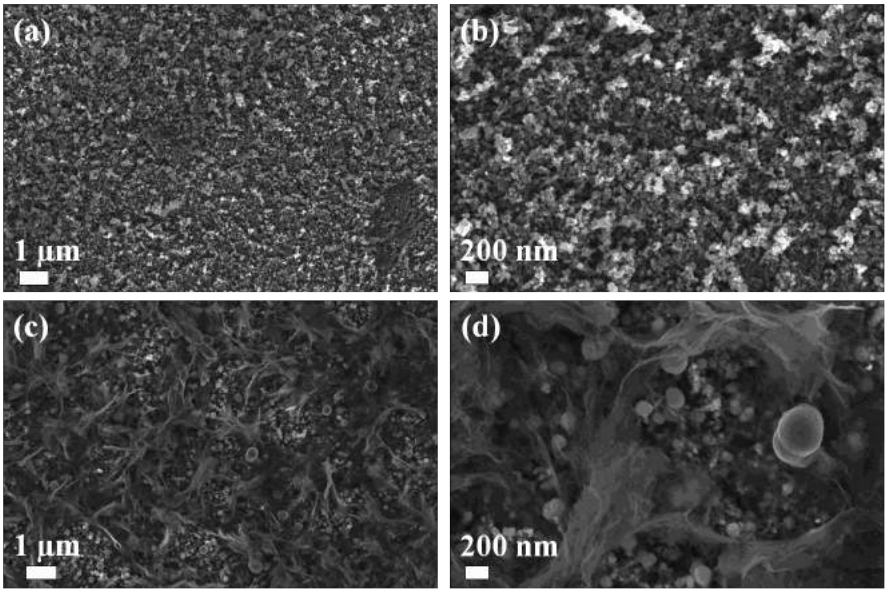

Figure 8.2. FESEM images showing the differences in the surface morphology of sample Zn_Mn_6h.

The average thickness of the Mn-doped ZnO samples deposited on ITO/glass substrates was investigated by cross-sectional FESEM imaging, reported in Fig. 8.3. The estimated thickness was of about 1.2 μm for samples impregnated at 2h and 4h, while a slight thickness reduction of the 6h-soaked sample was observed, being 1 μm - 1.1 μm thick. Despite the difference in the final average thickness, the presence of a uniform nanostructure along the whole sample could be observed, independently of the impregnation time.

From FESEM analysis, the non destructive characteristics of the three-step process followed in this work for the synthesis of Mn-doped, sponge-like ZnO films could be underlined, since the morphological characteristics of the starting Zn film were somehow preserved. No differences in the surface morphology were observed between the samples grown on FTO/glass and the ones deposited on ITO/glass substrates, confirming that the nature of the substrate did not influence the nanostructure of the resulting film.

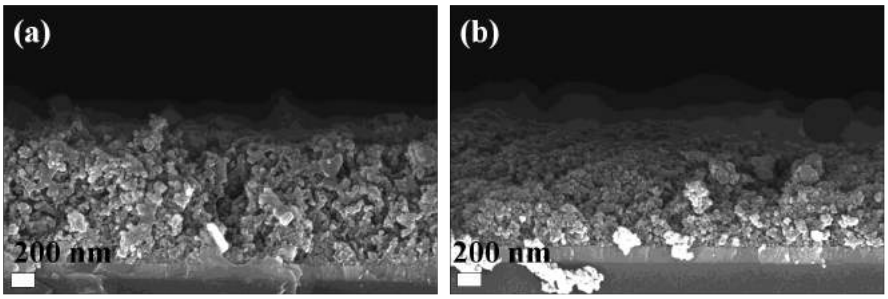

Figure 8.3. Cross-sectional FESEM images of samples (a) Zn_Mn_4h, and (b) Zn_Mn_6h.

Fig. 8.4 shows the XRD patterns acquired both on undoped and Mn-doped sponge-like ZnO films. The hexagonal and polycrystalline characteristics of the crystal structure in the undoped sponge-like ZnO film was confirmed by the presence of different diffraction contributions coming from the ZnO (100), ZnO

(002), and ZnO (101) crystal planes. All these contributions were also detected from the doped samples, confirming that the hexagonal, wurtzite-like crystal structure was still present after the doping process [1]. No trace of Mn metal, oxides, or any binary Zn-Mn phases were observed in any of the Mn-doped samples, since only reflections coming from the hexagonal wurtzite ZnO network were detected, as reported in Fig. 8.4.

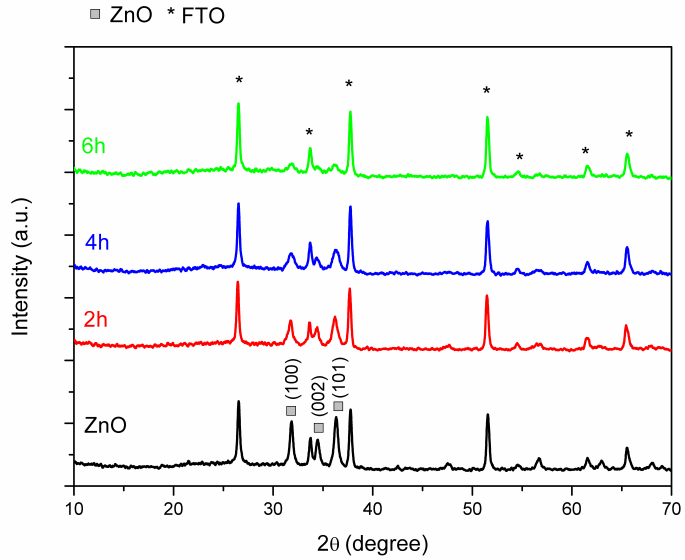

Figure 8.4. XRD patterns of samples Zn_Mn_2h (red line), Zn_Mn_4h (blue line), and Zn_Mn_6h (green line). As a comparison, the diffraction pattern of the undoped sponge-like ZnO film is also reported (black line). Peaks labeled by $*$ represent the substrate diffraction contribution.

The diffraction peaks of the Mn-doped samples became weaker and broadened, as the impregnation time increased from 2h to 6h. This aspect is clearly visible from Figs. 8.5 and 8.6, where the enlarged ZnO (100) and ZnO (101) diffraction peaks are reported. The enlarged ZnO (002) diffraction peak could not be reported because of its overlapping with a stronger diffraction peak coming from the FTO layer present in the substrates.

	Peak position		
Sample	ZnO (100)	ZnO (002)	ZnO (101)
Undoped ZnO	31.85°	34.49°	36.33°
Zn_Mn_2h	31.75°	34.43°	36.27°
Zn_Mn_4h	31.83°	34.37°	36.27°
Zn_Mn_6h	31.89°	34.39°	36.11°

Table 8.1. Diffraction peak positions detected for undoped and Mn-doped sponge-like ZnO films.

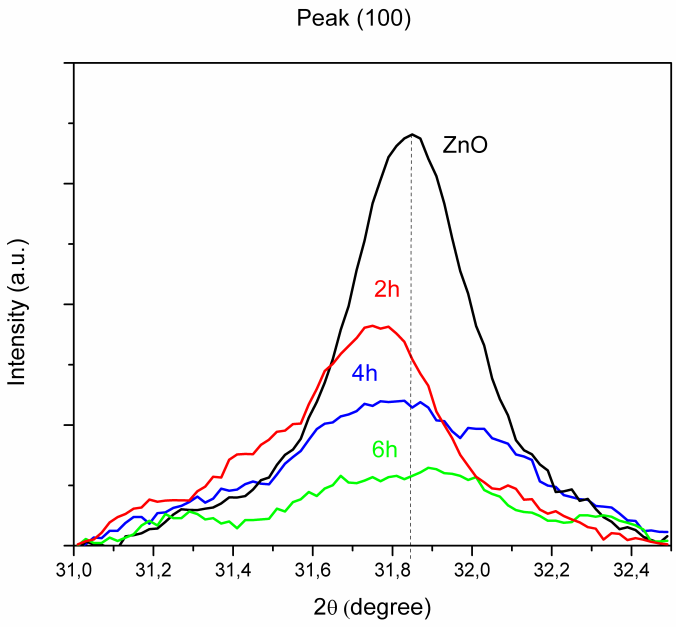

Figure 8.5. Particular of the ZnO (100) diffraction peak detected for the undoped and Mn-doped ZnO films, impregnated for 2h, 4h, and 6h.

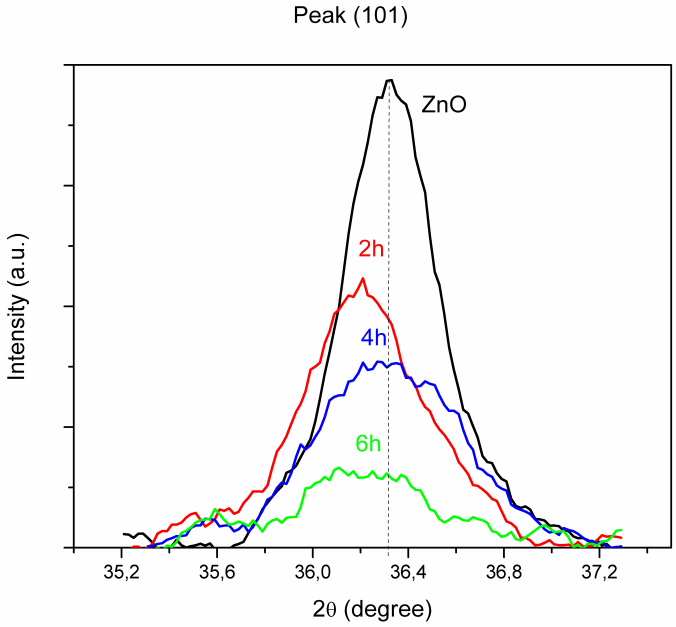

Figure 8.6. Particular of the ZnO (101) diffraction peak of the undoped and Mn-doped, sponge-like ZnO thin films, impregnated for 2h, 4h, and 6h.

The peak positions for all the Mn-doped ZnO films are listed in Table 8.1 and compared with those of the undoped specimen. An overall shift towards lower 2ϑ angles was underlined for all the Mn-doped samples. The presence of weaker and broadened diffraction peaks, together with a change in the diffraction peak positions, indicated lattice defects formation [2], and could be representative

of the substitution of Mn ions with a large ionic radius of 0.83 Å for Zn sites (0.74 Å) [1, 3]. Also the Mn content influenced the crystal structure of ZnO films [4], since the intensity of the diffraction peaks decreased with increasing the impregnation time and consequently with the Mn content. Moreover, the difference in the shift of the diffraction peaks described previously could be representative of the fact that Mn was incorporated into the wurtzite lattice with different Mn ionic size. Since the ionic radius of Mn ions is larger than the one of Zn ions, a strong distortion of the crystalline cell was expected, causing the observed shift to lower diffraction angles.

8.2.2. Chemical composition analysis and vibrational properties

The chemical composition of Mn-doped ZnO films was first evaluated by means of EDX measurements, carried out by a Oxford Instruments X-Max 50 mm^2 Silicon Drift Detector (SDD) for EDX analysis, coupled to the previously described FESEM set-up. The EDX spectrometry carried out on the samples impregnated for 2h and 4h is reported in Fig. 8.7, together with the FESEM images showing the corresponding area of the sample on which the EDX measure was performed. FESEM analysis already pointed out the uniformity of the samples impregnated for 2h and 4h, but the presence of inhomogeneity on the sample impregnated for the longest time (6h) was underlined. In order to see if these non uniformity in the sample could influence the presence of the Mn dopant or not, EDX spectrometry on sample Zn_Mn_6h was carried out on two different regions of the same area, showing different morphological aspects (see Fig. 8.8).

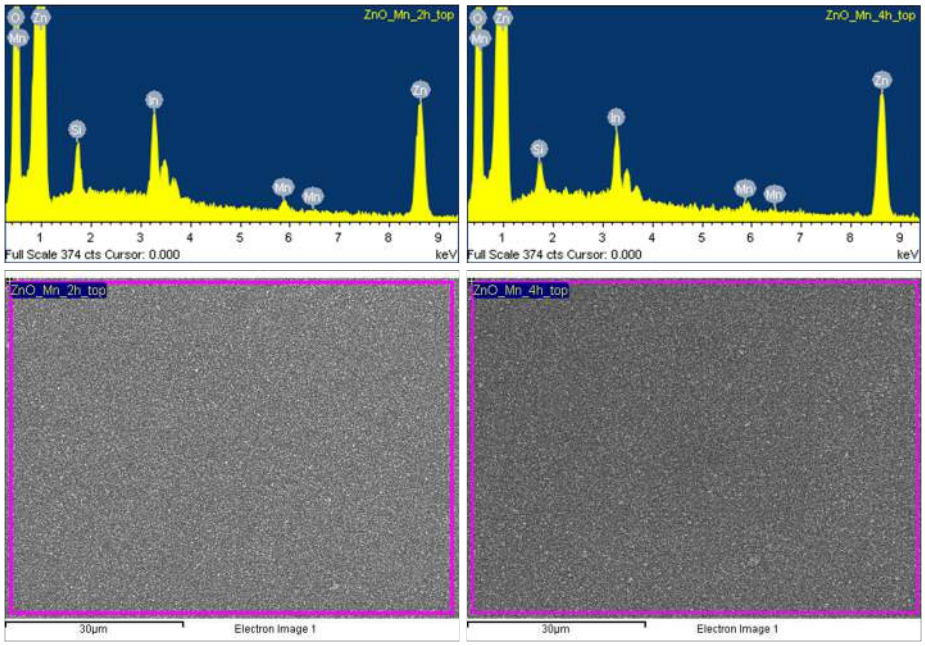

Figure 8.7. EDX spectrometry of samples Zn_Mn_2h and Zn_Mn_4h.

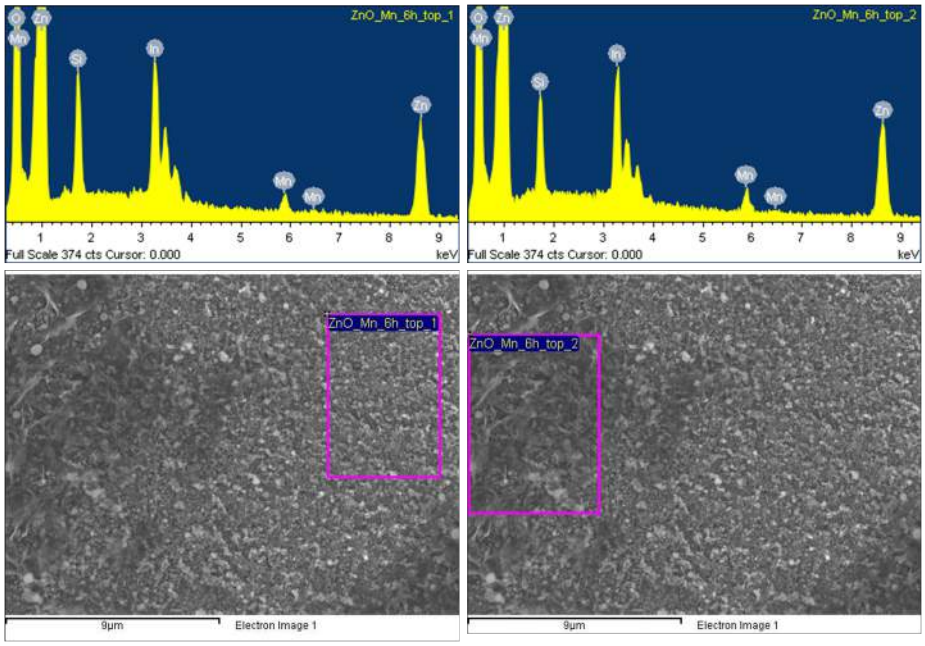

Figure 8.8. EDX spectrometry of sample Zn_Mn_6h performed on two different regions of the sample surface, having different morphological aspects.

Element	Impregnation time	Atomic %
O K	2h	54.27
	4h	54.37
	6h	58.14
Zn L	2h	41.99
	4h	40.54
	6h	33.35
Mn K	2h	0.62
	4h	0.82
	6h	1.39
In L	2h	1.99
	4h	2.46
	6h	3.64
Si K	2h	1.14
	4h	1.82
	6h	3.47

Table 8.2. Atomic percentage of the chemical elements detected by EDX spectrometry in the Mn-doped ZnO samples.

The detected chemical elements in each sample were oxygen, zinc, and manganese, confirming the presence of the Mn dopant in each case. Also silicon and indium were observed, and could be ascribed to the contribution of the underlying ITO/glass substrate. EDX spectrometry is based on the detection of the X-rays emitted after the interaction of the material with the primary electron beam incident on the sample. Since the energies of the emitted X-rays are characteristic of each chemical element, the chemical composition can be defined. However, the volume of interaction of the incident beam with the sample not only involves the analyzed material, i.e., the Mn-doped ZnO film in this case, but also part of the substrate. Indeed, the penetration depth of the primary beam is of several micrometers. Since the average thickness of the

analyzed materials is of around 1 μm - 1.2 μm, a contribution on the X-ray emission spectra, coming from the underlying substrate, could be expected. For this reason, the EDX spectrometry did not allow to exactly know the stoichiometry of the analyzed samples.

The quantitative analysis of the detected chemical elements, for the Mn-doped samples, is summarized in Table 8.2. The Mn-content of the doped samples was observed to increase with increasing the impregnation time. The estimated Mn atomic percentages were of 0.62 %, 0.82 %, and 1.39 % for the 2h, 4h, and 6h impregnated samples, respectively. On the contrary, the Zn atomic percentage decreased for longer impregnation times. The reason of this depletion could be explained by considering the mechanism at the basis of ZnO doping, which consisted in the replacement of Zn sites with Mn ions, into the ZnO crystal structure. For a higher Mn content, the number of Zn sites substituted by Mn ions increased too, thus lowering the total amount of Zn present in the sample. The EDX analysis did not confirm a linear increase of Mn incorporation with increasing the impregnation time. Moreover, in the case of the non-uniform morphology of the sample Zn_Mn_6h, the EDX measurement showed that no substantial differences in the Mn content were present, despite the different morphological aspects of the analyzed regions.

Since a quantitative evaluation of the doping content and stoichiometry could not be exactly carried out by EDX measurements, X-ray Photoelectron Spectroscopy (XPS) analysis was performed on the Mn-doped sponge-like ZnO films. In this case, just the first nanometers of the sample surface were analyzed, allowing to exclude the contribution of the underlying substrate from the measure. Moreover, the chemical state of the doping element could also be evaluated. In this way, the presence and the content of the dopant in the samples were investigated, together with the analysis of the chemical bonds involving the dopant.

XPS measurements were carried out by using a PHI 5000 VersaProbe (Physical Electronics) system, equipped with an Ar^+ gun, in order to remove any contaminant or pollutant from the surface of the analyzed material. The X-ray source was a Al K_α radiation.

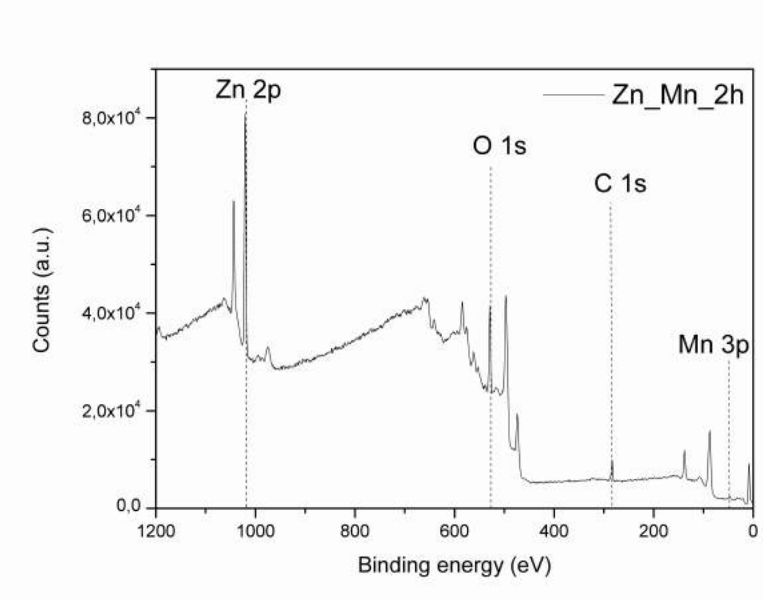

Figure 8.9. Survey XPS pattern of sample Zn_Mn_2h.

The XPS survey spectra are reported in Figs. 8.9, 8.10, and 8.11 for the Mn-doped samples impregnated for 2h, 4h, and 6h, respectively. From this first

analysis, all the chemical elements present in the analyzed samples could be identified, together with their relative atomic percentage, which are summarized in Table 8.3. For each of the considered samples, the same elements were detected; carbon, oxygen, zinc, and manganese. The presence of a high carbon content, ranging from 32.89% to 34.55%, was revealed and already discussed in Chapter 7, Section 7.3.2, for the sponge-like ZnO morphology, and ascribed to the contaminants and pollutants absorbed on the high active surface area exposed in this particular case.

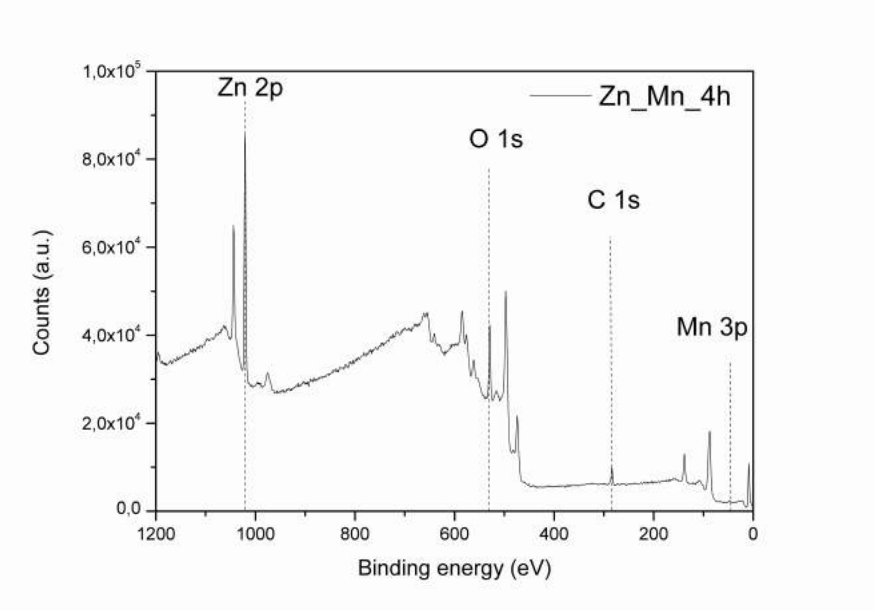

Figure 8.10. Survey XPS pattern of sample Zn_Mn_4h.

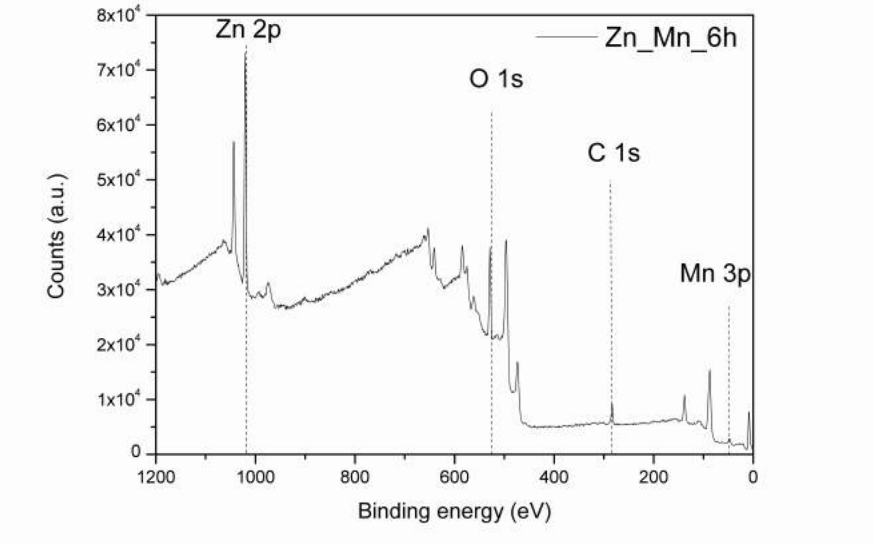

Figure 8.11. Survey XPS pattern of sample Zn_Mn_6h.

From the quantitative estimation of the atomic percentage of each detected chemical element reported in Table 8.3, a slight increase in the Mn content, changing from 3.07 % to 3.91 %, between the samples impregnated for 2h and 4h could be observed. Then, it strongly increased for the 6h- impregnated sample (7.21 %). As the presence of Mn increased, a decrease in the Zn atomic percentage could also be noticed, changing from 14.73 %, to 13.29 % and 11.98% for the samples impregnated at 2h, 4h, and 6h, respectively. The absence of a linear increase in the Mn content with increasing the impregnation time was already observed from EDX spectroscopy, and thus further confirmed by XPS analysis.

Sample	Element	Atomic %
Zn_Mn_2h	C_{1s}	34.19
	O_{1s}	48.10
	Zn_{2p}	14.73
	Mn_{3p}	3.07
Zn_Mn_4h	C_{1s}	34.55
	O_{1s}	48.25
	Zn_{2p}	13.29
	Mn_{3p}	3.91
Zn_Mn_6h	C_{1s}	32.89
	O_{1s}	47.92
	Zn_{2p}	11.98
	Mn_{3p}	7.21

Table 8.3. Atomic percentage of the chemical elements detected by XPS in the Mn-doped ZnO samples.

From the XPS survey spectra it was not possible to establish if the detected Mn acted as a doping element, or if its presence was related to the formation of Mn metallic or oxide phases. Despite this aspect was already excluded from the XRD results, to better understand the role of the incorporated Mn, high-resolution (HR) measurements were performed by collecting the O_{1s}, Zn_{2p} and Mn_{2p} core-electrons contribution.

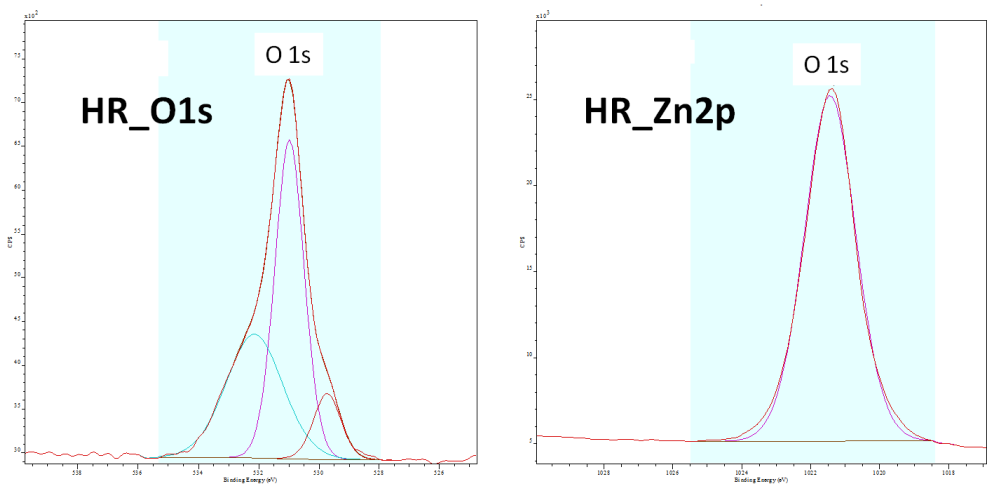

Figure 8.12. HR O_{1s} and Zn_{2p} XPS spectra of sample Zn_Mn_2h.

For simplicity, in Fig. 8.12 are shown only the HR spectra collected for the 2h-impregnated sample, since no relevant changes were observed for the

samples impregnated for higher times. From the fitting of the spectra shown in Fig. 8.12, no peaks related to the presence of Zn-Mn and O-Mn chemical bonds were detected, while the peak positioned at 531 eV and 1021.44 eV respectively in the O_{1s} and Zn_{2p} spectra allowed to confirm the formation of Zn-O chemical bonds.

A further insight into the study of the Mn chemical state came from the HR measurements performed considering the HR Mn_{2p} core-electrons contribution, showed in Figs. 8.13, 8.14, and 8.15, for the samples impregnated for 2h, 4h, and 6h, respectively. The characteristic peaks of Mn are centered respectively at 640 eV for Mn^{2+} ions, 642.6 eV for Mn^{3+} ions and 645 eV for Mn^{4+} ions. In the case of the Mn-doped samples of this work, only the peak related to Mn^{2+} ions was detected, as represented by the peaks centered at 640.28 eV, 640.35 eV, and 640.66 eV in the Mn_{2p} spectra of samples Zn_Mn_2h, Zn_Mn_4h, and Zn_Mn_6h, respectively [5, 6]. The observed shift of the binding energy of Mn_{2p} peaks towards lower values, respect to the 640.7 eV reported for commercial MnO powders, was related to the insertion of Mn^{2+} ions into the lattice position of Zn in the host ZnO crystal structure [5].

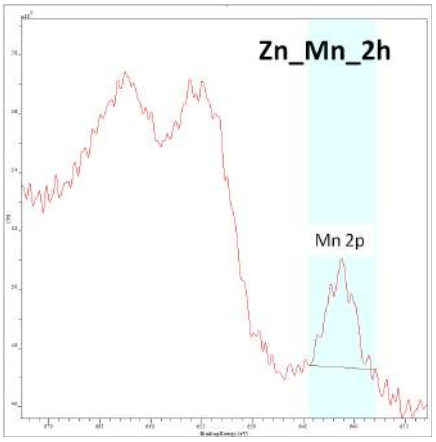

Figure 8.13. HR XPS spectrum of sample Zn_Mn_2h, related to Mn_{2p} core-electrons.

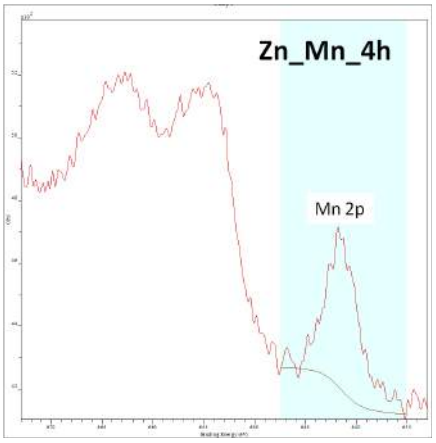

Figure 8.14. HR XPS spectrum of sample Zn_Mn_4h, related to Mn_{2p} core-electrons.

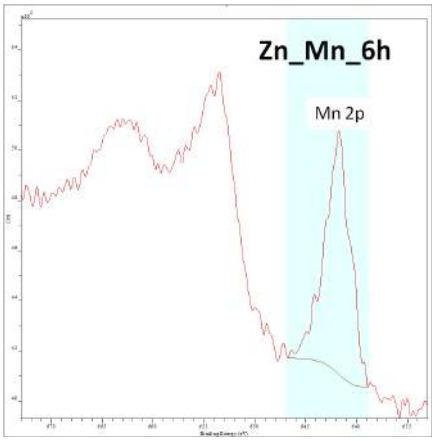

Figure 8.15. HR XPS spectrum of sample Zn_Mn_6h, related to Mn_{2p} core-electrons.

The vibrational properties of Mn-doped ZnO thin films were investigated by means of Raman spectroscopy measurements, using a Renishaw inVia Reflex (Renishaw PLC, UK) micro-Raman spectrophotometer equipped with a cooled CCD camera. Samples were excited with an Ar - Kr laser source with $\lambda = 514.5$ nm.

Raman spectra collected for the samples impregnated for 2h, 4h, and 6h are reported in Fig. 8.16. The strongest peaks positioned at 101 cm^{-1} and 437 cm^{-1} were assigned to the E_2 low and E_2 high phonon modes of hexagonal ZnO, respectively. However, the characteristic 437 cm^{-1} peak, assigned to the non-polar E_2 optical phonon mode, appeared broadened. This was a first confirm of the deteriorated quality of the crystal structure of ZnO, due to the presence of the Mn dopant [2, 7, 8], as also confirmed from the XRD results previously discussed.

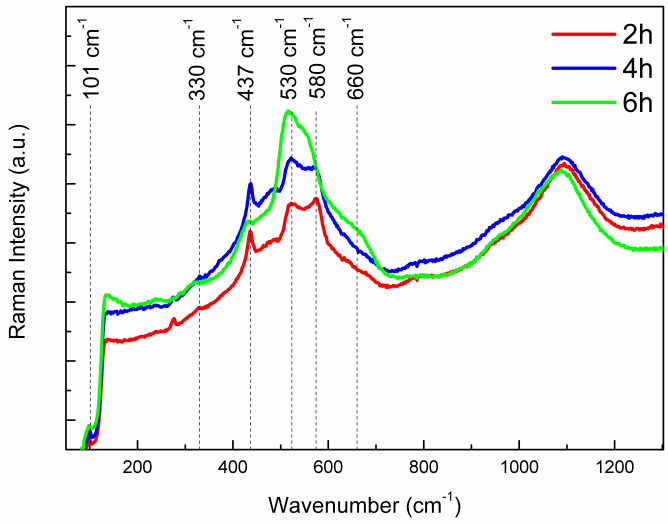

Figure 8.16. Raman spectra of Mn-doped sponge-like ZnO thin films, soaked at the different times of 2h, 4h, and 6h.

Another broadened peak was visible at about 330 cm^{-1}. In pure ZnO samples this peak is generally attributed to the second-order Raman processes, involving acoustic phonons [2, 7]. However, in the case of the Mn-doped samples, this peak was very weak. This is often observed for doped ZnO samples [2, 7, 8] independently of the kind of doping element, and is expected to be related to the deterioration of the ZnO crystal structure with doping. The literature also reports on the presence of the intense mode at about 530 cm^{-1} for many Mn-doped samples. This mode is a not-known mode of ZnO, and does not appear for other transition elements in ZnO [8]. Moreover, its intensity has been shown to increase with increasing Mn content [7]. This results was observed for the Mn-doped samples of this work (see Fig. 8.17), and thus believed to be an indication of the occured Mn substitution in the Zn sites, with the 530 cm^{-1} mode related to a local vibration involving the Mn atoms. The mode at about 580 cm^{-1}, present in all the analyzed samples (see Fig. 8.17), could be assigned to the disorder-increased $A_1(LO_1)$ mode, and to oxygen vacancies [7, 8]. The shift towards lower frequencies could be related to the fact that the substitution of the Mn into the Zn site introduced more defects and lattice distortions, because of the larger ionic radius of Mn^{2+} respect to that of Zn^{2+}. The vibrational mode at 660 cm^{-1} was ascribed to an intrinsic mode of ZnO, and assigned to the combination of transverse acoustic (TA) and longitudinal optical (LO) modes. The mode was enhanced in the case of Mn-doped ZnO, and should be related to the reinforcement of LO phonon scattering [2, 7].

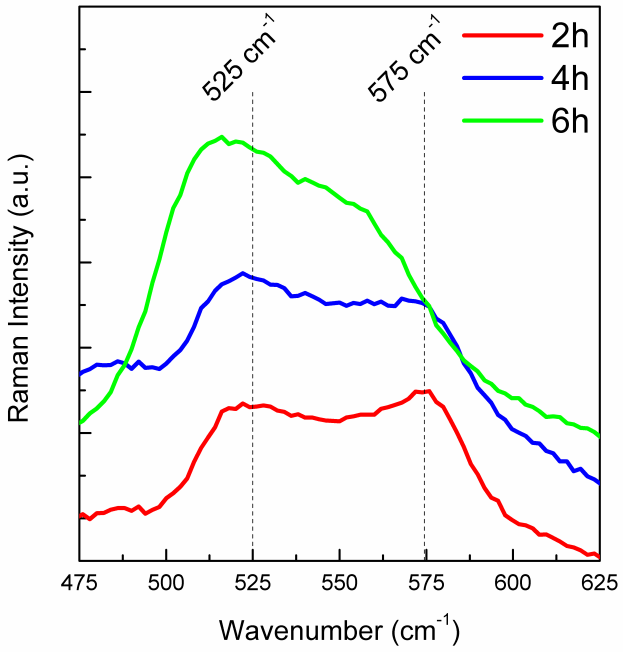

Figure 8.17. Particular of the Raman modes in the region 475 cm^{-1} - 625 cm^{-1} range, which presence was related to the occured Mn doping of ZnO.

8.2.3. Optical properties

Optical transmission spectra of the Mn-doped sponge-like ZnO films are shown in Fig. 8.18. All the samples exhibited an average reflectance of less than 20% in the visible region, indicating good optical quality of the deposited films.

From this first analysis, the Mn-doped samples appeared to be characterized by a higher optical transparency if compared with the undoped one, which showed an average reflectance of more than 40% in the lower part of the visible region, then decreasing up to around the 20% only at 700 nm. In the case of the doped samples, the average value of the reflectance was found to be maximum for sample Zn_Mn_2h and decreased with the increase of the Mn content, since the samples impregnated for 4h and 6h were characterized by a lower reflectance.

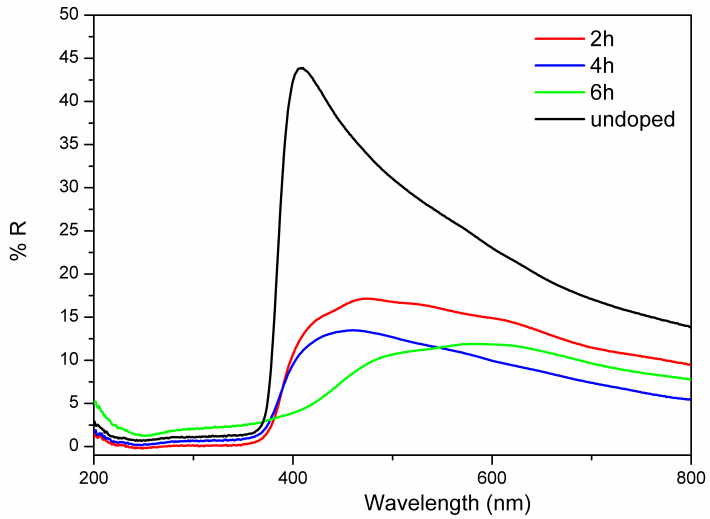

Figure 8.18. Optical absorbance of undoped and Mn-doped, sponge-like ZnO thin films.

The analysis of the diffused reflectance *F(R)* is reported in Fig. 8.19 for both the undoped and Mn-doped samples. The Kubelka–Munk function, *F(R)*, can be expressed as being:

$$F(R) = (1-R)\,2/2R = k/s$$

, where k is the molar absorption coefficient and s is the scattering coefficient. It is thus proportional to the absorbance of the analyzed sample. A higher absorbance in the visible region from 400 nm to 800 nm was thus observed for the doped samples in the visible range, with respect to the undoped one. The *F(R)* increased with the increase of the impregnation time, indeed sample Zn_Mn_2h had a lower absorbance with respect to sample Zn_Mn_4h. On the contrary, when the impregnation time was further increased up to 6h, a drop of the *F(R)* was revealed. This was expected, since the increase in the crystal defects induced by the doping process also implied a higher amount of light-scattering centers, thus decreasing the optical absorbance of the investigated material. The optical band gap (E_g) of the samples was calculated using the Tauc's method [9] from the *F(R)* spectra. According to this method, the plot of $[F(R)\cdot hv]^n$ against hv shows a linear region just above the optical absorption edge, where $n = 2$ is used for the direct allowed transition, $n = 1/2$ for the indirect allowed transition, and hv is the photon energy (eV). Both the experimental results and theoretical calculations suggest that the ZnO material has a direct forbidden gap [10]. Hence, in the Tauc plot shown in Fig. 8.20, $n = 2$ was employed, which clearly yields a satisfactory linearity for the undoped and Mn-doped ZnO samples. A slight decrease of the band gap energy was found for samples Zn_Mn_2h (3.28 eV) and Zn_Mn_4h (3.27 eV), respect to the undoped one (3.30 eV). By further

increasing the Mn content, a strong decrease of the band gap energy was then observed, changing from 3.30 eV of the undoped sample, to 2.96 eV for the 6h-impregnated doped film.

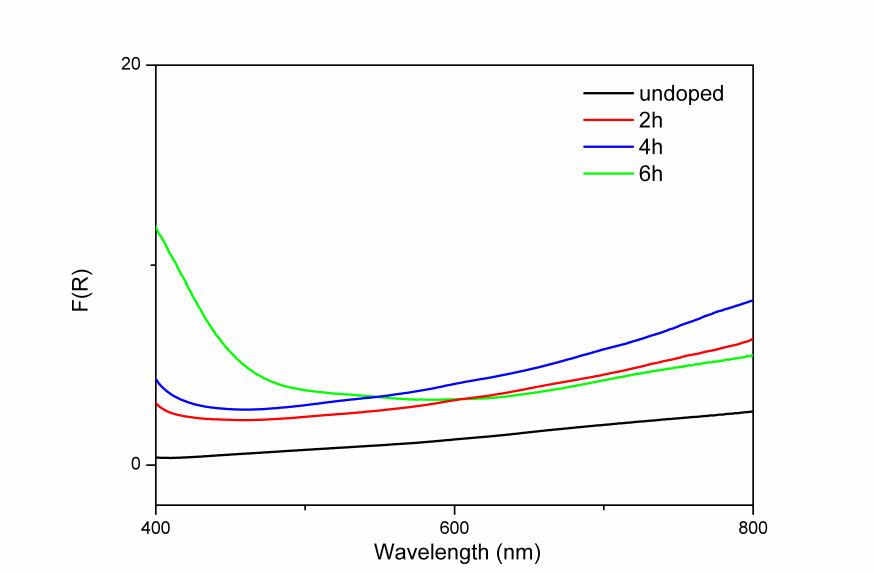

Figure 8.19. Diffuse reflectance *F(R)* spectra for the undoped sponge-like ZnO sample, and for the Mn-doped ZnO films, impregnated for 2h, 4h, and 6h.

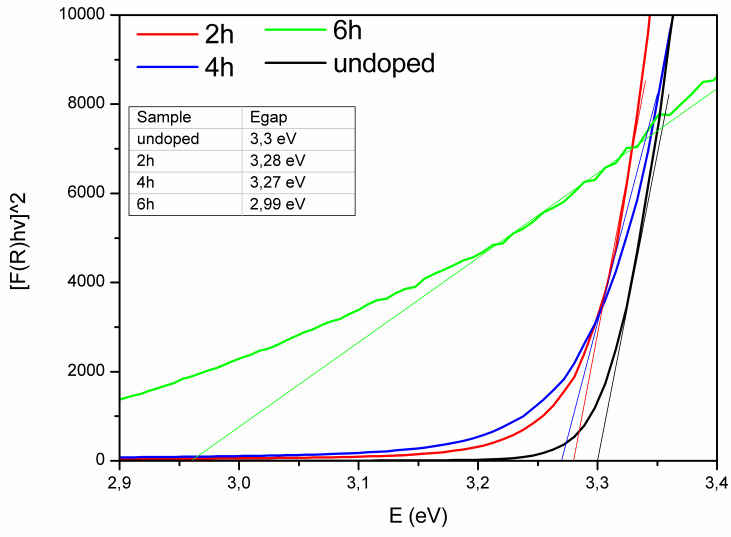

Figure 8.20. $[F(R)\cdot hv]^n$ vs. hv spectra for the undoped sponge-like ZnO sample, and for the Mn-doped ZnO films, impregnated for 2h, 4h, and 6h. The table inset shows the band gap energy values, estimated according to the Tauc's method.

8.2.4. Electrical and ferroelectric characterization

Electrical measurements were carried out on both the undoped and the Mn-doped sponge-like ZnO samples, in order to verify if any change in the I-V characteristics and in the polarization-voltage (P-E) loops were present before and after the introduction of the Mn dopants. Measurements were carried out by using a Piezo Evaluation System (PES, TFAnalyzer 2000HS, Aixacct) coupled to a single point laser vibrometer (Polytec OVF-505).

The I-V characteristics, together with the corresponding polarization curves for the Mn-doped ZnO films, impregnated for 2h, 4h, and 6h, are reported in Figs. 8.22, 8.23, and 8.24, respectively. As a comparison, the same measurements were performed on the undoped ZnO sample reference, and the obtained results are shown in Fig. 8.21.

All the doped samples showed the same electrical behavior. From each curve, a high resistive component, dominating the electrical behavior of the Mn-doped material, could be clearly observed. Indeed, I-V characteristics typical of a ohmic behavior can be underlined from Figs. 8.22(a), 8.23(a), and 8.24(a), independently of the impregnation time. The presence of high leakage currents, flowing inside the samples during the measurements, could also be stated. Depending on the electric field applied on the sample, these currents ranged between $15 \cdot 10^{-3}$ A and $60 \cdot 10^{-3}$ A.

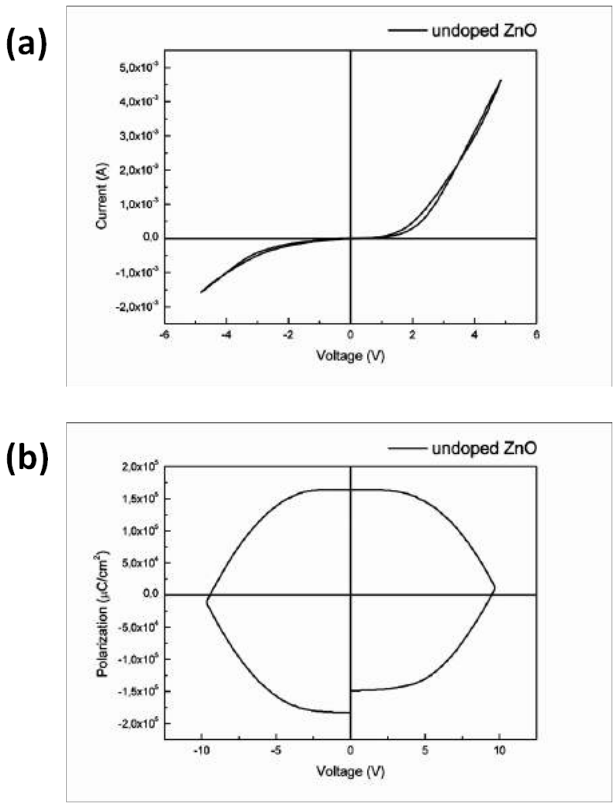

Figure 8.21. (a) I-V and (b) P-E curves of undoped, sponge-like ZnO film.

The I-V electrical characteristics of Mn-doped ZnO films strongly changed with respect to the one showed from the undoped reference sample, whose I-V characteristic is shown in Fig. 8.21(a). Without any doping, the electrical behavior of the sponge-like ZnO film was represented by a diode-like I-V characteristic, while from both the I-V and P-E measurements the absence of any ferroelectricity inside the sample was confirmed (see Fig. 8.21(b)). Since ZnO is a n-type semiconducting material, both resistive and capacitive contributions

are present, and the dominating one depends on the applied electric field. In the present case, both these contributions were revealed. The I-V response for the undoped sample was indeed different from the ideal case of a diode-like characteristic, with a non-zero current flowing inside the material also at electric fields lower than the threshold one.

The situation strongly changed for the Mn-doped samples. From the XPS analysis, only the presence of Mn^{2+} ions was observed. Mn^{2+} ions substituted Zn^{2+} ions with the same valence state. Thus, the introduced Mn dopants could not be able to compensate enough the intrinsic n-type conductivity of the undoped ZnO. Moreover, the doping process was demonstrated to lower the crystallinity of the samples, together with the formation of additional lattice defects. All these aspects probably contributed to an increase of the electrical conductivity of the Mn-doped samples, resulting in a higher predominance of the resistive contribution on the electrical response of the material. This was clearly visible from the I-V curves, which showed a linear characteristic typical of a resistive behavior.

From the P-E curves reported in Figs. 8.22(b), 8.23(b), and 8.24(b), no hysteresis loop were observed despite the introduction of the Mn dopant, which was expected to induce the presence of ferroelectricity. P-E curves were similar to the ones of the undoped ZnO sample.

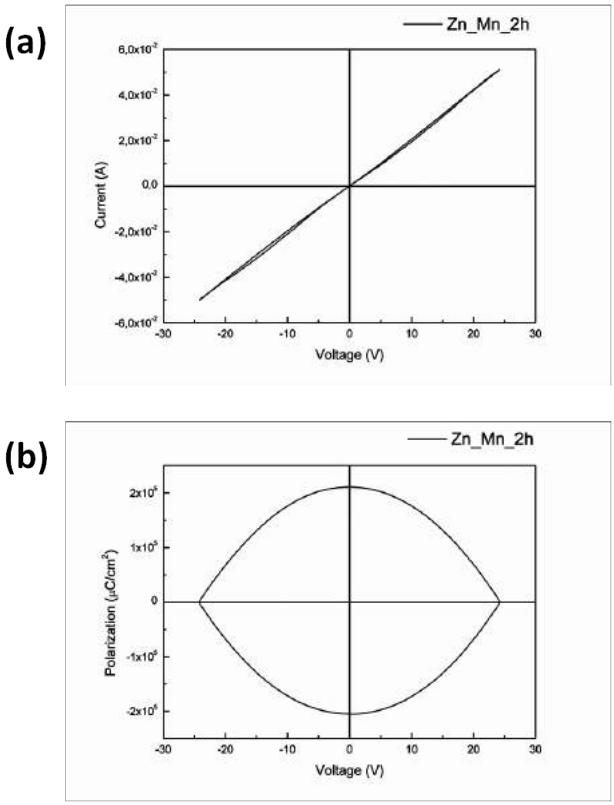

Figure 8.22. (a) I-V and (b) P-E curves of 2h Mn-doped, sponge-like ZnO film.

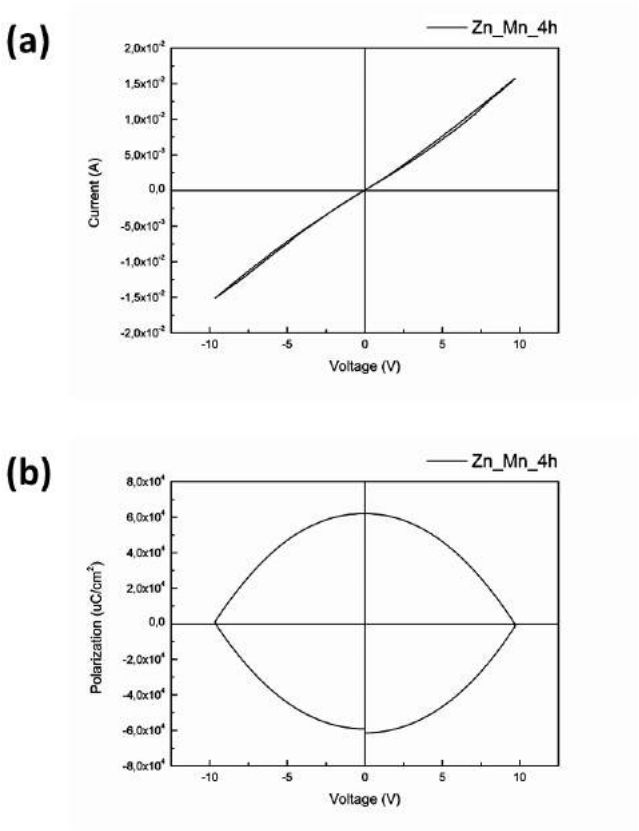

Figure 8.23. (a) I-V and (b) P-E curves of 4h Mn-doped, sponge-like ZnO film.

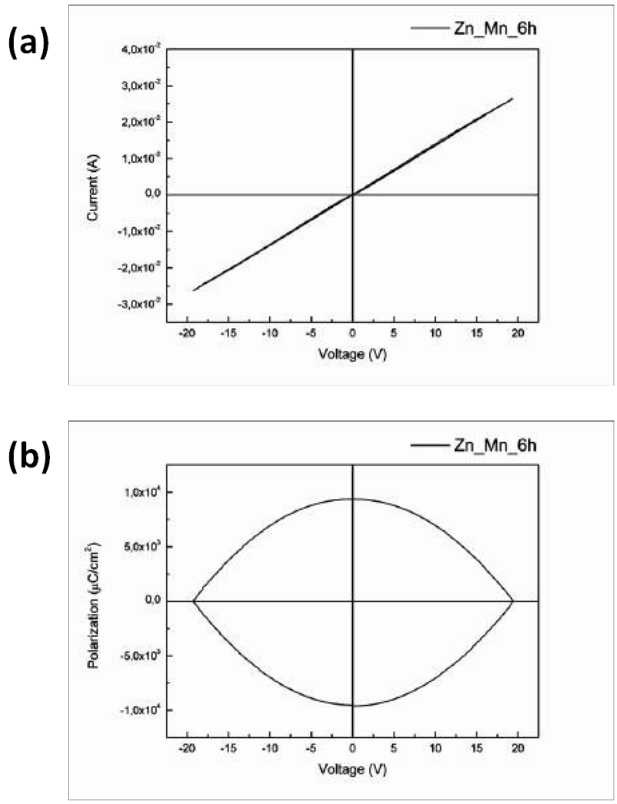

Figure 8.24. (a) I-V and (b) P-E curves of 6h Mn-doped, sponge-like ZnO film.

8.3. Analysis of Sb-doped sponge-like ZnO thin films

The aim of this Section is to present all the scientific results obtained from the characterization of sponge-like ZnO thin films doped with Sb. First, the morphology and the crystal structure of the samples are evaluated by means of Field Emission Scanning Electron Microscopy and X-Ray Diffraction, respectively. After that, the chemical composition analysis is carried out by two different spectroscopy techniques, the Energy Dispersive X-ray spectrometry and the X-ray Photoelectron Spectroscopy. The characterization of the vibrational properties is also considered, by performing Raman spectroscopy, while the optical properties are studied by UV-Vis measurements. In conclusion, the analysis of the electrical and ferroelectric behavior of the Sb-doped sponge-like ZnO films is discussed.

8.3.1. Morphological and structural characterization

The morphology and the average thickness of Sb-doped sponge-like ZnO samples were investigated using a Carl-Zeiss Dual Beam Auriga, consisting of a Field Emission Scanning Electron Microscope (FESEM) and Focused Ion Beam (FIB). The surface morphology of the analyzed samples grown on FTO/glass substrates is shown in Fig. 8.25, for each impregnation time. In all the cases, the sponge-like morphology previously observed for the starting metallic Zn film was still present, independently of the impregnation time and of the thermal treatment. Indeed, a surface characterized by the presence of elongated and branched nanostructures, forming a highly nanoporous network, was still present. Since also after the impregnation step and the thermal treatment, no substantial changes in the film morphology were observed, the non-destructive nature of the three-step process was demonstrated also for the Sb-doped ZnO samples.

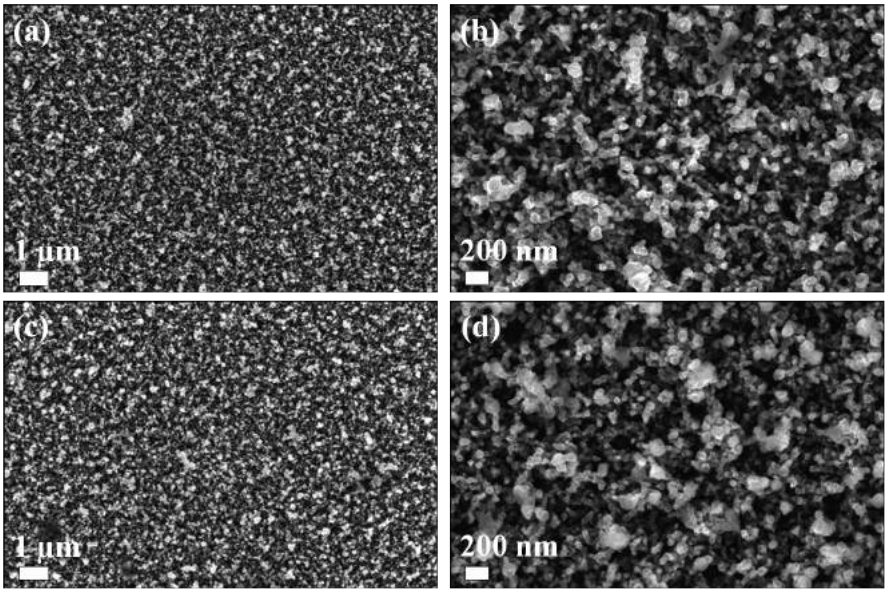

Figure 8.25. FESEM images showing the surface morphology of samples (a-b) Zn_Sb_2h, and (c-d) Zn_Sb_4h.

Fig. 8.26 shows the cross-sectional FESEM images acquired on the Sb-doped sponge-like ZnO films grown on ITO/glass substrates, and impregnated for 2h

(Fig. 8.26(a)) and 4h (Fig. 8.26(b)). The average thickness was estimated to be in the range of 1.1 μm – 1.2 μm, in each case. From this analysis, the presence of a uniform sponge-like nanostructure along the whole structure, from the surface up to the substrate, was demonstrated to be still present, despite the impregnation process performed at different times, and the subsequent thermal treatment. Moreover, the independence of the Sb-doped ZnO nanostructure from the particular kind of substrate was pointed out, as previously observed in the case of Mn-doping.

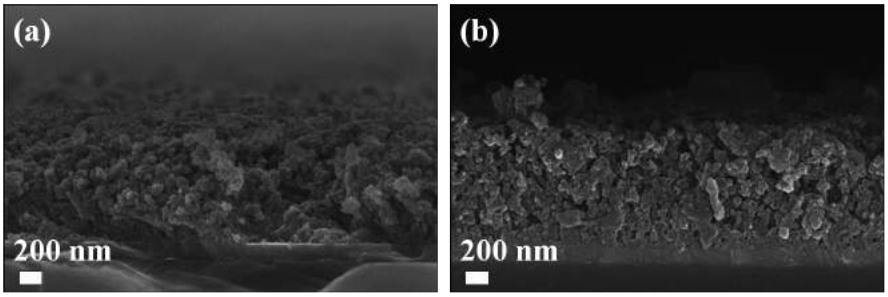

Figure 8.26. Cross-sectional FESEM images of samples (a) Zn_Sb_2h, and (b) Zn_Sb_4h.

The crystal structure and orientation of the Sb-doped, sponge-like ZnO samples grown on FTO/glass slides were analyzed by X-Ray Diffraction (XRD) measurements using a Panalytical X'Pert X-ray diffractometer in the Bragg-Brentano configuration. A Cu K_α monochromatic radiation was used as X-ray source, with a characteristic wavelength $\lambda = 1.54059$ Å.

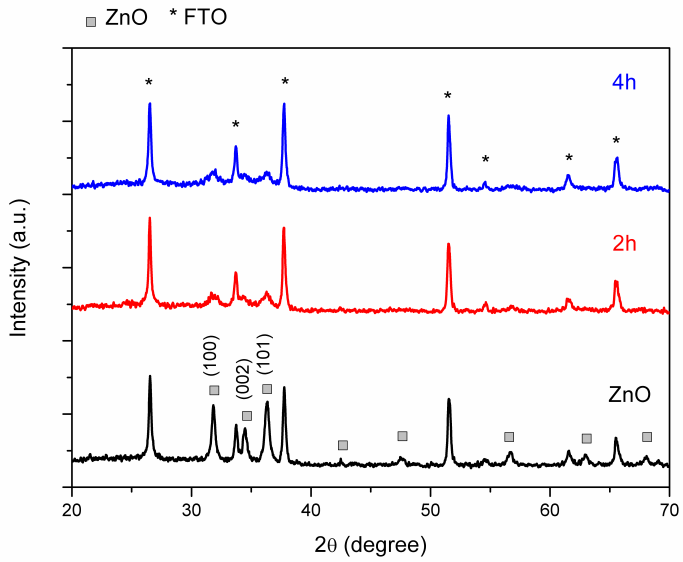

Figure 8.27. XRD pattern of samples Zn_Sb_2h (red line), and Zn_Sb_4h (blue line). As a comparison, the diffraction pattern of the undoped sponge-like ZnO film is also reported (black line). Peaks labeled by ∗ refer to the substrate diffraction contribution.

The XRD pattern acquired on the undoped sponge-like ZnO film, and on the Sb-doped samples Zn_Sb_2h and Zn_Sb_4h are reported in Fig. 8.27.

The undoped ZnO film revealed the presence of the hexagonal wurtzite-like crystal structure, already discussed in Chapter 7 for this kind of nanomaterial. The polycrystalline nature of the sponge-like ZnO film was underlined by the presence of multiple diffraction peaks related to the ZnO (100), ZnO (002), and ZnO (101) crystal planes. From the analysis of the patterns collected for the Sb-doped samples, diffraction contributions coming from the same crystal planes could be also confirmed. Despite the presence of the dopant, each ZnO sample was thus characterized by the same hexagonal crystal structure, without showing any diffraction contribution which could be generated from secondary Sb metallic or oxide phases, suggesting that the most Sb atoms were in the ZnO wurtzite lattice [11, 12].

	Peak position		
Sample	ZnO (100)	ZnO (002)	ZnO (101)
Undoped ZnO	31.83°	34.43°	36.31°
ZnO_Sb_2h	31.71°	34.41°	36.29°
ZnO_Sb_4h	31.65°	34.37°	36.29°

Table 8.4. Diffraction peak positions detected for undoped and Sb-doped sponge-like ZnO films.

To deeply investigate the effect of Sb doping on the crystallinity of the sponge-like ZnO films, the intensity and position of the (100), (002), and (101) diffraction peaks were considered and the corresponding diffraction peaks are shown in Figs. 8.28 and 8.29, while the peak positions for the Sb-doped samples are summarized in Table 8.4. The presence of Sb dopant in ZnO resulted in remarkable shift to lower angles [13] and each diffraction peak appeared to be broadened if compared to the corresponding one detected from the undoped sample (see Figs. 8.28 and 8.29). All these aspects were in good agreement with the literature [13, 11, 14, 12], suggesting the occured Sb substitution in the Zn sites of the host ZnO crystal structure [14].

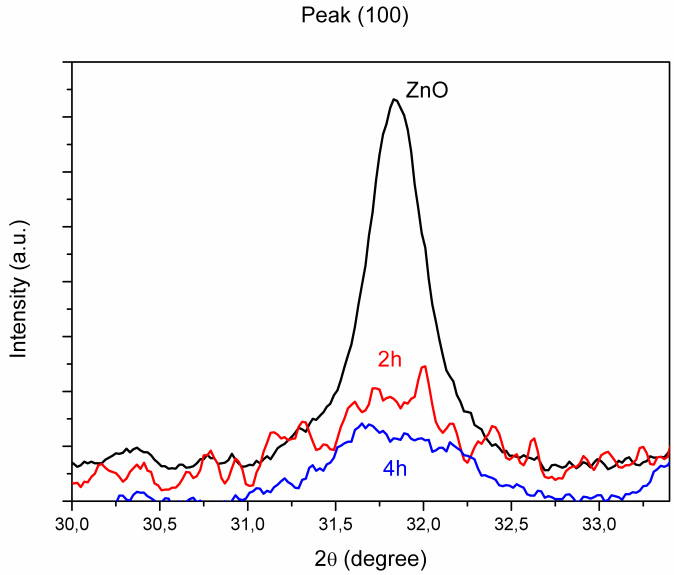

Figure 8.28. Particular of the ZnO (100) diffraction peak detected for the undoped and Sb-doped ZnO films, impregnated for 2h and 4h.

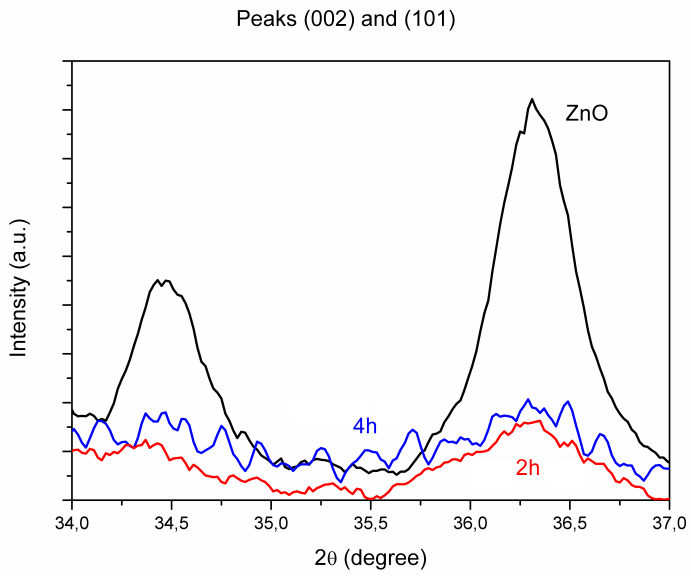

Figure 8.29. Particular of the ZnO (002) and ZnO (101) diffraction peaks of the undoped and Sb-doped, sponge-like ZnO thin films, impregnated for 2h and 4h.

8.3.2. Chemical composition analysis and vibrational properties

The chemical composition of Sb-doped ZnO films was first evaluated by means of EDX measurements, carried out by a Oxford Instruments X-Max 50 mm^2 Silicon Drift Detector (SDD) for EDX analysis, coupled to the previously described FESEM set-up.

The EDX spectrometry evaluated on the samples impregnated for 2h and 4h is reported in Fig. 8.30, together with the corresponding area of the sample on which the EDX measure was carried out. The detected chemical elements in each samples were oxygen, zinc, and antimony, confirming the presence of the Sb dopant in both the cases.

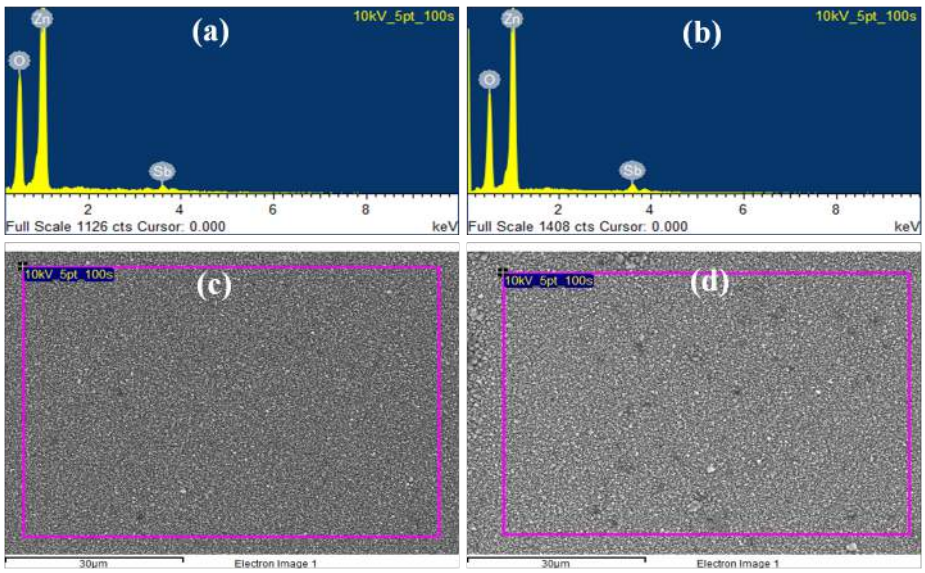

Figure 8.30. EDX spectrometry of samples Zn_Sb_2h (a) and (c); and Zn_Sb_4h (b) and (d).

From the quantitative analysis summarized in Table 8.5, an increase of the Sb content with the increase of the impregnation time was observed, with the highest amount of the Sb dopant (3.82 atomic %) observed for the sample impregnated for the longest time (4h). Since the thermal treatment and the solution concentration were the same for all the impregnated samples, the reason of this difference should be ascribed to the different soaking time used during the impregnation step. Together with the increase of the Sb content with increasing the impregnation time, a decrease of the Zn content could be also observed. In the case of 2h of impregnation, the Zn atomic percentage was estimated to be 44.40%, but slightly decreased to 40.92 % when the impregnation time was increased up to 4h. When a higher amount of the Sb dopant is present, the number of potential substitutional mechanisms of Sb ions into the Zn sites of the host ZnO crystal structure is expected to be higher too, and a higher amount of Zn sites is replaced by Sb ions. This was considered the reason why the Zn atomic percentage decreased with the increase of the impregnation time.

Element	Impregnation time	Atomic %
O K	2h	53.66
	4h	55.26
Zn L	2h	44.40
	4h	40.92
Sb L	2h	1.94
	4h	3.82

Table 8.5. Atomic percentage of the chemical elements detected by EDX spectrometry in the Sb-doped ZnO samples.

Since a quantitative evaluation of the doping content and stoichiometry could not be exactly carried out by EDX measurements, X-ray Photoelectron Spectroscopy (XPS) analysis was performed on the Sb-doped sponge-like ZnO films. With this kind of analysis, it was possible to study the presence and the content of the dopant in the samples, its chemical state and, in particular, the chemical bonds involving the doping element.

XPS measurements were carried out by using a PHI 5000 VersaProbe (Physical Electronics) system, equipped with an Ar^+ gun, in order to remove any contaminant or pollutant from the surface of the analyzed material. The X-ray source was a Al K_α radiation.

Figs. 8.31 and 8.32 show the survey XPS spectra acquired on the Sb-doped samples impregnated for 2h and 4h. For each of the two samples, the chemical elements detected were carbon, oxygen, antimony, and zinc. Table 8.6 summarizes the atomic percentage values estimated for each of the detected chemical elements. The reason for a so-high amount of C into the analyzed samples was previously discussed for the Mn-doped ZnO films.

From the XPS compositional analysis, the presence of the Sb was confirmed for each sample, and its atomic percentage increased with the increase of the impregnation time, according to EDX results. It was of 12.90% for the sample impregnated for 2h, then increased up to 17.59% for the sample impregnated for 4h. Contemporary to the increase of the Sb content, the Zn atomic percentage was reported to be lower for the sample impregnated for the longest time (4h), changing from 6.00% up to 3.69%. The decrease of the Zn content as the Sb content increased was thus underlined, confirming the EDX analysis. Moreover, this behavior was already reported in the case of the Mn-doped ZnO samples (see Section 8.2.2).

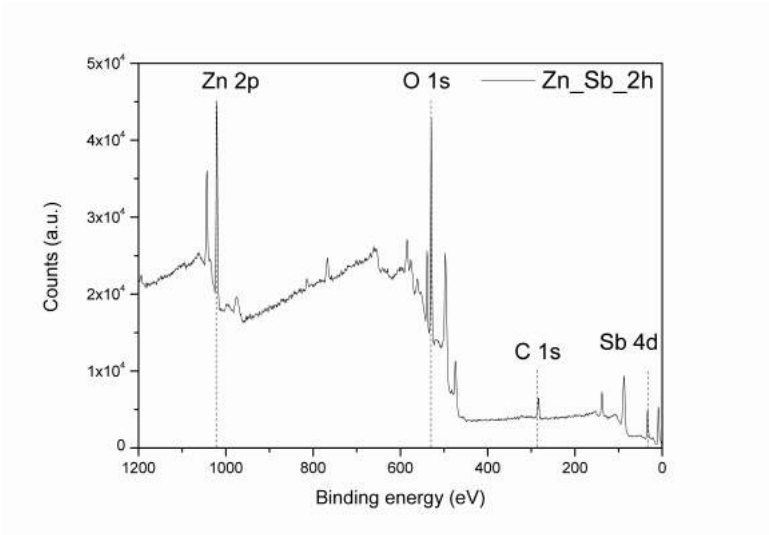

Figure 8.31. Survey XPS pattern of sample Zn_Sb_2h.

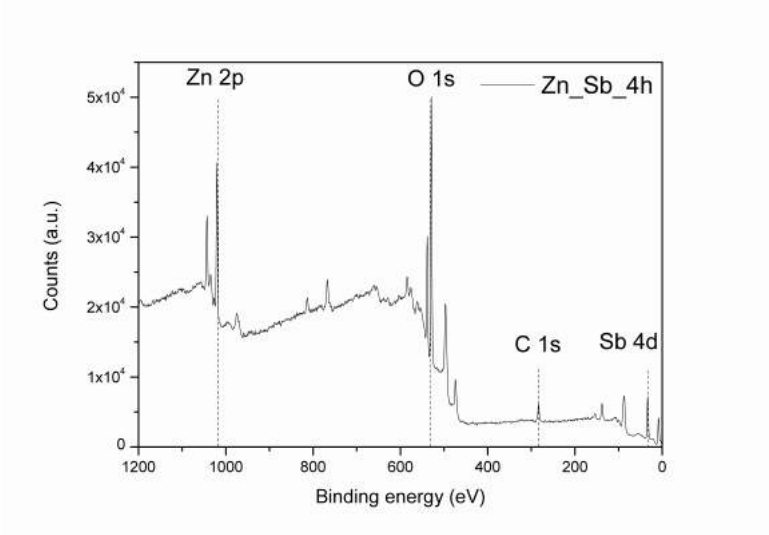

Figure 8.32. Survey XPS pattern of sample Zn_Sb_4h.

Sample	Element	Atomic %
Zn_Sb_2h	C_{1s}	18.60
	O_{1s}	62.50
	Zn_{2p}	6.00
	Sb_{4d}	12.90
Zn_Sb_4h	C_{1s}	15.06
	O_{1s}	63.67
	Zn_{2p}	3.69
	Sb_{4d}	17.59

Table 8.6. Atomic percentage of the chemical elements detected by XPS in the Sb-doped ZnO samples.

High-resolution (HR) measurements, related to the contribution of the O_{1s}, Sb_{4d}, and Zn_{2p} core-electrons, were carried out in order to establish the chemical bonds involving oxygen, zinc, and antimony atoms. These are shown in Figs. 8.33, 8.35 and 8.34, respectively.

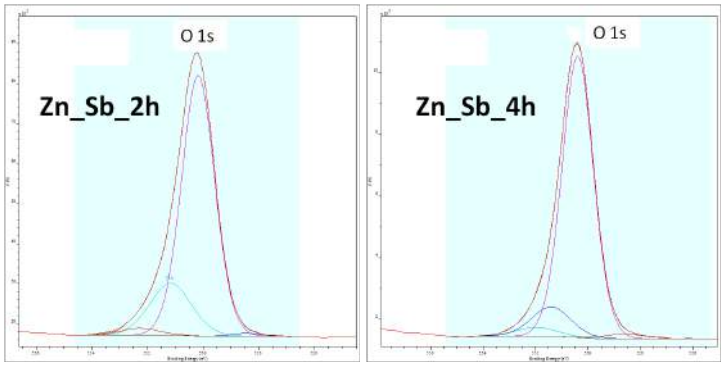

Figure 8.33. HR O_{1s} XPS spectra of samples Zn_Sb_2h and Zn_Sb_4h.

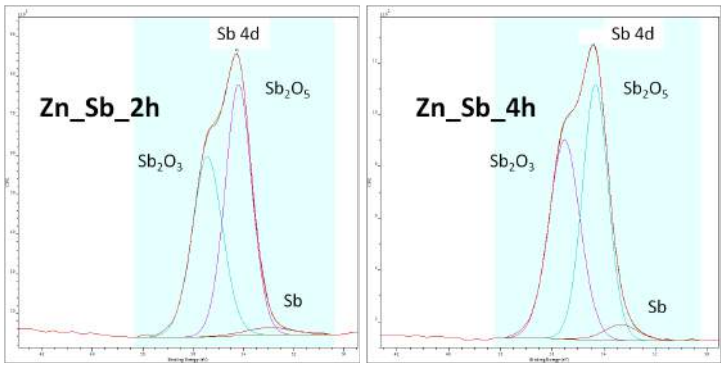

Figure 8.34. HR Sb_{4d} XPS spectra of samples Zn_Sb_2h and Zn_Sb_4h.

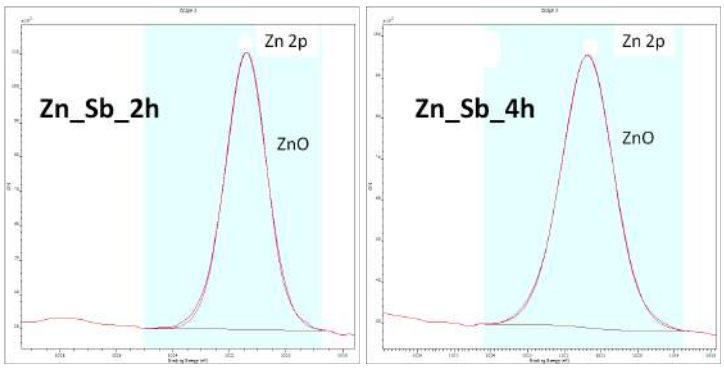

Figure 8.35. HR Zn_{2p} XPS spectra of samples Zn_Sb_2h and Zn_Sb_4h.

From Fig. 8.33, the presence of O-Zn and O-Sb chemical bonds was first observed, being represented by the peaks centered at the binding energy values of 530.2 eV and 532.3 eV, respectively. The presence of Sb and the nature of the chemical bonds involving the Sb ions were further analyzed by fitting the

HR Sb_{4d} XPS spectra for both the Zn_Sb_2h and Zn_Sb_4h samples. From this analysis, the presence of three main peaks was observed. The strongest ones were centered at 34.2 eV and 35.4 eV, and ascribed to the presence of Sb-O chemical bonds in Sb_2O_3 and Sb_2O_5, respectively. The presence of these peaks was reported to be representative of Sb^{3+} and Sb^{5+} species [15]. A third, weaker peak, and centered at 33.3 eV was also observed. The origin of this peak is reported to be related to the presence of Sb^0 species [15].

The vibrational properties of Sb-doped ZnO thin films were investigated by means of Raman spectroscopy measurements, using a Renishaw inVia Reflex (Renishaw PLC, UK) micro-Raman spectrophotometer equipped with a cooled CCD camera. Samples were excited with an Ar - Kr laser source with λ = 514.5 nm. Raman spectroscopy of the samples Zn_Sb_2h and Zn_Sb_4h are reported in Fig. 8.36.

Raman scattering is considered to be the most powerful nondestructive technique to study the crystalline quality, being sensitive to structural disorder, and defects in micro- and nanostructures. In the present case, it can give important information about the local structural changes due to the incorporation of Sb^{3+} and Sb^{5+} ions into the host ZnO lattice. According to group theory, ZnO belongs to $C_{6\nu}^4$ and is characterized by eight sets of optical phonon modes. A_1 + E_1 + $2E_2$ are classified as Raman active modes, $2B_1$ are Raman silent mode while A_1 + E_1 are IR active modes, which split into the LO and TO components [16]. The Sb-doped ZnO exhibited a broad band between 500 cm^{-1} and 600 cm^{-1}, in agreement with already reported in the literature [17]. Most likely, this band was due to Sb-related in-band modes that were coupled to the longitudinal optical phonon modes of the host ZnO lattice. Indeed, Sb–O compounds with fivefold coordinated Sb atoms show vibrational frequencies in this range [17].

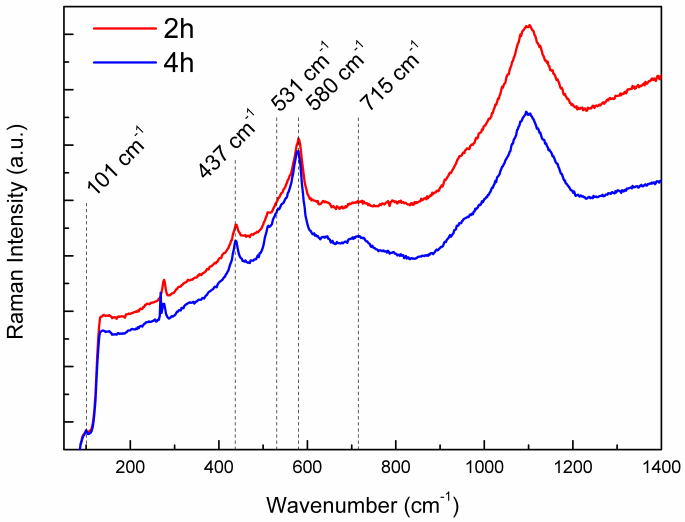

Figure 8.36. Raman spectra of Sb-doped sponge-like ZnO films.

A more accurate analysis of the Raman spectra is reported in Fig. 8.37. Additional/local vibrational modes were found in the analysis of Sb-doped ZnO films, such as the mode at 531 cm^{-1}. The appearance of this component was already reported for Sb doping in ZnO [18]. However, it is worth noting that this conclusion came from the comparison of specific dopants (Fe, Sb, Al, Ga) in Raman spectra, and it was concluded that, since the 531 cm^{-1} was present only for the Sb-doped samples, it was characteristic of Sb doping. The origin

of this mode was attributed from Manjon et al. [19] to the additional or local vibrational modes due to the breakdown of the translation symmetry of the lattice caused by defects or impurities (the doping element in the present case). The mode at about 580 cm^{-1}, detected in the spectra of both samples, was also measured for the Mn-doped ZnO samples, previously described in Section 8.2.2, and could be assigned to the disorder-increased $A_1(LO_1)$ mode, and to oxygen vacancies as well [11, 12, 14]. A further mode at around 715 cm^{-1} confirmed the presence of Sb ions in the ZnO lattice, corresponding to Sb-O-Sb stretching [20].

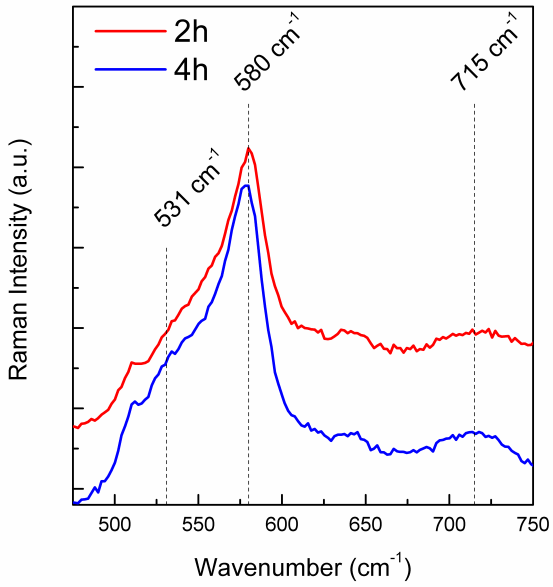

Figure 8.37. Particular of the Raman modes in the region 475 cm^{-1} - 750 cm^{-1} range, which presence was related to the occured Sb doping of ZnO.

8.3.3. Optical properties

Fig. 8.38 shows the optical absorbance spectra of undoped and Sb-doped sponge-like ZnO thin films. The absorbance of the undoped sample was higher with respect to the doped ones, which in turn showed and average absorbance ranging from 15% to 5% in the visible range.

Since the optical properties of a material are determined both from the reflectance (R), absorbance (A), and transmittance (T), by the relation R = 1 - T - A, also the diffused reflectance F(R), proportional to the absorbance, was estimated both for the undoped and Sb-doped samples, and the corresponding results are shown in Fig. 8.39. It is shown that a higher absorbance was reported for the Sb-doped samples, slightly decreasing with the increase of the impregnation time.

From the *F(R)* curves, the estimation of the energy band gap E_g was also possible (see Fig. 8.40), according to the Tauc's method [9]. It generally decreased from the 3.30 eV of the undoped sample, up to 3.25 eV and 3.24 eV for the 2h-impregnated and 4h-impregnated Sb-doped films. The decrease in the band gap energy could be ascribed to the introduction of additional shallow donors energy states in the ZnO band structure, following the introduction of Sb dopants [14].

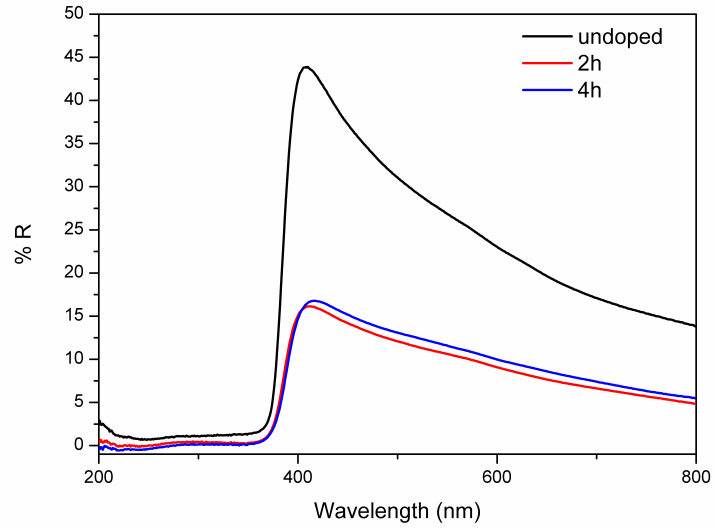

Figure 8.38. Optical absorbance of undoped and Sb-doped, sponge-like ZnO thin films.

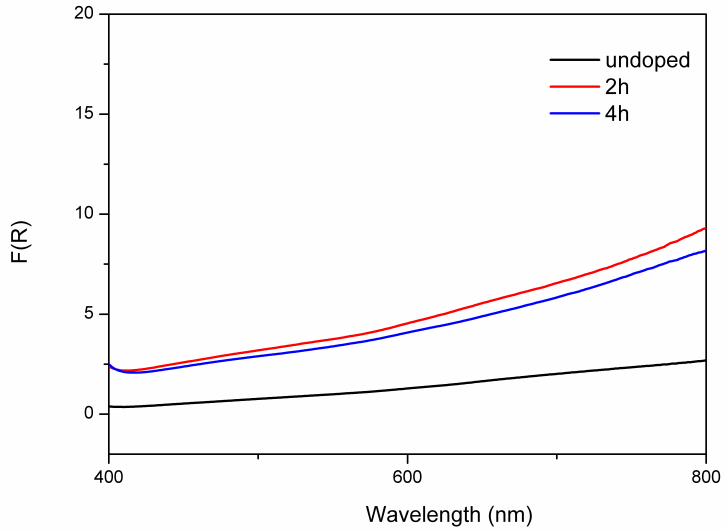

Figure 8.39. Diffused reflectance spectra estimated for the undoped sponge-like ZnO sample, and for the Sb-doped ZnO films, impregnated for 2h and 4h.

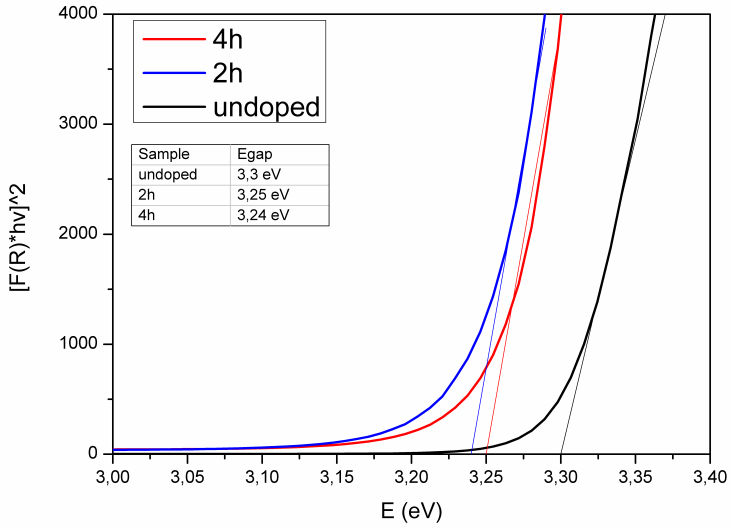

Figure 8.40. $[F(R)\cdot hv]^n$ vs. hv spectra for the undoped sponge-like ZnO sample, and for the Sb-doped ZnO films, impregnated for 2h and 4h. The inset table shows the band gap energy values, estimated according to the Tauc's method.

8.3.4. Electrical and ferroelectric characterization

Electrical measurements were carried out on both the undoped and the Sb-doped sponge-like ZnO samples, in order to verify if any change in the I-V characteristics and in the P-E loops were present before and after the introduction of the Sb dopants. Measurements were carried out by using the Piezo Evaluation System already described in Section 8.2.4.

Figs. 8.41(a) and 8.41(b) show the I-V and P-E characteristics of the undoped sponge-like ZnO film. They were already discussed in Section 8.2.4. A typical diode-like characteristic was revealed in this case, and no hysteresis phenomena were observed in both the I-V and P-E curves, confirming the absence of any ferroelectric behavior.

The situation strongly changed after the insertion of the Sb dopants. Figs. 8.42 and 8.44 show the I-V characteristics for the Sb-doped ZnO samples, impregnated for 2h and 4h. In each figure, panel (a) refers to the I-V measurements obtained by a single-loop measure (a), while panel (b) shows the same measure repeated for three cycles. In all the Sb-doped samples, the appearance of switching phenomena in the current flowing through the samples occured, with typical current ranges being in the order of 10^{-9} A, confirming the high insulating characteristic of Sb-doped ZnO samples with respect to the Mn-doped ones and to the undoped sample. The shape of the I-V characteristics was quite different from the one generally observed in literature for well-known ferroelectric materials. However, these differences could be ascribed to the following aspects. Asymmetries in the I-V shapes were present mainly because of the use of two different electrode materials, Pt for the top electrode and Indium-Tin-Oxide for the bottom one, which induced an asymmetrical response when the bias voltage changed from positive to negative values. These two materials are indeed characterized by different working functions, which affected the final electrical response of the material. A low but still not negligible resistive component was also found, inducing leakage current contributions and being represented by the presence of current peaks occurring at bias voltages lower than the maximum values.

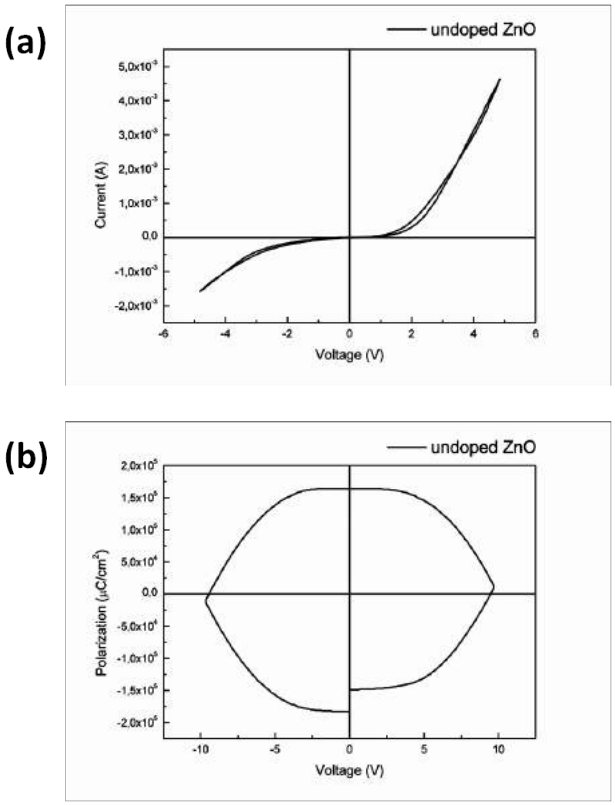

Figure 8.41. (a) I-V and (b) P-E curves of undoped, sponge-like ZnO film.

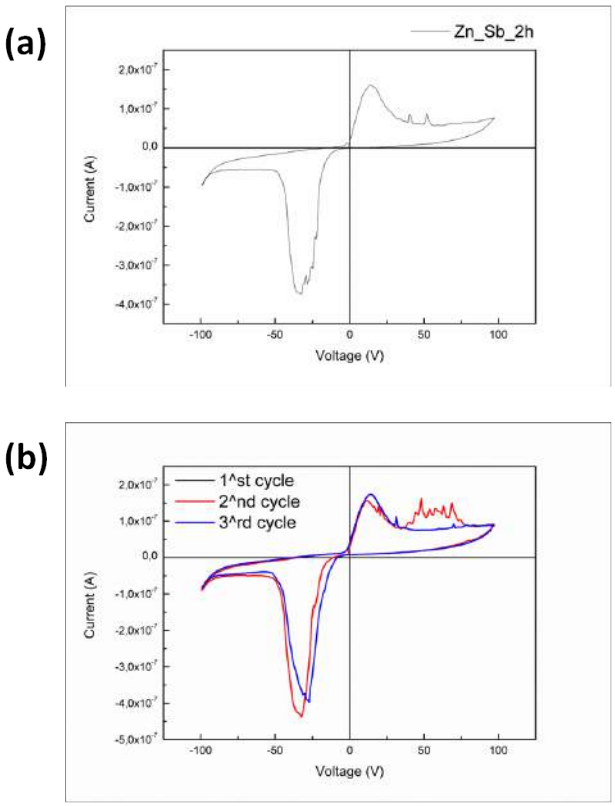

Figure 8.42. I-V curves of sample Zn_Sb_2h: (a) single-loop, and (b) for three cycles.

The presence of leakage phenomena could also be denoted by the I-V characteristics where, for the maximum values of the bias voltage, the current increased considerably. If no leakage current were present, it would remain constant. In particular, for the sample impregnated for 4h, higher leakage current effects were observed, since the peaks corresponding to leakage phenomena were more intense and pronounced with respect to the 2h impregnated sample. This aspect is better visible by comparing Figs. 8.42(b) and 8.44(b). The presence of a higher leakage component could be ascribed to the presence of different Sb ionic states, i.e., Sb^0, Sb^{3+} and Sb^{5+}, already confirmed by the XPS analysis described previously.

Closed-loop, hysteretical P-E curves were observed for both the Sb-doped samples, which are shown in Figs. 8.43 and 8.45. From the comparison of both I-V and P-E curves, the formation of ferroelectric domains into the Sb-doped ZnO films could thus be supposed to exist. In particular the switching of these domains could be considered as the origin of the switching phenomena observed in the I-V curves, and of the hysteretical loop shown from the electrical polarization of the analyzed samples.

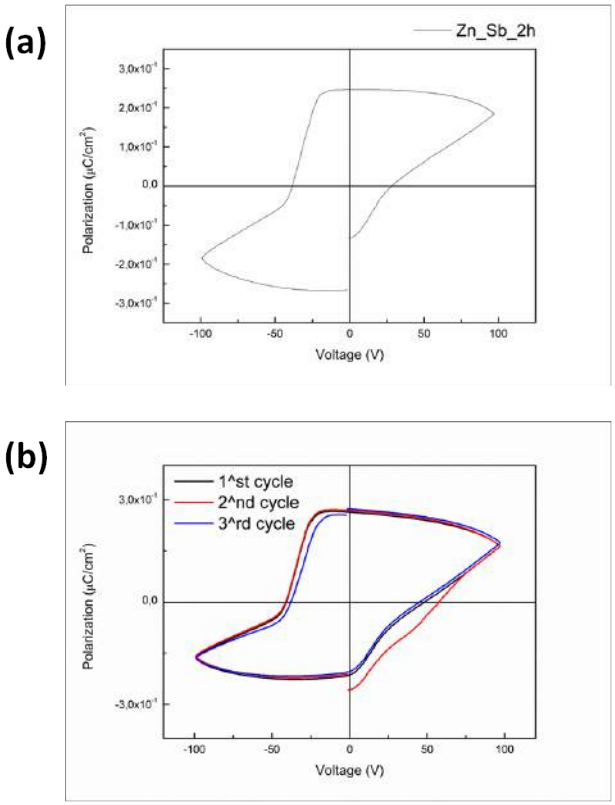

Figure 8.43. P-E curves of sample Zn_Sb_2h: (a) single-loop, and (b) for three cycles.

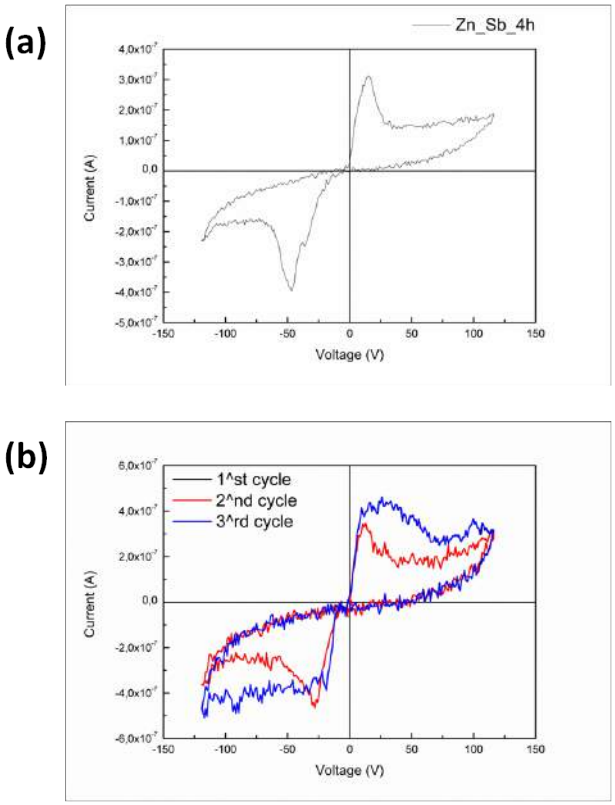

Figure 8.44. I-V curves of sample Zn_Sb_4h: (a) single-loop, and (b) for three cycles.

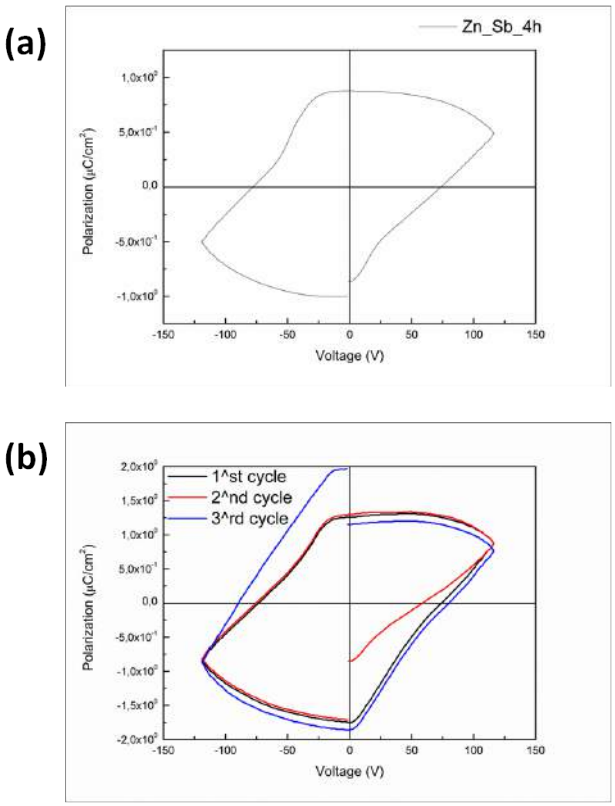

Figure 8.45. P-E curves of sample Zn_Sb_4h: (a) single-loop, and (b) for three cycles.

8.4. Conclusions

In this chapter a detailed analysis on the properties of Mn-doped and Sb-doped sponge-like ZnO thin films deposited on conductive glass substrates was presented and properly discussed. Doped ZnO thin films with a porous nanostructure were successfully synthesized with a simple three-step method. The first step concerned on the deposition of metallic Zn films with the RF magnetron sputtering technique. The resulting films, widely described in Chapter 7, provided a highly active surface area characterized by the presence of a nanoporous network. This aspect was fully exploited in the second step of the synthesis method, when the nanoporous Zn films were impregnated for different impregnation times by two different liquid solutions, providing the desired doping elements. Manganese and antimony were selected for this purpose. After the impregnation step, the samples were subjected to a thermal treatment, performed in ambient air, with the manifold aim of oxidizing the Zn network, obtaining the full conversion of the starting metallic film into ZnO, and at the same time to promote the diffusion and the insertion of the Mn and Sb doping agents into the ZnO crystal lattice.

The morphological characterization confirmed the presence of a porous network on both Mn- and Sb- doped ZnO films, underlining the non-destructive nature of the method followed for the synthesis of the analyzed materials. Energy Dispersive X-ray spectroscopy and X-ray Photoelectron Spectroscopy confirmed the presence of the doping elements in all the samples, and highlighted the increase of the dopant content with the increase of the impregnation time. From the XPS analysis also the nature of the chemical bonds involving the doping elements could be determined, confirming that the detected dopants did not form any secondary metallic or oxide phases, but completely participated into the doping process of ZnO. This last aspect was further confirmed by the X-ray diffraction analysis, which also highlighted the deterioration of the hexagonal crystal structure with respect to the undoped ZnO sample. The presence of the dopant elements into the crystal structure of ZnO, together with a degradation of the crystal lattice, was further assessed through Raman spectroscopy, which evidenced the presence of vibrational modes typical of Mn- and Sb- doped ZnO nanomaterials. The introduction of substitutional dopants into the ZnO lattice is expected to distort the crystal cell, which should in turn result into the appearance of ferroelectricity, that is not normally observed in undoped ZnO. This last aspect was properly analyzed by electrical measurements on undoped, Mn-doped and Sb-doped sponge-like ZnO films. Results confirmed the absence of ferroelectrcity in the undoped ZnO sample, which showed its typical capacitor-like behavior. In the case of the Mn-doped samples, a change in the electrical behavior was also observed, but no ferroelectric phenomena were pointed out. Conversely, a high resistance contribution was highlighted in the I-V response, being represented by linear characteristics and high current range regimes, which were in the range of mA. Strikingly, typical ferroelectric switching phenomena in the I-V characteristics were instead observed in Sb-doped ZnO films, which also showed the presence of hysteretical polarization loops, with residual polarizations at zero bias voltage.

Bibliography

[1] J. B. Wang, G. J. Huang, X. L. Zhong, L. Z. sun, Y. C. Zhou, and E. H. Liu, *Appl. Phys. Lett.* **88** (2006) 252502.

[2] S. Guo, Z. Du, and S. Dai, *Phys. Status Solidi B* **246** (2009) 2329-2332.

[3] H. K. Yadav, K. Sreenivas, R. S. Katiyar, and V. Gupta, *J. Phys. D: Appl. Phys.* **40** (2007) 6006.

[4] J. T. Luo, X. Y. Zhu, G. Chen, F. Zeng, and F. Pan, *Phys. Status Solidi R* **4** (2010) 209-211.

[5] J. Wang, W. Chen, and M. Wang, *J. Alloy Compd.* **449** (2008) 44-47.

[6] Y. Guo, X. Cao, X. Lan, C. Zhao, X. Xue, and Y. Song, *J. Phys. Chem. C* **112** (2008) 8832-8838.

[7] J. B. Wang, G. J. Huang, X. L. Zhong, L. Z. Sun, Y. C. Zhou, and E. H. Liu, *Appl. Phys. Lett.* **88** (2006) 252502.

[8] H. K. Yadav, K Sreenivas, R S Katiyar, and Vinay Gupta, *J. Phys. D: Appl. Phys.* **40** (2007) 6007-6009.

[9] K. Madhusudan Reddy, Sunkara V. Manorama, and A. Ramachandra Reddy, *Mater. Chem. Phys.* **78** (2002) 239-245.

[10] A. Segura, J. A. Sans, F. J. Manjón, A. Muñoz, and M. J. Herrera- Cabrera, *Appl. Phys. Lett.* **83** (2003) 278-280.

[11] O. Lupan, L. Chow, L. K. Ono, B. R. Cuenya, G. Chai, H. Khallaf, S. Park, and A. Schulte, *J. Phys. Chem. C* **114** (2010) 12401-12408.

[12] Sushil K. Pandey, Saurabh K. Pandey, V. Awasthi, A. Kumar, U. P. Deshpande, M. Gupta, and S. Mukherjee, *Appl. Phys. Lett.* **114** (2013) 163107.

[13] Y. Yang, J. Qi, Q. Liao, Y. Zhang, L. Tang, and Z. Qin, *J. Phys. Chem. C* **112** (2008) 17916-17919.

[14] K. Samanta, P. Bhattacharya, and R. S. Katiyar, *Appl. Phys. Lett.* **108** (2010) 113501.

[15] R. Reiche, J. P. Holgado, F. Yubero, J. P. Espinos, and A. R. Gonzalez-Elipe, *Surf. Interface Anal.* **32** (2003) 256-262.

[16] K.A. Alim, V.A. Fonoberov, M. Shamsa, and A.A. Balandin, *J. Appl. Phys.* **97** (2005) 124313.

[17] F. Friedrich, I. Sieber, C. Klimm, M. Klaus, Ch. Genzel and N. H. Nickel, *Appl. Phys. Lett.* **98** (2011) 131902.

[18] C. Bundesmann, N. Ashkenov, M. Schubert, D. Spemann, T. Butz, E. M. Kaidashev, M. Lorenz, and M. Grundmann, *Appl. Phys. Lett.* **83** (2003) 1974.

[19] F. J. Manjón, B. Marí, J. Serrano, A. H. Romero, *J. Appl. Phys.* **97** (2005) 053516.

[20] B.S. Naidu, M. Pandey, V. Sudarsan, R.K. Vatsa, and R. Tewari, *Chem. Phys. Lett.* **474** (2009) 180-184.

Chapter 9

Conclusions

In this thesis, the sputter deposition and characterization of ZnO nanomaterials both in the form of dense and sponge-like thin films is reported and described. It is shown that high-quality ZnO thin films can be successfully grown on both hard and flexible conductive substrates, with the final aim of proving that their piezoelectric and electrical properties can be successfully exploited in the fabrication of piezoelectric-based nanosensors and nanoactuators.

Dense ZnO thin films were first deposited on Si substrates by the RF magnetron sputtering technique. The morphology and crystal structure of the resulting samples was analyzed by means of FESEM and XRD measurements, while the chemical composition and stoichiometry of two different samples grown in different sputtering atmospheres were evaluated by XPS. On the basis of the characterization results, suitable deposition parameters were selected, in order to deposit high quality ZnO thin films, with a proper surface morphology, a *c*-axis oriented crystal structure, and the right stoichiometry. After this, hard and flexible conductive substrates were considered, and ZnO thin films with different thicknesses were deposited according to the set of the deposition parameters selected previously. The as-deposited films were characterized in terms of their morphology and crystal structure, just to check the quality of the samples. Then the piezoelectric behavior of ZnO films was analyzed by means of PFM and piezoelectric voltage generation measurements. Results showed that all the ZnO films are characterized by a good piezoelectric response, with a d_{33} piezoelectric coefficient value in agreement with those reported in literature, achieving a maximum value of 8.7 pmV^{-1} for the thickest sample. Also piezoelectric output voltage measurements conducted on the flexible structures pointed out a good response from all the samples, with a maximum output voltage of 0.746 V obtained for the thickest film. All these results encourage in exploiting and using dense ZnO thin films as high-performing, reliable functional materials, to be integrated in the fabrication of pressure sensors and for energy harvesting applications.

To further state the versatility of ZnO thin films, both spin coated and RF magnetron sputtered dense ZnO thin films were synthesized and used as seed layers for promoting the growth of well-aligned ZnO nanowires via a hydrothermal method, using two different growth solutions. The influence of the seed layer characteristics, deriving from the different synthesis conditions, on the final morphology and wettability properties of the ZnO NWs was analyzed. A time-dependent behavior of the wetting properties was found for both sputtered and spin coated seed layers. In particular, a marked transition from a hydrophilic to hydrophobic state, associated to a change of the surface free energy of the films, was obtained for sputtered seed layers. In the case of spin-coated films this transition towards higher contact angles was still present but less pronounced and dependent on the precursor concentration. The surface of the aged spin coated seed layer synthesized from a higher precursor concentration was still hydrophilic after two weeks from its deposition. A strong relationship between the kind of seed layer, i.e., sputtered or spin-coated, and the final NWs morphology, surface chemistry and thus wettability was noticed. In particular NWs grown on sputtered seed layers showed a columnar morphology, high aspect ratio and a superhydrophobic behavior, with contact angles of around 180°. In contrast, on spin coated seed layers, highly hydrophilic NWs with hydroxyl-rich surfaces, conical-shape morphology and high aspect ratio were obtained. In addition, densely packed ZnO nanowires could be obtained by increasing the

concentration of the starting seed layer by spin-coating. It could be also noted in general that fresh seed layers (both sputtered and spin coated) led to thinner but shorter nanowires, whereas NWs on aged seed layers were longer and thicker. It is therefore demonstrated that ZnO nanowire arrays with tunable density, aspect ratio and wetting properties can be easily produced on broad surface areas (typically cm^2-sized). Depending on their surface chemistry and wetting behavior, superhydrophobic nanowires, ideal for self-cleaning, anti-fogging or microfluidic devices can be obtained. In contrast the hydroxyl-rich and hydrophilic surface makes the ZnO nanowires ideal candidate for further surface functionalization with enhanced adsorption properties towards biological agents or dye for imaging, diagnostic, optical or photovoltaic applications.

A simple two-step method, developed for growing sponge-like nanostructured ZnO films, was presented and the resulting materials were properly analyzed. The first step of this process consisted in growing metallic zinc films by the RF magnetron sputtering technique. Different deposition conditions were used and the resulting samples were properly analyzed by means of FESEM and XRD measurements. The morphology of the zinc films was found to be strictly dependent on the RF power used for the deposition, with compact zinc films obtained with the highest value, while the sponge-like morphology was found to be present only when the lowest value was used. The presence of such a particular nanostructure was discussed and explained by the Thornton's "structure zone" model. XRD patterns highlighted the presence of the metallic phase in all the Zn samples, independently of the deposition conditions. The conversion of the metallic film into zinc oxide was achieved by two different methods. The first one was a standard thermal oxidation process, carried out at 380°C for 120 min in ambient air. Both FESEM and XRD analysis confirmed that the morphological characteristics of the starting Zn layer were still present after the oxidation process. XRD also confirmed the presence of the oxide phase after the thermal treatment, meaning that the conversion of zinc into zinc oxide was successfully achieved. This last condition, however, was only partially pursued in the case of the sample deposited with the highest RF power. Indeed, different diffraction peaks associated to zinc were still present in the diffraction pattern acquired after the thermal oxidation. The set of the optimal deposition parameters for growing sponge-like nanostructured ZnO films with a thickness of few micrometers was then selected according to the characterization results. The chemical composition of the sponge-like ZnO films was also analyzed by means of XPS, confirming the presence of oxygen atoms bonded to zinc atoms. Sponge-like ZnO films were also grown on conductive substrates, and the converse piezoelectric effect was analyzed. The high electronic mobility gave to this particular material a resistive behavior. Moreover, a contribution coming from the bending of the substrate, which could not be excluded from the measure, not allowed a proper estimation of the piezoelectric constant in the analyzed material. In view of exploiting the properties of sponge-like piezoelectric ZnO films in the fabrication of flexible devices, a fully low-temperature oxidation approach to convert Zn nanostructures into sponge-like ZnO films was also presented. In this case, the prolonged exposure of the Zn metallic film to the action of water-vapor resulted in the conversion of Zn into ZnO. This was confirmed by the XRD characterization results, emphasizing the presence of diffraction peaks related to the oxide phase, which showed a hexagonal wurtzite-like crystal structure. FESEM analysis evidenced the sussistance of the sponge-like morphology of the starting Zn film after the water-vapor oxidation, as noticed in the case of thermally treated samples. The chemical composition analysis further confirmed the presence of the oxide in the water-vapor oxidized Zn films, while optical contact angle measurements highlighted the hydrophilic behavior of metallic Zn, and of thermally oxidized and water-vapor oxidized ZnO sample surfaces. On the basis of the reported results, sponge-like ZnO films represent a possible alternative to conventional 1-D nanostructures for the fabrication of both hard and flexible sensors and energy harvester devices.

In view of further exploiting the sponge-like morphology, Mn-doped and

Sb-doped sponge-like ZnO thin films were successfully deposited on conductive glass substrates by a three-step synthesis method. The first step consisted in the deposition of metallic Zn films with the RF magnetron sputtering technique. The resulting films provided a high active surface area characterized by the presence of a nanoporous network. This aspect was fully exploited in the second step of the synthesis process, when the nanoporous Zn films were impregnated for different impregnation times by soaking the samples in two different liquid solutions, providing the desired Mn and Sb doping elements. After the impregnation step, the samples were subjected to a thermal treatment, performed in ambient air, with the manifold aim of oxidizing the Zn network, obtaining the full conversion of the starting metallic film into ZnO, but at the same time to promote the diffusion and the insertion of the Mn and Sb doping agents into the ZnO crystal lattice. The morphological characterization confirmed the presence of a porous network on both Mn- and Sb- doped ZnO films, underlining the non-destructive nature of the method followed for the synthesis of the analyzed materials. Energy Dispersive X-ray spectroscopy and X-ray Photoelectron Spectroscopy confirmed the presence of the doping elements in all the samples, and highlighted the increase of the dopant content with the increase of the impregnation time. From the XPS analysis also the nature of the chemical bonds involving the doping elements could be determined, allowing to confirm that the detected dopants did not form any secondary metallic or oxide phases, but completely participated into the doping process of ZnO. This last aspect was further confirmed by the X-ray diffraction analysis, which also highlighted the deterioration of the hexagonal crystal structure with respect to the undoped ZnO sample. The presence of the dopant elements into the crystal structure of ZnO, together with a degradation of the crystal lattice, was further assessed through Raman spectroscopy, which evidenced the presence of vibrational peaks typical of Mn- and Sb- doped ZnO nanomaterials. The introduction of substitutional dopants into the ZnO lattice is expected to distort the crystal cell, which should in turn result into the appearance of ferroelectricity, that is not normally observed in undoped ZnO. This last aspect was properly analyzed by electrical measurements on undoped, Mn-doped and Sb-doped sponge-like ZnO films. Results confirmed the absence of ferroelectrcity in the undoped ZnO sample, which showed its typical capacitor-like behavior. In the case of the Mn-doped samples, a change in the electrical behavior was also observed, but no ferroelectric phenomena were noticed. Conversely, a high resistance contribution was highlighted in the I-V response, being represented by linear characteristics and high current range regimes, which were in the order of magnitude of 10^{-3} A. Typical ferroelectric switching phenomena in the I-V characteristics were instead observed in the Sb-doped ZnO films, showing the presence of hysteretical polarization loops, with residual polarizations at zero bias voltage. The reported results suggest a simple, elegant and reliable method for the synthesis of Mn- and Sb- doped, sponge-like ZnO films.

Publications list

— M. Vacca, M. Graziano, A. Chiolerio, A. Lamberti, M. Laurenti, D. Balma, E. Enrico, F. Celegato, P. Tiberto, L. Boarino, and M. Zamboni, "Electric Clock for NanoMagnet Logic Circuits" in: *Field-Coupled Nanocomputing. Paradigms, Progress, and Perspectives* / Neal G. Anderson, Sanjukta Bhanja. Springer Berlin Heidelberg, (2014) pp. 73-110. (Chapter 2, Section 2.1)

— C. Ottone, M. Laurenti, P. Motto, S. Stassi, D. Demarchi, and V. Cauda, "ZnO Nanowires: Synthesis Approaches and Electrical Properties" in: *Nanowires . Synthesis, Electrical Properties and Uses in Biological Systems* / Luke J Wilson. Nova Publishers, (2014) pp. 1-57. (Chapter 4)

— M. Laurenti, V. Cauda, R. Gazia, M. Fontana, V.F. Rivera, S. Bianco, and G. Canavese, "Wettability control on ZnO nanowires driven by seed layer properties", *Eur. J. Inorg. Chem.*, **2013** (2013) 2520-2527. (Chapter 6)

— A. Lamberti, A. Sacco, M. Laurenti, M. Fontana, C.F. Pirri, and S. Bianco, "Sponge-like ZnO nanostructures by low temperature water vapor-oxidation method as dye-sensitized solar cell photoanodes", *J. Alloy. Compd.* **615** (2014) S487-S490. (Chapter 7, Section 7.3)

List of Figures

List of Tables